JETP Letters, Vol. 73, No. 9, 2001, pp. 439–442. Translated from Pis'ma v Zhurnal Éksperimental'noĭ i Teoreticheskoĭ Fiziki, Vol. 73, No. 9, 2001, pp. 499–502.

On the Oscillations of the Plasma Atmosphere in Gamma-Ray Bursts

V. P. Vlasov and B. A. Trubnikov

Institute of Nuclear Fusion, Russian Research Centre Kurchatov Institute, pl. Akademika Kurchatova 1, Moscow, 123182 Russia

Received March 5, 2001; in final form, March 27, 2001

One of the possible hypotheses implies that cosmic gamma-ray bursts can arise when two neutron stars or black holes merge together. These bursts sometimes continue for several tens of seconds, but the time dependence of their intensity often exhibits ~10^2–10^3 almost periodic small peaks with a period of ~10 ms. A model of oscillations in the lower plasma shell, which arises in cosmic gamma-ray bursts and is located near a neutron star, is proposed; the greater part of arising plasma in the form of an "upper" shell continues to expand into the surroundings. Other possible interpretations of periodicity of the "small peaks" are also analyzed. © *2001 MAIK "Nauka/Interperiodica".*

PACS numbers: 98.70.Rz; 95.30.Qd

Typical time dependences of the intensities of cosmic gamma-ray bursts (CGBs) are shown in Figs. 1 and 2, where almost periodic small peaks are observed against a wide background hump.

In addition, after the basic burst with small peaks, Fig. 1 exhibits two sequential bursts. Therefore, we can assume that, during this burst, two gradually approaching neutron stars touch one another, then some part is broken off, returns, and touches the basic residual two more times 18 and 25 s after the first contact of the stars. Approximate constancy of the period of small peaks with a duration of 1–10 ms was pointed out by, e.g., Postnov [1], who indicated that this property must be explained because the periods of small peaks should increase when a fireball scatters.

In this work, we demonstrate that this constancy can qualitatively be attributed to the stratification of the scattering plasma "atmosphere" into two regions with approximately identical thicknesses—an expanding upper shell and lower one, where small peaks are generated. Other hypotheses are also possible (see below), and the presence of the small peaks provides the possibility of gaining information on the fine structure of expanding fireball from experimental data. Below, we will explore this problem.

Instead of the spherical case, we first consider the problem of small oscillations in the atmosphere over the flat surface $z = 0$ in a constant gravitational field g. Assuming that the atmosphere arose from one source, we treat it as isentropic. In this case, it is convenient to express the density and pressure of a gas with the adiabat $p = p_0(\rho/\rho_0)^\gamma$ in terms of the reduced dimensionless temperature $\Theta = (T/T_0) = (\rho/\rho_0)^{\gamma-1}$. Then, the hydrodynamic equations take the form

$$\frac{\partial\Theta}{\partial t} + v\frac{\partial\Theta}{\partial z} = -\frac{\Theta}{\mu}\frac{\partial v}{\partial z},$$
$$\frac{\partial v}{\partial t} + v\frac{\partial v}{\partial z} = -g - \mu c_0^2\frac{\partial\Theta}{\partial z}, \tag{1}$$

where $\mu = 1/(\gamma - 1)$ and $c_0 = \sqrt{\gamma p_0/\rho_0}$ is the speed of sound at the lower boundary $z = 0$ of the atmosphere. In the stationary case ($v = 0$), we obtain the equilibrium profiles of the temperature, pressure, and density in the form

$$\Theta^0 = 1 - \xi, \quad \rho^0 = \rho_0(1-\xi)^\mu,$$
$$p^0 = p_0(1-\xi)^{\gamma\mu}. \tag{2}$$

Here, $\xi = z/H_0$, where $H_0 = \mu c_0^2/g$ is the upper atmosphere boundary. As is seen, the temperature in the isentropic atmosphere with arbitrary adiabat exponent γ linearly decreases as the height increases.

Setting $\Theta = \Theta^0 + \theta$, where $\theta \sim \exp(i\omega t) \ll \Theta^0$, we obtain the equations of small oscillations:

$$v = i\frac{\mu c_0^2}{\omega H_0}\frac{d}{d\xi}\theta,$$
$$(1-\xi)\theta''_{\xi\xi} - \mu\theta'_\xi + \Omega^2\theta = 0, \quad \Omega = \omega\frac{H_0}{c_0}, \tag{3}$$

0021-3640/01/7309-0439$21.00

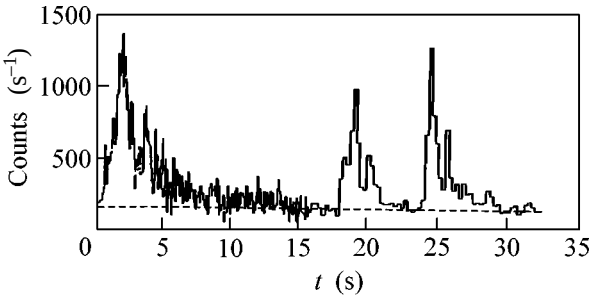

Fig. 1. The time dependence of the intensity of a CGB on January 13, 1979.

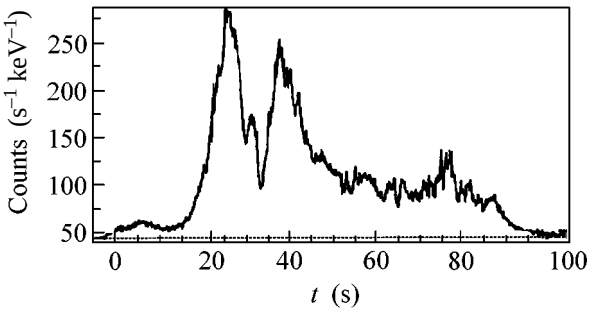

Fig. 2. The time dependence of the intensity of a CGB on January 23, 1999.

whose solution is expressed in terms of the Bessel function:

$$\theta = x^{-p}J_p(2\Omega x), \quad x = \sqrt{1-\xi}, \quad p = \mu - 1. \quad (4)$$

We omitted the second solution because it diverges at the upper boundary $z = H_0$, i.e., at $x = 0$. The velocity $v \sim d\theta/d\xi \sim x^{-p-1}J_{p+1}(2\Omega x)$ should vanish at the lower boundary $z = 0$, i.e., at $x = 1$. Therefore, the natural frequencies are determined from the equation $J_\mu(2\Omega_n) = 0$, where $n = 1, 2, 3, \ldots$. Using the well-known asymptotic form of the Bessel function, we find the natural frequencies $\Omega_n \approx (\pi/8)(2\mu - 1 + 4n)$.

A case when the adiabat exponent has the one-atomic value $\gamma = 5/3$ is particularly simple. In this case, $\mu = 3/2$, the Bessel function $J_{3/2}(z) = \sqrt{2/\pi z}\,(z^{-1}\sin z - \cos z)$, and the frequencies are determined from the equation $2\Omega_n = \tan(2\Omega_n)$. Therefore, $\Omega_n \approx \pi(2n + 1)/4$; i.e., $\Omega_1 \approx 3\pi/4$, $\Omega_2 \approx 5\pi/4$, … .

We note also the case when $\gamma = 3/2$, i.e., $\mu = 2$. In this case, the equation has the form $J_2(2\Omega_n) = 0$, which gives $\Omega_n \approx \pi(4n + 3)/8$, … .

In summary, at $\gamma = 5/3$, the first frequency is $\Omega_1 \approx 2.3$, corresponding to the fundamental period $T_1 \approx 3H_0/c_0$. For the neutron star radius ~10 km, the height of the lower atmosphere arising at a gamma-ray burst can be about 10–100 km and the speed of sound in electron–positron plasma at a temperature of 10 keV is approximately one-tenth of the speed of light. In this case, the oscillation period is $T_1 \sim 1$–10 ms, which can be attributed to the small peaks against the general hump in the intensity of a CGB continuing ~1–10–100 s.

Observations indicate that the period of small peaks does not noticeably increase at the end of the basic hump and, therefore, the height H_0 of the lower atmosphere does not vary. It is reasonable to assume that most of the plasma formed is ejected upward in the form of a mushroom (as occurs in surface nuclear explosions) and forms the upper atmosphere in the form of a spherical shell, which continues to diverge into the surroundings at approximately the speed of light.

According to the magnetic model proposed in [2], CGBs are induced due to generation of a strong magnetic field B in the shear flow of arising plasma, which revolves around the star body of radius a. In this model, the linear time increase in the field is described by the simple magnetohydrodynamic equation $\mathbf{B}_t' = \mathrm{curl}[\mathbf{vB}]$ in the case of a constant velocity $v = v_0(a/r)^n\sin\theta$. For the initial field $B \sim 10^{12}$ G and velocity $v_0 \sim c/2$, this mechanism can pump the total magnetic energy W_{mag} on the order of the kinetic energy of rotation of two touching neutron stars into the plasma during typical CGB times. This estimate corresponds to the observed CGB energies.

For the problem of small peaks, it is important to note that the field is generated in this mechanism in a fairly narrow layer, which is assumed to separate the upper and lower plasma atmospheres and keep approximately constant thickness H_0 of the latter.

For completeness, let us consider the case of a spherical "lower" shell over the neutron star of radius a. This gives the following remarkable result: in the case $a \ll H_0$, the periods of small oscillations are independent of the star size and depend only on the upper bound H_0.

The equations for a spherical layer are written as

$$\frac{\partial\Theta}{\partial t} + v\frac{\partial\Theta}{\partial r} = -\frac{\Theta}{\mu}\frac{\partial}{r^2\partial r}(r^2 v),$$
$$\frac{\partial v}{\partial t} + v\frac{\partial v}{\partial r} = -g - \mu c_0^2\frac{\partial\Theta}{\partial r}. \quad (5)$$

But here, $g = GM/r^2$ depends on the radius and the latter equation provides the profile of equilibrium temperature $\Theta^0 = \theta_*[(H_0/r) - 1]$, where $\theta_* = GM/\mu c_0^2 H_0 = \mathrm{const}$.

Setting as above $\Theta = \Theta^0 + \theta$, we obtain the equations for small disturbances of the temperature and velocity

$$i\omega\theta = \frac{\theta_*}{\mu}\left[\frac{v}{r}\left(\frac{\mu-2}{r}H_0 + 2\right) - \left(\frac{H_0}{r} - 1\right)\frac{dv}{dr}\right],$$
$$i\omega v = -\mu c_0^2 \frac{d}{dr}\theta, \quad (6)$$

whose solutions for arbitrary γ values are not expressed in terms of known functions and can be determined by numerical calculations.

Only for $\mu = 2$, i.e., $\gamma = 3/2$, are the relations simplified and reduced to the equation

$$\frac{d^2}{dy^2}\theta + \frac{2d}{ydy}\theta + \Omega^2\left(\frac{1}{y} - 1\right)\theta = 0, \quad (7)$$

where $\Omega = \omega H_0/c_0\sqrt{\theta_*}$ and $y = 1 - (r/H_0) < 1$. Introducing the argument $z = 2\Omega y$ and setting $\theta = \exp(-z/2)K(z)$, we obtain the equation

$$zK''_{zz} + (2-z)K'_z - [1 - (\Omega/2)]K = 0, \quad (8)$$

which is satisfied by the known (see [3]) Kummer confluent hypergeometric function $K(z) = M(a, b, z)$ with the parameters $a = 1 - \Omega/2$ and $b = 2$. The boundary condition is that the velocity v vanishes at the star surface, i.e., at $r = a$. But assuming that $a \ll H_0$, we impose this condition at $r = 0$, i.e., at $y = 1$, $z = 2\Omega$. In this case, the dimension of the star is omitted.

We found numerically (by the Kummer series) the values $\Omega_n = 3.3$, 5.4, 7.5, and 9.5, which differ little from the "flat" spectrum determined by the equation $2\Omega = \tan(2\Omega)$ at $\gamma = 5/3$ (see above).

The periods of harmonics are represented as

$$T_n = \sqrt{2}\frac{T_*}{\Omega_n}, \quad T_* = 2\pi\sqrt{\frac{H_0^3}{GM}}, \quad (9)$$

where T_* is the period of revolution of satellites in the orbit with radius H_0 from the center of the neutron star of mass M. Formula (9) yields the periods $\sim 10^{-3}$ s, which coincide with the estimates for the flat model.

Let us clarify the behavior of the expanding outer CGB shell for which, due to its detachment from the star, for simplicity we ignore the gravitational strength g. Omitting g in Eqs. (5), we can find the following simplest self-similar solution with a linear profile of velocity and a parabolic profile of temperature:

$$v(r, t) = \frac{r}{R(t)}\dot{R}, \quad \dot{R} = \frac{dR}{dt},$$
$$\theta(r, t) = \left(\frac{R_0}{R}\right)^2\left(1 - \frac{r^2}{R^2}\right), \quad (10)$$

where $R = R(t) = R_0\sqrt{1 + (t/\tau_0)^2}$ and $\tau_0 = R_0/c_0\sqrt{3}$. We emphasize that this solution is obtained only for the one-atomic exponent $\gamma = 5/3$, i.e., $\mu = 3/2$. According to this solution, the velocity $\dot{R}$ of the outer boundary first (at $t \ll \tau_0$) increases with time and then (at $t \gg \tau_0$) attains a constant value $\dot{R}_{\max} = c_0\sqrt{3} = \text{const}$. If this maximal nonrelativistic value is higher than the speed of light, it is necessary to use the relativistic equations of gas motion.

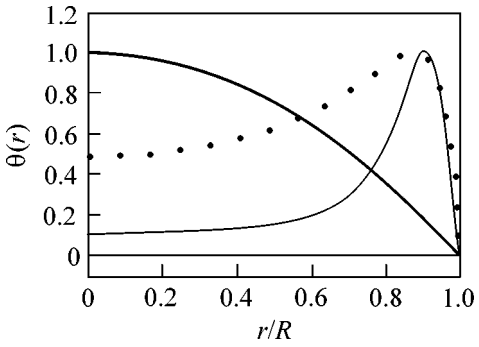

Fig. 3

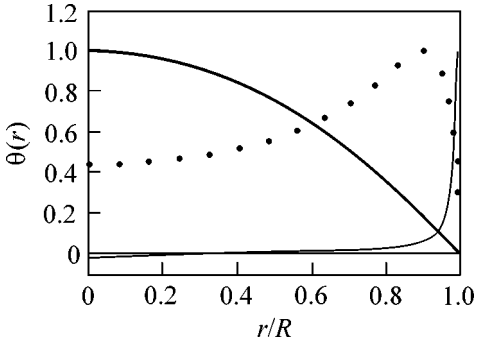

Fig. 4

We numerically solved these equations in two variants. The first and the second variants involve the equation of state in the intrinsic reference frame for nonrelativistic gas with an adiabatic exponent of 5/3 and for ultrarelativistic gas, respectively. Figures 3 and 4 show the radial profile of the temperature calculated for two successive time instants differing by an order of magnitude.

The lines are normalized so that all three maxima are equal to unity and the right edge is the propagating front. Both figures also present the parabola of nonrelativistic solution (10). The dotted and solid lines in these figures are the profiles for the first and the second variants, respectively.

In contrast to time-independent nonrelativistic profiles (10), ultrarelativistic gas concentrates near the front as time increases and forms the increasing hump of temperature and density immediately behind the front. Therefore, a thin scattering spherical shell is formed and moves virtually at the speed of light.

Then, the shell as a "bulldozer" rakes the rarefied gas of the surroundings. As a result, the X-ray, optical, and radio afterglows of CGBs arise sequentially, continue for about a day, weeks, and months, respectively, and are observed after CGBs.

For treating the *periodicity* of small peaks in the model proposed above, it should be assumed that only one (fundamental) mode of oscillation is excited if the peaks are indeed strictly periodic. The accuracy of observed intensities is still insufficient for drawing a conclusion about strict periodicity. But if it is discovered, another interpretation of the periodicity can be considered along with the model proposed above.

In particular, one may expect that a body (maybe a black hole) which is formed when a pair of rapidly rotating neutron stars merges takes the form of a Maclaurin general ellipsoid rotating with a period on the order of milliseconds [cf. Eq. (9)]. It is its rotation that provides the strict periodicity of small peaks. In this case, three large humps could be attributed to the fact that the general ellipsoid loses stability after 18 s due to the evaporation of two of its opposite vertices, becomes a Maclaurin two-axis ellipsoid, and, at 25 s, becomes a single-axis ellipsoid of revolution due to the further mass evaporation. If this is a black hole consisting of quarks (this possibility was pointed out in [2] and [4]), these rearrangements of the body shape should be accompanied by intense coupling of quarks into hadrons, which induces gamma-ray bursts. It is interesting to note that the small peaks in Fig. 1 are distinct only in the first hump, whereas they are less pronounced or completely absent in two subsequent humps. To our knowledge, the possibility of Maclaurin rearrangement of a body generating gamma-ray bursts has not been discussed yet.

Addition after review. Gershteĭn [5] proposed a different mechanism implying that CGB arises when a massive Volf–Rayet star collapses, leading to the production of a neutron star. Subsequent accretion of matter from the shell to the star surface results in thermonuclear combustion, which can occur in the oscillator regime with the characteristic periods $\tau \sim (G\rho_*)^{-1/2} \sim$ 10 ms, where the estimate $\rho_* \sim 10^{11}$ g/cm^3 for the matter density at the boundary of a neutron star was obtained in [6]. Gershteĭn [5] emphasized that the analysis of the small peaks "can be a basic key for the problem of the gamma-ray bursts."

This work was supported by the Council for Grants of the President of the Russian Federation and by the Russian Foundation for Basic Research (project no. 00-15-96526 for support of Leading Scientific Schools).

REFERENCES

1. K. A. Postnov, Usp. Fiz. Nauk **169**, 545 (1999).
2. I. L. Rozental' and B. A. Trubnikov, Pis'ma Zh. Éksp. Teor. Fiz. **70**, 417 (1999) [JETP Lett. **70**, 419 (1999)].
3. *Handbook of Mathematical Functions*, Ed. by M. Abramowitz and I. A. Stegun (Dover, New York, 1971; Nauka, Moscow, 1979).
4. D. B. Cline, C. Matthey, S. Otvinovski, *et al.*, astro-ph/9905346 (1999).
5. S. S. Gershteĭn, Pis'ma Astron. Zh. **26**, 848 (2000) [Astron. Lett. **26**, 730 (2000)].
6. D. K. Nadyozhin, Astrophys. Space Sci. **53**, 131 (1978).

Translated by R. Tyapaev

JETP Letters, Vol. 73, No. 9, 2001, pp. 443–445. From Pis'ma v Zhurnal Éksperimental'noĭ i Teoreticheskoĭ Fiziki, Vol. 73, No. 9, 2001, pp. 503–505.

Possible Galactic Sources of Ultrahigh-Energy Cosmic Rays and a Strategy for Their Detection Via Gravitational Lensing[1]

A. Kusenko[1,2] and V. A. Kuzmin[3]

[1] *Department of Physics and Astronomy, UCLA, Los Angeles, CA 90095-1547, USA*
[2] *RIKEN BNL Research Center, Brookhaven National Laboratory, Upton, NY 11973, USA*
[3] *Institute for Nuclear Research, Russian Academy of Sciences, Moscow, 117312 Russia*

Received March 28, 2001

If decays of superheavy relic particles in the galactic halo are responsible for ultrahigh-energy cosmic rays, these particles must be clustered to account for small-scale anisotropy in the AGASA data. We show that the masses of such clusters are large enough for them to gravitationally lens stars and galaxies in the background. We propose a general strategy that can be used to detect such clusters via gravitational lensing, or to rule out the hypothesis of decaying relic particles as the origin of highest energy cosmic rays. © *2001 MAIK "Nauka/Interperiodica".*

PACS numbers: 98.70.Sa; 98.62.Sb

The origin of cosmic rays [1–3] with energies beyond the Greisen–Zatsepin–Kuzmin (GZK) cutoff [4] is unknown. One of the possible explanations invokes decays of metastable superheavy relic particles X with masses 10^{13} GeV or higher and cosmologically long lifetimes [5–7]. Such superheavy particles could be produced nonthermally at the end of inflation [8–10]. Their extremely small decay width may be due to a conservation of some topological charge [6]. Particles with the requisite properties may also arise from string theory [11].

If these particles decay into hadrons and photons, the flux of ultrahigh-energy cosmic rays (UHECR) is dominated by those particles in the halo of our galaxy [5]. This can explain the absence of the GZK cutoff. Even if the superheavy particles decay predominantly into neutrinos [12], cosmic rays with energies beyond the GZK cutoff may originate through Z bursts [13]. In this letter, we concentrate on the former possibility and assume that observed ultrahigh-energy events [1–3] come mainly from the decays of relic particles in the Milky Way halo.

The new data provide an opportunity to test this hypothesis through gravitational lensing. There is strengthening evidence for directional clustering of events in the AGASA data [2, 3]. The latest analyses [2] show one triplet and six doublets of events, each originating from the same point in the sky, to ±1.3° accuracy. The probability of this clustering to occur by accident is less than 0.07% [2]. The only way to reconcile these data with the hypothesis of relic particle decays is to assume a nonuniform distribution of particles in the halo. If the relic particles form regions of increased density, such lumps may be responsible for the doublets in the UHECR data. To produce a doublet, a lump of particles must be of a certain size determined by the decay probability. Since the mass of the hypothetical particle is fixed by the energy of UHECR, there is a prediction for the mass of each lump that can give rise to a doublet. In addition, the celestial coordinates of the particle cluster are known to one degree accuracy. In this letter we propose a novel gravitational lensing technique that can be used to discover a cluster of relic particles, or to rule out such particles as the origin of ultrahigh-energy cosmic rays.

Under the assumption that UHECR are caused by the relic particle decays, the data suggest that (in addition to a possible uniform distribution) on the order of ten clusters of X particles exist in our galactic halo. N-body simulations of dark matter halos predict some inhomogeneities that can be related to small-scale anisotropy of UHECR [14] but probably are not sufficient to produce larger clumps. However, additional interactions of the hypothetical particles can alter this picture dramatically. We assume that each doublet comes from a separate cluster of particles. Here, we do not discuss the dynamics of clustering of the heavy particles. This issue will be addressed in an upcoming publication. We note in passing that clumps of dark matter with masses $10^8 M_\odot$ may resolve [15] the widely debated issue of cusps in the halo density profiles [16].

If the X-particle lifetime is $\tau_X \sim 10^{10}$–10^{22} yr [6], a cluster of N particles produces decays at a rate

$$P = \frac{N}{\tau_X} \sim (10^{-10}\text{–}10^{-22})N \text{ yr}^{-1}. \quad (1)$$

[1] This article was submitted by the authors in English.

0021-3640/01/7309-0443$21.00 © 2001 MAIK "Nauka/Interperiodica"

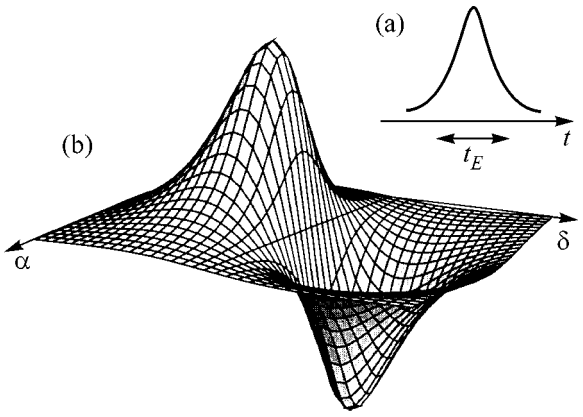

Fig. 1. A typical light curve for gravitational lensing of a single source as a function of time (a) and the corresponding plot of brightness variations for a sample of stars (b) as a function of celestial coordinates, in arbitrary units. Photometric changes indicate the location of the lens.

The probability for the decay products to produce an air shower in a detector is $P \times (d/L)^2$, where $d \sim 10^6$ cm is the size of the detector and $L \sim 10^{23}$ cm is the distance to the cluster of relic particles. In order to have a doublet in a one-year data set, each cluster must have

$$N \sim \frac{\tau_X}{1\ \text{yr}}\left(\frac{L}{d}\right)^2 \sim 10^{50}\left(\frac{\tau_X}{10^{16}\ \text{yr}}\right) \qquad (2)$$

particles. If an X particle has mass $m_X \sim 10^{13}$ GeV [5, 6], the mass of the cluster is

$$M \sim 10^{63}\left(\frac{\tau_X}{10^{16}\ \text{yr}}\right)\ \text{GeV} = 10^6\left(\frac{\tau_X}{10^{16}\ \text{yr}}\right)M_\odot. \qquad (3)$$

The lifetime τ_X can be in the range from 10^{10} yr (for the relic particles to survive until the present) to 10^{21} yr (for the total mass of the clusters not to exceed the mass of the galaxy). Correspondingly, the masses of clusters can range from one solar mass to $10^{10}M_\odot$.

There is a remarkable possibility to discover such invisible massive objects by what we will call a "lens-chasing" technique. Although the cluster can be entirely dark, it can be detected through gravitational lensing of stars and galaxies behind it. AGASA data [1, 2] provide the celestial coordinates of the clusters with a precision of a few degrees.

The Einstein radius of a cluster with mass M is

$$R_E = 0.14\ \text{pc}\left[\frac{M}{10^7 M_\odot}\frac{L}{10\ \text{kpc}}\right]^{1/2}. \qquad (4)$$

A lens of this kind has angular size

$$\theta_E = \frac{R_E}{L} = 0.0008^\circ\left[\frac{M}{10^7 M_\odot}\frac{10\ \text{kpc}}{L}\right]^{1/2} \qquad (5)$$

and passes the line of sight in time

$$t_E = \frac{R_E}{10^{-3}c} = 4.8\times 10^2\ \text{yr}\left[\frac{M}{10^7 M_\odot}\frac{L}{10\ \text{kpc}}\right]^{1/2}. \qquad (6)$$

We propose to use the small changes in brightness of stars and galaxies behind the lens on time scales of the order of one year. The AGASA data specify the location of the cluster to ±1.3°. It is possible to scan over a large sample of remote sources in the patch specified by the UHECR data, recording the brightness of the background stars and galaxies. The scan must be repeated after a period of several months. Next, one should extract the changes in the absolute brightness of the background stars. A slowly moving lens with a single-star light curve shown in Fig. 1a will produce a map of brightness differentials shown in Fig. 1b. By using temporal changes in the brightness of stars from a large sample, one can locate a small lens within a large, 2.5°, patch of the sky.

The number of background sources chosen for scanning and photometry determines the sensitivity of the proposed lens-chasing experiment. Let us consider a sample of n^2 stars with an average angular separation of $\theta_b \approx 2.5^\circ/n$. A lens that passes near one of these stars at an angular distance $\delta\theta = \theta_b/2 < \theta_E$ from the line of sight will magnify the source by a factor $(2\theta_E/\theta_b)^2$ as compared to its brightness in the absence of the lens. The change in the star's brightness over a one-year period is

$$\frac{\Delta A}{A} \approx \frac{1\ \text{yr}}{t_E}\left(\frac{\theta_E}{\theta_b/2}\right)^2 = \frac{1\ \text{yr}}{t_E}\left(\frac{2n\theta_E}{2.5^\circ}\right)^2$$
$$= 0.8\%\left(\frac{n^2}{10^7}\right)\left[\frac{M}{10^7 M_\odot}\right]^{1/2}\left[\frac{10\ \text{kpc}}{L}\right]^{3/2}. \qquad (7)$$

Assuming a better than 1% precision photometry, a sample of 10^7 background sources allows detection of clusters with mass $10^7 M_\odot$ and higher. Smaller masses require a higher number of background sources. For comparison, the MACHO project has monitored 11.9 million stars during 5.7 yr of operation [17]. Of course, lens chasing presents a very different challenge from that faced by MACHO. Unlike MACHO, which monitors bright nearby stars in the Large Magellanic Cloud on a continuous basis, we want a relatively infrequent (once a year) accurate photometry of stars in the directions of UHECR doublets.

Some of the clusters in the AGASA data lie in the supergalactic plane [2, 3]. The presence of many relatively close (and, hence, bright) background stars in these directions makes the corresponding clusters particularly appealing for lens chasing.

One can, of course, refine this technique. If the lensing cluster is discovered after several initial crude scans, one can narrow down its coordinates and perform a more detailed monitoring of closely spaced sources around the location of the lens.

We note in passing that future detectors can observe yet another signature of the same kind of sources. Decays of superheavy particles and subsequent fragmentation can produce excited hadrons. Their decays, in turn, can produce simultaneous air showers separated by thousands of kilometers. The time delay is $\delta t = t\gamma^{-2}\Delta E/E$, where t is the time of flight, $\gamma \sim 10^{11}$ is the Lorentz factor, and $\Delta E/E \sim 1$. The difference in the arrival time $\delta t \sim 10^{-11}$ s, and the distance between air showers is on the order of 10^3 km. Future space-based detectors, such as EUSO and OWL, will be able to observe such spatially separated events in coincidence.

To summarize, a small-scale anisotropy in the AGASA data demands that, if the UHECR are due to decaying relic particles in the halo, these particles form clusters with coordinates specified by the cosmic ray events. The masses of such clusters can range from $M_\odot$ to $10^{10}M_\odot$. We have proposed a general strategy for detecting such clusters by their gravitational lensing of the background stars and galaxies.

This work was supported by the NATO Collaborative Linkage Grant no. PST.CLG.976397. In addition, A.K. was supported by the US Department of Energy, grant no. DE-FG03-91ER40662, Task C. The work of V.A.K. was supported in part by the Russian Foundation for Basic Research, project no. 98-02-1744a. V.A.K. thanks UCLA for hospitality during his visit, when this work was performed.

REFERENCES

1. M. Takeda, N. Hayashida, K. Honda, *et al.*, Phys. Rev. Lett. **81**, 1163 (1998); M. A. Lawrence, R. J. Reid, and A. A. Watson, J. Phys. G **17**, 733 (1991); D. J. Bird, S. C. Corbató, H. Y. Dai, *et al.*, Phys. Rev. Lett. **71**, 3401 (1993); Astrophys. J. **424**, 491 (1994); N. Hayashida *et al.*, Astrophys. J. **522**, 225 (1999).
2. M. Teshima, *Talk Presented at First International Workshop on Radio Detection of High-Energy Particles (RADHEP-2000), Los Angeles, 2000*.
3. M. Takeda, N. Hayashida, K. Honda, *et al.*, Astrophys. J. **522**, 225 (1999).
4. K. Greisen, Phys. Rev. Lett. **16**, 748 (1966); G. T. Zatsepin and V. A. Kuzmin, Pis'ma Zh. Éksp. Teor. Fiz. **4**, 114 (1966) [JETP Lett. **4**, 78 (1966)].
5. V. Berezinsky, M. Kachelriess, and A. Vilenkin, Phys. Rev. Lett. **79**, 4302 (1997).
6. V. A. Kuzmin and V. A. Rubakov, Yad. Fiz. **61**, 1122 (1998) [Phys. At. Nucl. **61**, 1028 (1998)].
7. K. Hamaguchi, Y. Nomura, and T. Yanagida, Phys. Rev. D **59**, 063507 (1999).
8. D. J. Chung, E. W. Kolb, and A. Riotto, Phys. Rev. Lett. **81**, 4048 (1998); Phys. Rev. D **59**, 023501 (1999).
9. V. Kuzmin and I. Tkachev, Pis'ma Zh. Éksp. Teor. Fiz. **68**, 255 (1998) [JETP Lett. **68**, 271 (1998)].
10. V. A. Kuzmin and I. I. Tkachev, Phys. Rep. **320**, 199 (1999).
11. K. Benakli, J. Ellis, and D. V. Nanopoulos, Phys. Rev. D **59**, 047301 (1999); **59**, 123006 (1999); M. Birkel and S. Sarkar, Astropart. Phys. **9**, 297 (1998).
12. G. Gelmini and A. Kusenko, Phys. Rev. Lett. **84**, 1378 (2000); J. L. Crooks, J. O. Dunn, and P. H. Frampton, astro-ph/0002089.
13. T. Weiler, Astropart. Phys. **11**, 303 (1999); D. Fargion, B. Mele, and A. Salis, Astrophys. J. **517**, 725 (1999).
14. P. Blasi and R. Sheth, Phys. Lett. B **486**, 233 (2000); astro-ph/0006316.
15. A. El-Zant, I. Shlosman, and Y. Hoffman, astro-ph/0103386.
16. D. N. Spergel and P. J. Steinhardt, Phys. Rev. Lett. **84**, 3760 (2000); R. Dave, D. N. Spergel, P. J. Steinhardt, and B. D. Wandelt, astro-ph/0006218; B. D. Wandelt, R. Dave, G. R. Farrar, *et al.*, astro-ph/0006344.
17. C. Alcock, R. A. Allsman, D. R. Alves, *et al.* (MACHO Collab.), Astrophys. J. **542**, 281 (2000).

JETP Letters, Vol. 73, No. 9, 2001, pp. 446–450. Translated from Pis'ma v Zhurnal Éksperimental'noĭ i Teoreticheskoĭ Fiziki, Vol. 73, No. 9, 2001, pp. 506–510.

Test of Lorentz Invariance through Observation of the Longitudinal Development of Ultrahigh-Energy Extensive Air Showers

E. E. Antonov[1], L. G. Dedenko[1,*], A. A. Kirillov[2], T. M. Roganova[2], G. F. Fedorova[2], and E. Yu. Fedunin[1]

[1] *Faculty of Physics, Moscow State University, Vorob'evy gory, Moscow, 119899 Russia*
** e-mail: ddn@dec1.npi.msu.su*
[2] *Institute of Nuclear Physics, Moscow State University, Vorob'evy gory, Moscow, 119899 Russia*
Received April 2, 2001

An idea that Lorentz invariance can be violated was proposed by Coleman and Glashow to overcome the astrophysical problems of air showers of ultrahigh energies $E > 10^{20}$ eV. This statement can be tested by analyzing experimental data on these showers. The longitudinal development of showers and the distribution of the depths of shower maxima were calculated in the model of quark–gluon strings with allowance made for the Landau–Pomeranchuk–Migdal effect and the interactions of ultrahigh-energy neutral pions. Comparison of the calculations with available experimental data provides a new bound $|c_\gamma - c_{\pi^\circ}| < 10^{-20}$ for the possible difference between the speeds of photons and neutral pions. This bound becomes $|c_\gamma - c_{\pi^\circ}| < 10^{-22}$ when one takes the upper limiting value for the observed depth of maximum. © *2001 MAIK "Nauka/Interperiodica".*

PACS numbers: 13.85.Tp; 96.40.Pq; 11.30.Cp

The detection of giant air showers (GASs) of energies above 10^{20} eV [1–3] has revealed some problems. First, these energies are well beyond a cutoff that arises in the energy spectrum of primary cosmic rays (PCRs) due to interaction with relict photons, i.e., due to the Greisen–Zatsepin–Kuz'min (GZK) effect [4, 5]. A specific mechanism that is responsible for such high energies of particles remains an enigma. Second, the distribution of GAS arrival directions does not contradict the isotropic one. It is surprising that the arrival directions of ultrahigh-energy particles, which must travel along almost straight lines in known intergalactic magnetic fields, do not explicitly point to sources. These particles possibly arrive from cosmological distances [6], which contradicts the GZK prediction.

These problems were called the GZK paradox. To overcome this paradox, various extravagant ideas have long been proposed. One of such ideas was proposed about 30 years ago by Kirzhnits and Chechin [7, 8], who assumed possible violation of Lorentz invariance at ultrahigh energies and the gravitational origin of this violation. Recently, as the number of detected GASs of energies above 10^{20} eV considerably increased [9, 10], the interest in ideas implying Lorentz invariance violation (see, e.g., [11–16]) and in other extravagant suppositions grew. Topological defects, active galactic nuclei, γ-ray bursts [17], magnetic monopoles [18], *Z*-boson bursts (which are generated in collisions of ultrahigh-energy neutrinos with relict neutrinos near the Earth) [19], and decay of hypothetical very massive relict particles [20, 21] were considered as sources of ultrahigh-energy PCRs. Some authors [22–24] regarded the quantum properties of space–time, as well as quantum gravity, as causes of possible violation of Lorentz invariance.

In view of ideas proposed in [11], we consider here a new interesting possibility of testing Lorentz invariance through the results for observed longitudinal development of extensive air showers (EASs) of energies $E > 5 \times 10^{19}$ eV. Due to the assumption that maximal attainable speeds of photons c_γ and neutral pions c_{π° are different, neutral pions do not decay at energies $E_{\pi^\circ} \geq m_{\pi^\circ}/\sqrt{c_\gamma^2 - c_{\pi^\circ}^2}$, which results in faster dissipation of the energy of a PCR particle, as compared to the standard model. Therefore, the development of air showers occurs earlier, and, as a consequence, the depth $X_{\max}$ of their maximum decreases. Below, the supposition that $\Delta c_{\gamma\pi^\circ} = |c_\gamma - c_{\pi^\circ}| < 10^{-22}$ and $E_{\pi^\circ} = 10^{19}$ eV will be referred to as hypothesis 1. To estimate the effect of the degree of Lorentz invariance violation, we consider also hypothesis 2 in which $\Delta c_{\gamma\pi^\circ} = 10^{-20}$ and $E_{\pi^\circ} = 10^{18}$ eV. The longitudinal development of showers and the distribution of the depth $X_{\max}$ of shower maximum are calculated in the model of quark–gluon strings (QGSs) [25] with allowance made for the Landau–Pomeranchuk–Migdal effect [26] and interactions of ultrahigh-energy neutral pions with atomic nuclei in the atmosphere (standard variant) and with allowance

made for hypotheses 1 and 2. Comparison of calculations with available experimental data provides a new bound for the difference of maximal attainable speeds of photons and neutral pions.

The experimental procedure at Fly's Eye set and at its updated variant HiRes [10] provides determination of the cascade curve of a GAS. Figure 1 shows (points with error bars) experimental data [3] for the cascade curve of GAS of energy $E \sim 3.2 \times 10^{20}$ eV and (lines) our calculations. The dashed line is the standard variant of simulation. Solid lines *1* and *2* were calculated with hypotheses 1 and 2, respectively. It should be borne in mind that experimental data compose an individual cascade curve, whereas the calculations correspond to average curves (statistics of simulated showers is ~1000). Experimental estimate $X_{\max} = 815 \pm (40) + 45 - 35$ g/cm^2 [3], where the number in the parentheses is the systematic error and the last two numbers are statistical errors, for the depth of shower maximum can be compared to the theoretical values $X_{\max} = 875$, 866, and 836 g/cm^2 for the standard variant (dashed line), as well as for lines *1* and *2*, respectively. Errors in calculated estimates are less than several grams per centimeter squared. Note that Fig. 1 and above estimates for the depth $X_{\max}$ demonstrate that Lorentz invariance violation can be tested through data on the longitudinal development of GASs and hypotheses 1 and 2 are attractive for improving agreement in interpretation of experimental data.

More detailed information is shown in Fig. 2, where the distributions of the depths $X_{\max}$ for (dashed histogram) the standard variant of the model and for (solid histograms *1* and *2*) hypotheses 1 and 2, respectively, are plotted. Figure 2 demonstrates that the standard variant is free from showers with the depth of maximum $X_{\max} = 815$ g/cm^2. Only an increase in the experimental estimate for the depth $X_{\max}$ by the sum of systematic and statistical errors provides agreement between the experimental estimate and calculation. The computational results with hypothesis 1 and especially with hypothesis 2 do not noticeably differ from the experimental value. In particular, calculation with hypothesis 2 indicates that a considerable fraction (about 40%) of showers of energy $E \sim 3.2 \times 10^{20}$ eV attains a maximum up to a depth of 815 g/cm^2. Thus, an analysis of the distributions of the depths $X_{\max}$ corroborates the above conclusion that experimental data on the longitudinal development of GASs and, in particular, on the depth $X_{\max}$ of the shower maximum can be used as a test of possible Lorentz invariance violation in the ultrahigh-energy region. Because the calculation with hypothesis 2 agrees well with experimental data, the upper limit of violation can be estimated as $\Delta c_{\gamma\pi^\circ} < 10^{-20}$. A more stringent bound $\Delta c_{\gamma\pi^\circ} < 10^{-22}$ is obtained when one takes the upper value (including the total value 60 g/cm^2 [3] of systematic and statistical errors) for the observed depth $X_{\max}$ of the maximum. A more

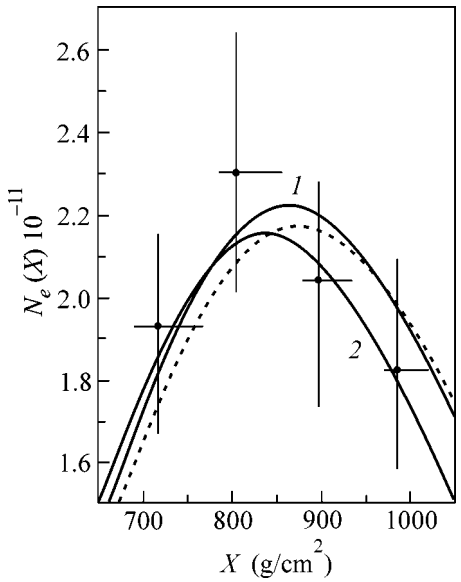

Fig. 1. The cascade curve for the $E = 3.2 \times 10^{20}$-eV GAS. The points with error bars are experimental data [3]. The dashed line is the standard variant of our calculations. Solid lines *1* and *2* were calculated with hypotheses 1 and 2, respectively [11].

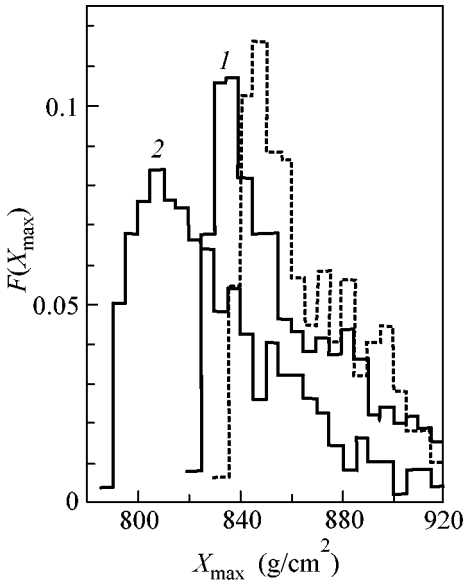

Fig. 2. The distributions of the depth $X_{\max}$ for (dashed line) standard variant and (solid lines *1* and *2*) with allowance made for hypotheses 1 and 2, respectively [11].

stringent bound cannot be obtained because the calculated results become virtually independent of the difference $\Delta c_{\gamma\pi^\circ}$ at small values of this difference. The bounds obtained for the difference of maximal attainable speeds of other particles are of approximately the same order of magnitude [27–29].

Finally, let us consider the dependence of the depth $X_{\max}$ of shower maximum on the energy E of PCR par-

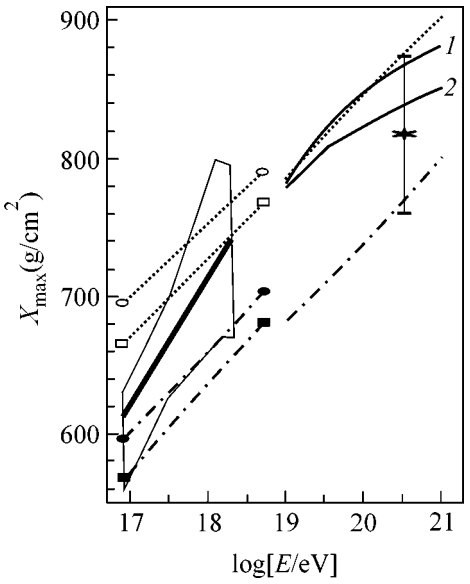

Fig. 3. The depth X_{max} of the shower maximum vs. log$E$, where E is the shower energy in electronvolts. The thick solid line is experimental data [30], the solid polygon around this line is the range of systematic and statistical errors. The dotted lines between open circles and squares are the calculations for primary protons in the hadron-interaction models SYBILL and QGSJet, respectively. The dash–dotted lines between closed circles and squares are the calculations for primary iron nuclei in the same models. The dotted and dash–dotted lines in the energy range 10^{19}–10^{21} eV are calculated in the standard variant for primary protons and primary iron nuclei, respectively. Solid lines *1* and *2* in this energy range are calculated with hypotheses 1 and 2 [11], respectively. The asterisks with error bars are experimental data for the shower described in [3].

ticles. Experimental data [30], which were obtained in the energy range $10^{17} - 2 \times 10^{18}$ eV, are shown by thick solid line in Fig. 3, where the solid polygon around this line is the range of systematic and statistical errors. The dotted lines between open circles and squares are the calculations [30] for primary protons in the hadron-interaction models SYBILL and QGSJet, respectively. The dash–dotted lines between closed circles and squares are the calculations for iron primary nuclei in the same models. An important characteristic of a shower is the variation ΔX_{max} in the depth of shower maximum when the energy E increases by an order of magnitude. This quantity is abbreviated as ER [31]. All the current models of hadron interactions give values $ER \sim 60$ g/cm^2 with a small error. Experimental data [30] provide the estimate $ER = 91.4 \pm (15.3) \pm 9.6$ g/cm^2, where the number in the parentheses is the systematic error and the latter term is the statistical error. Such a large value does not agree with any model of hadron interactions. A natural interpretation of this value consists in a hypothesis that the chemical composition of the PCRs changes from a heavy mixture dominated by iron nuclei at energies above 10^{17} eV to a light mixture dominated by protons at energies above 2×10^{18} eV. This interpretation is supported by an observed value $\alpha = 0.73 \pm 0.03$ of the exponent in the energy dependence $N_\mu \sim E^\alpha$ of the number of muons. Because various models give $\alpha \sim 0.85$, the observed α value can be attributed only to a change in the composition of the PCRs from a heavy mixture to a light one.

The dotted and dash-dotted lines in the energy range 10^{19}–10^{21} eV in Fig. 3 are our calculations in the standard variant for primary protons and primary iron nuclei, respectively. Because we use the QGS model, which does not take jets into account, Fig. 3 exhibits a slight decrease in the depth X_{max} compared to that expected in the QGSJet model [30]. Solid lines *1* and *2* in this energy range are our calculations with hypotheses 1 and 2, respectively. The asterisks with error bars are the experimental data for GAS of the highest energy $E \sim 3.2 \times 10^{20}$ eV [3]. As well as Figs. 1 and 2, Fig. 3 demonstrates that the calculations with hypotheses 1 and 2 do not contradict experimental data, and, therefore, the above-indicated bounds on the maximal attainable speeds of photons and neutral pions are valid.

Figure 3 allows one to analyze also various alternative hypotheses. First, the simplest alternative is the assumption that the highest energy particles of the PCRs are nuclei. However, the left part of Fig. 3 indicates that the primary particles of energies $E > 10^{19}$ eV are most likely protons, because the experimental data lie near the line for protons. The muon fraction in almost vertical 2.4×10^{20}-eV GAS, which was detected at AGASA [2], is also consistent with that calculated for a primary proton [32].

Second, another alternative possibility is a change in the hadron interactions in the ultrahigh-energy region. As is seen in Fig. 3, frequently used models SYBILL and QGSJet give larger values of the depth X_{max} than that in the QGS model, which is used in this study. Perturbative QCD calculations [33, 34] demonstrated that the QGS model leads to more rapid dissipation of the primary-particle energy and, therefore, underestimates the depth X_{max} compared to the QCD. Thus, to reduce the depth of shower maximum, the concept of hadron interactions should be changed considerably so as to increase the dissipation rate of primary-particle energy at ultrahigh energies. But such a change is beyond reason yet.

Third, one can assume that GASs are induced by primary photons arising, e.g., in the chain of decays of hypothetical very massive particles, which form dark matter in the Galaxy [20]. In view of this alternative, we note that a photon intersecting a magnetic field line in the Earth's magnetosphere generates an electron–photon cascade [35, 36]. As a result, instead of one particle, 100–1000 particles (electrons and photons), which are distributed in energy, fall on the atmosphere. These particles have characteristic energy $E \sim 10^{18}$ eV and induce

a shower with the depth $X_{max} \sim 870$ g/cm^2 of the maximum. This value scarcely fluctuates and, therefore, can hardly be consistent with an experimental estimate. For a cascade induced by a 3.2×10^{20}-eV photon, the depth is $X_{max} = 1100$ g/cm^2 disregarding the Landau–Pomeranchuk–Migdal effect and is considerably larger when this effect is taken into account. Thus, this hypothesis does not result in a decrease of the depth of maximum. Moreover, the fraction of muons in these showers should be approximately one-thirtieth of that in hadron-induced showers [37] if the cross section for photonuclear reactions is not assumed to sharply increase with energy. This cross section increases very slowly up to energies $E_\gamma \sim 10^{16}$ eV [38], and there are no reasons to assume that it sharply changes at $E_\gamma \sim 10^{18}$ eV. As was mentioned above, the fraction of muons in a 2.4×10^{20}-eV shower [2] corresponds to that calculated for protons and is approximately 30 times as large as that estimated for a shower induced by the primary photons. Moreover, an inclined 3×10^{20}-eV GAS [1], which was detected at the Yakutsk array, consists virtually of muons only. If this shower were induced by photons, its energy estimate would be larger by a factor of ~30, i.e., $E \sim 10^{22}$ eV, which is inconsistent with the array area ~10 km^2 and observation time ~10 years.

Finally, we note that the Chudakov effect [39] is of little importance.[1] Indeed, the minimal scattering angle of photons is $\theta_{min} \sim 1/\gamma$, where $\gamma \sim 10^{11}$ is the Lorentz factor. Therefore, the scattering occurs over the distance $r \sim d/\theta_{min} \sim 10^{-2}$ cm ($d \sim 10^{-13}$ cm is the characteristic nuclear dimension), which is much less than the free path $\lambda \sim 1$ km for the interaction of neutral pions in the rarefied atmosphere.

An idea of small Lorentz-invariance violation [11], proposed for overcoming the GZK paradox, which results in the stability of neutral pions at ultrahigh energies, can be tested through GAS data. Our analysis of the longitudinal development of GASs and distribution of the depth X_{max} of shower maximum demonstrates that possible violation is $\Delta c_{\gamma\pi^\circ} \le 10^{-20}$. A more stringent bound $\Delta c_{\gamma\pi^\circ} \le 10^{-22}$ is obtained when one takes the upper value (including the total systematic and statistical errors) for the observed depth X_{max} of the maximum [3].

Measurements of the depth of maximum at the new HiRes array [9] and at future arrays Auger [40], Telescope Array [41], Air Wath [42], etc., as well as more accurate QCD predictions for the interactions of ultrahigh-energy hadrons, will provide more stringent bounds.

We are grateful to G.T. Zatsepin for valuable comments and to I.M. Dremin, who proposed that we analyze the role of the Chudakov effect. This work was supported by the Russian Foundation for Basic Research (project 00-15-96632 for the scientific school of G.T. Zatsepin).

[1] Our attention to the Chudakov effect was kindly called by I.M. Dremin.

REFERENCES

1. N. N. Efimov, T. A. Egorov, A. V. Glushkov, *et al.*, in *Proceedings of the International Workshop on Astrophysical Aspects of the Most Energetic Cosmic Rays, Kofu 20*, 1990.
2. N. Hayashida, K. Honda, M. Honda, *et al.*, Phys. Rev. Lett. **73**, 3491 (1994).
3. D. J. Bird, S. C. Corbato, H. U. Dai, *et al.*, Astrophys. J. **424**, 491 (1994).
4. K. Greisen, Phys. Rev. Lett. **2**, 748 (1966).
5. G. T. Zatsepin and V. A. Kuz'min, Pis'ma Zh. Éksp. Teor. Fiz. **4**, 78 (1966) [JETP Lett. **4**, 53 (1966)].
6. G. R. Farrar and P. L. Biermann, Phys. Rev. Lett. **81**, 3579 (1998).
7. D. A. Kirzhnits and V. A. Chechin, Pis'ma Zh. Éksp. Teor. Fiz. **14**, 261 (1971) [JETP Lett. **14**, 172 (1971)].
8. D. A. Kirzhnits and V. A. Chechin, Yad. Fiz. **15**, 1051 (1972) [Sov. J. Nucl. Phys. **15**, 585 (1972)].
9. M. Takeda, N. Hayashida, K. Honda, *et al.*, Phys. Rev. Lett. **81**, 1163 (1998).
10. T. Abu-Zayyad, G. Archbold, K. Belov, *et al.*, in *Proceedings of the 26th International Cosmic Ray Conference, Salt Lake City, 1999*, Vol. 3, p. 264.
11. S. Coleman and S. L. Glashow, Phys. Rev. D **59**, 116008 (1999).
12. B. E. Schaefer, Phys. Rev. Lett. **82**, 4964 (1999).
13. J. Ellis, K. Farakos, N. E. Mavromatos, *et al.*, astro-ph/9907340 (1999).
14. O. Bertolami and C. S. Carvalho, gr-qc/9912117 (2000).
15. T. Kifune, astro-ph/9904164 (1999).
16. L. Gonzalez-Mestres, astro-ph/0011181 (2000).
17. V. Berezinsky, Nucl. Phys. B (Proc. Suppl.) **70**, 419 (1999).
18. T. W. Kephart and T. J. Weiler, Astropart. Phys. **4**, 271 (1996).
19. T. J. Weiler, hep-ph/9710431 (1997).
20. V. Berezinsky, M. Kachelriess, and V. Vilenkin, Phys. Rev. Lett. **79**, 4302 (1997).
21. V. A. Kuz'min and I. I. Tkachev, Pis'ma Zh. Éksp. Teor. Fiz. **68**, 255 (1998) [JETP Lett. **68**, 271 (1998)].
22. G. Amelino-Camelia, J. Ellis, N. E. Mavromatos, *et al.*, Nature **393**, 763 (1998).
23. R. Aloisio, P. Blasi, P. L. Ghia, *et al.*, Phys. Rev. D **62**, 053010 (2000).
24. G. Amelino-Camelia and T. Piran, hep-ph/0006210 (2000).
25. A. B. Kaĭdalov, K. A. Ter-Martirosyan, and Yu. M. Shabel'skiĭ, Yad. Fiz. **43**, 1282 (1986) [Sov. J. Nucl. Phys. **43**, 822 (1986)].
26. A. B. Migdal, Phys. Rev. **103**, 1811 (1956).
27. E. B. Brucker, P. F. Jacques, M. Kalelkar, *et al.*, Phys. Rev. D **34**, 2183 (1986).
28. R. Cowsik and B. V. Sreekantan, hep-ph/9811241 (1998).

29. T. Hambye, R. B. Mann, and U. Sarkar, Phys. Lett. B **421**, 105 (1998).
30. T. Abu-Zayyad, K. Belov, D. J. Bird, *et al.*, in *Proceedings of the 26th International Cosmic Ray Conference, Salt Lake City, 1999*, Vol. 5, p. 365.
31. J. Linsley, Phys. Rev. Lett. **10**, 146 (1963).
32. L. G. Dedenko, G. T. Zatsepin, T. M. Roganova, *et al.*, Pis'ma Zh. Éksp. Teor. Fiz. **61**, 233 (1995) [JETP Lett. **61**, 241 (1995)].
33. I. M. Dremin and W. J. Gary, Phys. Rep. **344**, 1 (2001).
34. I. M. Dremin, V. A. Nechitailo, M. Biyajima, *et al.*, Phys. Lett. B **403**, 149 (1997).
35. B. McBreen and C. J. Lambert, in *Proceedings of the 17th International Cosmic Ray Conference, Paris, 1981*, Vol. 6, p. 70.
36. T. Stanev and H. P. Vankov, Phys. Rev. D **55**, 1365 (1997).
37. N. Inoue for the AGASA Collab., in *Proceedings of the 26th International Cosmic Ray Conference, Salt Lake City, 1999*, Vol. 1, p. 357.
38. C. Caso, G. Conforto, A. Gurtu, *et al.*, Eur. Phys. J. C **3**, 206 (1998).
39. A. E. Chudakov, Izv. Akad. Nauk SSSR, Ser. Fiz. **19**, 650 (1955).
40. H. Bluemer, V. Bocci, J. Castro, *et al.*, in *Proceedings of the 26th International Cosmic Ray Conference, Salt Lake City, 1999*, Vol. 5, p. 345.
41. T. Aoki, Y. Arai, K. Arisaka, *et al.*, in *Proceedings of the 26th International Cosmic Ray Conference, Salt Lake City, 1999*, Vol. 5, p. 352.
42. L. Scarsi for the OA Collab., in *Proceedings of the 26th International Cosmic Ray Conference, Salt Lake City, 1999*, Vol. 2, p. 384.

Translated by R. Tyapaev

JETP Letters, Vol. 73, No. 9, 2001, pp. 451–452. Translated from Pis'ma v Zhurnal Éksperimental'noĭ i Teoreticheskoĭ Fiziki, Vol. 73, No. 9, 2001, pp. 511–512.

Dynamics of $\eta \longrightarrow 3\pi^0$ Decay

M. N. Achasov, K. I. Beloborodov, A. V. Berdyugin*, A. G. Bogdanchikov, A. V. Bozhenok, D. A. Bukin, S. V. Burdin, A. V. Vasil'ev, T. V. Dimova, A. A. Drozdetskiĭ, V. P. Druzhinin, V. B. Golubev, V. N. Ivanchenko, A. A. Korol', M. S. Korostelev, S. V. Koshuba, A. P. Lysenko, I. N. Nesterenko, E. V. Pakhtusova, A. A. Sal'nikov, S. I. Serednyakov, V. A. Sidorov, Z. K. Silagadze, A. G. Skripkin, Yu. V. Usov, V. V. Sharyĭ, and Yu. M. Shatunov

Budker Institute of Nuclear Physics, Siberian Division, Russian Academy of Sciences, pr. Akademika Lavrent'eva 11, Novosibirsk, 630090 Russia

** e-mail: berdugin@inp.nsk.su*

Received March 15, 2001

The $\eta \longrightarrow 3\pi^0$ decay was studied with the SND detector at the VEPP-2M e^+e^- collider. The parameter that describes deviation of the Dalitz plot of events from a uniform distribution was found to be $\alpha = -0.010 \pm 0.021 \pm 0.010$. © *2001 MAIK "Nauka/Interperiodica".*

PACS numbers: 13.25.Jx; 14.40.Aq

According to the one-loop approximation of the chiral perturbation theory, the Dalitz plot for $\eta \longrightarrow 3\pi^0$ events is uniform [1, 2]. However, when the final-state pion interaction is taken into account [3], the matrix element of this decay can be represented as

$$|M|^2 \propto 1 + 2\alpha z, \quad z = \frac{2}{3}\sum_{i=1}^{3}\left(\frac{3E_i - m_\eta}{m_\eta - 3m_{\pi^0}}\right)^2 = \frac{\rho^2}{\rho_{\max}^2},$$

where E_i is the energy of ith pion in the rest frame of the η meson and $\rho_{\max}$ is the maximum value of the distance ρ from the center of the Dalitz plot. This matrix element was previously examined in [4–7]. All values obtained for the parameter α are negative, and the maximum deviation of these values from zero is 2.5σ (see Table 1). Theoretical models [3] give $\alpha = -0.014$ and -0.007, where the second value is preferable because it includes higher order corrections.

In this work, the $\eta \longrightarrow 3\pi^0$ decay is examined in the process $e^+e^- \longrightarrow \phi \longrightarrow \eta\gamma$. An experiment was carried out at the VEPP-2M collider with the SND detector [8]. The accumulated integrated luminosity was 4.4 pb^{-1} in 1996 (PHI_96 experiment) and 8.7 pb^{-1} in 1998 (PHI_9801 and PHI_9802 experiments), which corresponds to 8.4×10^6 and 13×10^6 of produced ϕ mesons, respectively. The decay was analyzed and the relative probability of $\phi \longrightarrow \eta\gamma$ transition was determined in [9].

The Dalitz plot was analyzed under rather stringent conditions, which provide virtually total suppression of background. We selected seven-photon events, for which the polar angle was greater than 36° and 27° for the photon energy less and higher than 50 MeV, respectively. For selected events, kinematic reconstruction was performed under the assumption that the events are due to the process $e^+e^- \longrightarrow \eta\gamma \longrightarrow 3\pi^0\gamma \longrightarrow 7\gamma$. In [9], we demonstrated that, under these conditions, the detection efficiency of the process was 5%, which ensured determination of the relative decay probability of the $\phi \longrightarrow \eta\gamma$ decay without noticeable systematic shift. The number of events of the basic background process $\phi \longrightarrow K_S K_L$ is ~1% of the total number of selected events. Simulation demonstrates that the background events are uniformly distributed in the Dalitz plot. Figure 1 shows the energy distribution of reconstructed π^0 mesons in simulation and experiment. In [9], we found that inaccuracy in the efficiency determination provided a 2% error in the number of events of the effect.

After subtraction of the background, the distribution of events in the parameter z was constructed (see Fig. 2) and was analyzed as follows: the z interval was divided into ten parts, and then the number $N_j^{\exp}$ was compared with the calculated one $N_j^{thr} = \sum_{i=0}^{10} C\varepsilon_{ij}(1 + \alpha z_i) f_i$, where f_i is the phase-space volume; ε_{ij} is the matrix of the event detection efficiencies, which are determined from the

Table 1. The α values obtained in previous studies

	α	The number of events
Baglin *et al.* [4]	-0.32 ± 0.37	192
Alde *et al.* [5]	-0.022 ± 0.023	5×10^4
Abele *et al.* [6]	-0.052 ± 0.020	9.8×10^4
Teige *et al.* [7]	-0.005 ± 0.008	8.75×10^4

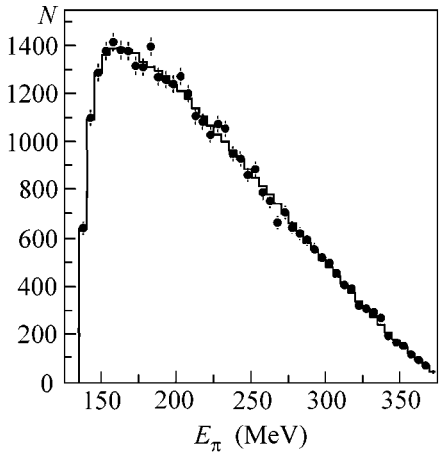

Fig. 1. The sum of the energy distributions of π^0 mesons. The histogram is the simulation and the points are the experimental data.

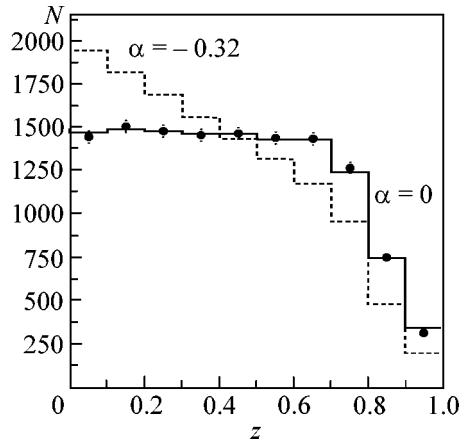

Fig. 2. The z distribution of events. The histogram is the simulation, and the points are the experimental data.

simulation; and $C = \sum_{i=1}^{10} N_i^{\exp} / \sum_{j=1}^{10} \sum_{i=1}^{10} \varepsilon_{ji}(1 + \alpha z_i) f_i$ is the normalization factor. The phase-space volume is calculated by the Monte Carlo method with an accuracy of 0.4%. The α parameter was determined by the maximum likelihood method. The likelihood function was constructed in terms of $N_i^{\exp}$ and N_i^{thr} in the form

$$F = \sum_{i=1}^{10} \left(N_i^{thr} - N_i^{\exp} + N_i^{\exp} \ln \frac{N_i^{\exp}}{N_i^{thr}} \right), \qquad (1)$$

and its minimum with respect to the only free parameter α was found. Table 2 presents the results of approximation. The α values that were obtained in three independent experiments agree with each other within the statistical errors. Joint approximation of data from all three experiments gives the value

$$\alpha = -0.010 \pm 0.021 \pm 0.010, \quad \chi^2/ndf = 4.4/9. \qquad (2)$$

The former error is the statistical error, and the latter one is systematic error, which is due to inaccuracy in simulation and statistical errors in ε_{ij}.

Table 2. The α values obtained in different experiments. Only statistical error is presented

Experiment	α	The number of events	χ^2/ndf
PHI_96	0.002 ± 0.035	4883	5.6/9
PHI_9801	-0.053 ± 0.035	3702	7.6/9
PHI_9802	0.030 ± 0.039	3916	5.7/9

Result (2) is consistent with data of other experiments [4–7] and theoretical predictions [3] but also agrees well with zero value of the parameter α. In this work, its error is determined by the experimental statistics. Therefore, the accuracy can be improved at larger integrated luminosity in the experiment $e^+e^- \longrightarrow \phi \longrightarrow \eta\gamma$.

This work was supported by the "Russian Universities" Foundation (project no. 3N-339-00) and by the Russian Foundation for Basic Research (project nos. 99-02-16813, 00-02-17478, and 00-02-17481).

REFERENCES

1. J. Gasser and H. Leutwyler, Nucl. Phys. B **250**, 539 (1985).
2. P. Di Vecchia *et al.*, Nucl. Phys. B **181**, 318 (1981).
3. J. Kambor, C. Wiesendanger, and D. Wyler, Nucl. Phys. B **465**, 215 (1996).
4. C. Baglin *et al.*, Nucl. Phys. B **22**, 66 (1970).
5. D. Alde *et al.*, Z. Phys. C **25**, 225 (1984).
6. A. Abele *et al.*, Phys. Lett. B **417**, 193 (1998).
7. S. Teige *et al.*, hep-ex/0002064.
8. N. N. Achasov *et al.*, Nucl. Instrum. Methods Phys. Res. A **449**, 125 (2000).
9. M. N. Achasov, S. E. Baru, K. I. Beloborodov, *et al.*, Pis'ma Zh. Éksp. Teor. Fiz. **72**, 411 (2000) [JETP Lett. **72**, 282 (2000)].

Translated by R. Tyapaev

JETP Letters, Vol. 73, No. 9, 2001, pp. 453–456. Translated from Pis'ma v Zhurnal Éksperimental'noĭ i Teoreticheskoĭ Fiziki, Vol. 73, No. 9, 2001, pp. 513–516.

Estimate of the Δ(1232) Component in the ^{12}C Nucleus

V. M. Bystritsky[1], I. V. Glavanakov[2], P. Grabmayr[3], Yu. F. Krechetov[2,*], O. K. Saigushkin[2], A. N. Tabachenko[2], A. I. Fix[4], and E. N. Schuvalov[2]

[1] *Joint Institute for Nuclear Research, Dubna, Moscow region, 141980 Russia*

[2] *Research Institute of Nuclear Physics, Tomsk Polytechnical University, Tomsk, 634050 Russia*

** e-mail: krechet@npi.tpu.ru*

[3] *Institute of Physics, Tübingen University, D-72076 Tübingen, Germany*

[4] *Tomsk Polytechnical University, Tomsk, 634034 Russia*

Received March 22, 2001

The cross section for the ^{12}C(γ, π^+p) reaction was measured in the range of the Δ(1232) isobar. The data were analyzed using the models taking into account the nucleon and isobaric degrees of freedom of the ^{12}C nucleus. The conclusion is drawn that in the large-momentum transfer range the π^+p pairs are produced in the course of the direct knocking-out of Δ^{++} isobar from the nucleus. The probability of finding the Δ isobar in the ground-state ^{12}C nucleus is estimated at 0.018 ± 0.005 Δ isobars per nucleon. © *2001 MAIK "Nauka/Interperiodica".*

PACS numbers: 25.20.Lj; 21.30.-x

The isobaric degrees of freedom in nuclei are part of the fundamental problem of nucleon–nucleon interaction at medium and short distances (see reviews [1, 2]). The exchange of π and ρ mesons between nucleons may give rise to the virtual *N*Δ and ΔΔ states. In 1971, Gerasimov suggested using the process of isobar knocking-out by high-energy particles for studying the isobaric degrees of freedom in nuclei [3]. Theoretical estimates [4, 5] and the results of a few experiments on setting off the mechanism of direct isobar knocking-out [6, 7] gave a value of 0.5–4% for the contribution of Δ-isobaric states to the wave function of *p*-shell nuclei. Such a small value hampers experimental observation of the Δ component in the collisions of particles with nuclei. The main difficulty consists in setting off the background reaction mechanisms. We solved this problem by measuring the cross section for π^+p-pair production in the reaction

$$\gamma + {}^{12}\mathrm{C} \longrightarrow \pi^+ + p + \mathrm{X} \qquad (1)$$

in the range of large momentum transfer to the residual nucleus X. The idea of the experiment is that the direct production of π^+p pairs by the nucleons in a nucleus is forbidden for reaction (1), whereas the background is concentrated in the small-momentum transfer range.

The experiment was conducted on an electron bremsstrahlung beam of the Tomsk synchrotron. The experimental setup included two channels for detecting the positive pion–proton coincidences in the coplanar geometry.

Positive pions with an average momentum of 181 MeV/s were detected by a strongly focusing magnetic analyzer [8] arranged at an angle of 54° to the photon beam axis. Angular and momentum acceptances of the analyzer were 3×10^{-3} sr and 24%, respectively. The pion momentum was measured with an accuracy of ~1% using a scintillation hodoscope placed in the focal plane of the analyzing magnet.

Protons with energies in the range T_p = 50–130 MeV were detected by a (Δ*E*, *E*) scintillation spectrometer at an angle $\theta_p = (75 \pm 19)°$ to the photon beam axis. The solid angle in the proton channel was determined by the Δ*E* detector and chosen to be 0.26 sr. The *E* detector of the proton spectrometer consisted of three counters arranged one above the other, each with a scintillator of size $10 \times 10 \times 50$ cm. A joint analysis of the pulse amplitudes in the photomultipliers of the Δ*E* and *E* detectors facing each of the scintillators on both sides allowed one to determine the polar angle and the energy of a proton. The accuracies of measured proton energy (σ_T) and proton emission angle (σ_θ) were 4 MeV and 3°, respectively. The accuracy $\sigma_\phi \sim 2°$ of measuring the azimuthal emission angle of a proton was determined by the vertical size of the *E* counter.

For monitoring the stability of (Δ*E*, *E*)-spectrometer operation, two auxiliary narrow scintillation counters with absorbers were placed behind the spectrometer. In parallel with the accumulation of the π^+p events, the pulse amplitude spectra were measured for the Δ*E* and *E* detectors, which were triggered by the coincident spectrometer and auxiliary counter pulses. Two portions of these spectra were identified and monitored, one corresponding to pions and another to the lowest energy protons. This energy was determined by the absorbers and chosen within the spectrometer operating range.

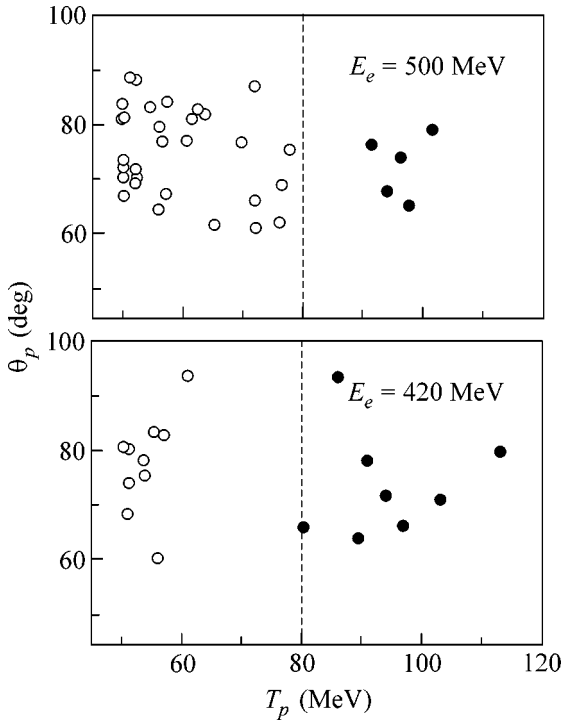

Fig. 1. Distribution of events over the proton emission angle θ_p and its kinetic energy T_p for two electron energies E_e. The events shown by the black circles were used to estimate the experimental reaction cross section.

To reduce the cosmic-ray background, a large-area scintillation veto counter was placed over the detectors in the pion channel. For the same purpose, the final trigger was formed only during the accelerator pulse. This allowed the cosmic-ray background to be reduced down to a level of 2%.

A graphite plate of natural isotope composition, with a thickness of 4.35×10^{22} nucleus/cm^2 for the photon beam, was used as a target. The total energy of the photon beam was measured by a gauss quantometer [9] with an accuracy of 3%. The $^{12}C(\gamma, \pi^+p)$-reaction events were accumulated at two electron energies E_e = 420 and 500 MeV. The accidental coincidence level depended on the energy of detected protons and was determined by the intensity of events beyond the π^+p-coincidence correlation peak. Its magnitude in the operating range changed from 6% at T_p = 50 MeV to 1% at T_p > 80 MeV.

Fifty-two π^+p coincidences were detected in the experiment. Figure 1 demonstrates their distribution over the proton exit angle and energy.

With the aim of determining the kinematic region where the reaction mechanisms caused by nonnucleon degrees of freedom may dominate, analysis was carried out of the contributions from the background π^+p-production mechanisms. For this purpose, we employed a model described in [10] (see also [11–13]). This model takes into account the one-, two-, and three-nucleon modes of incident-photon absorption and the single-pion production on nucleons, as well as the pion and nucleon rescattering by the residual nucleus. The cross sections for background reactions were calculated for the photon energies E_γ = 400 and 450 MeV and averaged over the proton polar angles θ_p = 56°–94° and pion energies T_π = 71.5–106.5 MeV; the results are presented in Fig. 2. The background is mainly due to the π^+n- or π^0p-pair production followed by charge-exchange rescattering of a neutron into a proton or a π^0 meson into a π^+ meson. According to the calculation, the background is concentrated in the range of small momentum transfer.

To analyze the data for E_e = 500 MeV, we took into account the background caused by the pion-pair production in the $^{12}C(\gamma, \pi^+p)\pi^{-11}B$ reaction (it is absent at E_e = 420 MeV). The corresponding cross section, calculated using the DWIA model [14], is shown in Fig. 2 by the dot-and-dash curve.

Based on the results of these calculations, the boundary of the kinematic region was chosen at T_p = 80 MeV (shown by the dashed line in Fig. 1), beyond which (at higher proton energies and, correspondingly, larger momentum transfer) the contribution from the π^+p-production background does not exceed 3% of the experimental reaction yield at E_e = 500 MeV and is negligible at E_e = 420 MeV. Because of this, further analysis was carried out for the events that fell within the region to the right of the dashed line in Fig. 1.

The experimental cross section for the π^+p-pair production in reaction (1) was averaged in the following kinematic intervals:

$$\begin{aligned} T_p &= 80\text{–}120 \text{ MeV}; \\ T_\pi &= 71.5\text{–}106.5 \text{ MeV}; \\ \theta_p &= 56°\text{–}94°. \end{aligned} \qquad (2)$$

Based on the data obtained for two electron energies E_e = 420 and 500 MeV, the cross section was found to be

$$\frac{d^3\sigma}{dE_p d\Omega_p \Omega_\pi} = 8.5 \pm 2.4 \pm 0.5 \ \frac{\text{nb}}{\text{MeV sr}^2}. \qquad (3)$$

For the events in the indicated kinematic region, the average photon energy E_γ was 355 MeV. Experimental cross section (3) is shown in Fig. 2 by the dot. The vertical bar denotes the total error of measuring cross sections, and the horizontal bar is the standard deviation obtained for T_p on the assumption that the events are uniformly distributed over the averaging interval.

Figure 3 shows the distribution of events over the invariant masses of π^+p pair. One can see that the events in region (2) fall within the range of $\Delta(1232)$-resonance masses. For this reason, we assume that the considerable experimental reaction yield in this region is due to the isobaric nuclear degrees of freedom.

The experimental cross section for reaction $^{12}C(\gamma, \pi^+p)$ measured in kinematic region (2) was analyzed within the framework of a model described in [15, 16]. This model is based on the assumption that the $\gamma\Delta^{++} \longrightarrow \pi^+p$ process, where the incident photon is absorbed by the nuclear Δ^{++} isobar, is the dominant mechanism of our reaction in the large-momentum transfer range. This approach was implemented in a practical manner within the framework of impulse approximation and using the closure relation when summing over the experimentally undetectable final nuclear states. In this case, the following expression holds for the squared modulus of reaction amplitude in Eq. (1):

$$\overline{|M_{fi}|^2} = \rho_\Delta(\mathbf{p}) f_\pi f_p \overline{|T_{\gamma\Delta\to\pi p}|^2}. \quad (4)$$

Here, f_i ($i = \pi, p$) are the suppression factors accounting for the particle absorption in nucleus; they are functions of the pion and proton kinetic energies, respectively. The function $\rho_\Delta(\mathbf{p})$ denotes the momentum distribution for the Δ^{++} isobar in the ground-state ^{12}C nucleus. The amplitude $T_{\gamma\Delta\to\pi N}$ of elementary $\gamma\Delta^{++} \longrightarrow \pi^+p$ process was calculated using the diagrammatic technique in the nonrelativistic approximation [15, 16].

The momentum distribution ρ_Δ in Eq. (4) was written as

$$\rho_\Delta(\mathbf{p}) = 4\frac{4}{3}\pi R^3 n_\Delta^c(\mathbf{p}). \quad (5)$$

Here, $n_\Delta^c(\mathbf{p})$ are the occupation numbers of the Δ isobar with momentum p in the ^{12}C nucleus with effective radius R, which was chosen to be 3.2 fm.

Because of the lack of literature data on the momentum distribution ρ_Δ in p-shell nuclei, we used the results of work [17], where the occupation numbers $n_\Delta^m(p)$ are given for the Δ(1232)-isobar states of nuclear matter. It was assumed that $n_\Delta^m(p)$ and $n_\Delta^c(p)$ are linearly related to each other taking into account that the densities of the nuclear matter and the ^{12}C nucleus are different. The momentum distribution ρ_Δ was normalized as

$$\int \rho_\Delta(\mathbf{p}) \frac{d\mathbf{p}}{(2\pi)^3} = \alpha A N_\Delta^c, \quad (6)$$

where $A = 12$ is the mass number of the target nucleus and N_Δ^c is the number of Δ isobars per nucleon in the ^{12}C nucleus. The α multiplier stands for the ratio of the number of Δ^{++} isobars to the total number of Δ isobars in the nucleus. It follows from the $SU(2)$ symmetry of the $NN \longrightarrow N\Delta$ process that $\alpha = 15/64$ (see also [7]).

To compare the expected reaction cross section due to the isobaric nuclear degrees of freedom with the cross section for background reactions and the experimental cross section, the cross section calculated for the $^{12}C(\gamma, \pi^+p)$ reaction in the above-mentioned approximations is shown in Fig. 2 as a function of proton energy. The cross section is averaged over the proton exit angle and the pion energy, according to Eq. (2). The calculations were performed with the value $N_\Delta^c = 0.015$ that was experimentally measured for the pion double charge-exchange [7]. One can see in Fig. 2 that the cross-section maximum due to the π^+p-pair production by knocking out the Δ isobar with a photon is strongly shifted to higher proton energies and, hence, is well-defined kinematically. The experimental cross section at $T_p > 80$ MeV is almost two orders of magnitude larger than the theoretical estimates obtained with the models allowing for only the nucleon degrees of freedom in the ^{12}C nucleus. This fact, being particularly important for low-intensity signals, is one of the main advantages of the method used in this work.

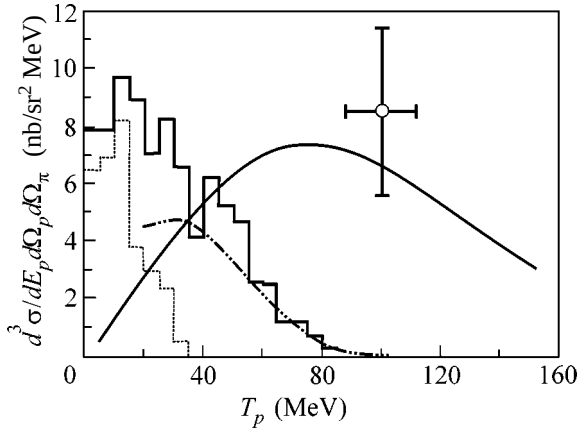

Fig. 2. Differential cross section for the $^{12}C(\gamma, \pi^+p)$ reaction: the solid and dotted histograms correspond to the single-pion production at $E_\gamma = 400$ and 450 MeV, respectively, in the model [10] based on the nucleon degrees of freedom; the dot-and-dash curve corresponds to the pion-pair production; the solid line corresponds to the model of direct knocking-out of the Δ(1232) isobar; and the dot is for the experimental cross section.

The computational results presented in Fig. 3 for the cross section dependence on the invariant mass of π^+p pair indicate that the model used does not contradict the experimental data.

Considering the aforesaid and regarding the quantity N_Δ^c in Eq. (6) as a free parameter, we determined its value on the condition for best coincidence between the calculated and the measured cross section (3):

$$N_\Delta^c = 0.018 \pm 0.005 \pm 0.001\ \Delta \quad (7)$$

isobars per nucleon.

The resulting N_Δ^c value agrees well with the estimate made in [7].

The systematic error in Eq. (7) is due to the measurement procedure. The use of physical constants and

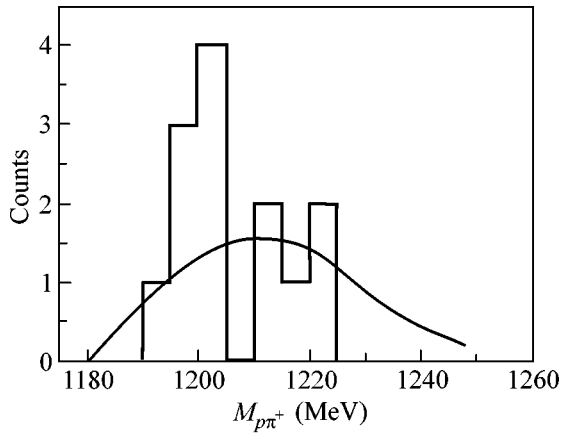

Fig. 3. Distribution of events over the π^+p-pair invariant masses. The curve corresponds to the model of direct knocking-out of the isobar from the nucleus.

methods of calculation of some low-accuracy nuclear effects is another source of a sizable systematic error in the reaction model. In particular, our estimates show that the systematic error introduced by the uncertainty in magnetic moment of the Δ^{++} isobar and in the final-state interaction is 0.006 Δ isobars per nucleon.

This work was supported by the Russian Foundation for Basic Research, project nos. 96-02-16742, 97-02-17765, and 99-02-16964.

REFERENCES

1. A. M. Green, Rep. Prog. Phys. **39**, 1109 (1976).
2. H. J. Weber and H. Arenhövel, Phys. Rep. **36**, 277 (1978).
3. S. B. Gerasimov, Pis'ma Zh. Éksp. Teor. Fiz. **14**, 385 (1971) [JETP Lett. **14**, 260 (1971)].
4. G. Horlacher and H. Arenhövel, Nucl. Phys. A **300**, 348 (1978).
5. M. R. Anastasio, A. Faessler, H. Müther, *et al.*, Nucl. Phys. A **322**, 369 (1979).
6. A. I. Amelin, M. N. Behr, B. A. Chernyshov, *et al.*, Phys. Lett. B **337**, 261 (1994).
7. C. I. Morris, J. D. Zumbro, J. A. McGill, *et al.*, Phys. Lett. B **419**, 25 (1998); E. A. Pasyuk, R. L. Boudrie, P. A. M. Gram, *et al.*, nucl-ex/9912004 (1999).
8. S. V. Kolmogorova, Yu. F. Krechetov, and G. A. Saruev, Available from VINITI No. 340-83 (1983).
9. A. P. Komar, S. P. Kruglov, and I. V. Lopatin, *Measuring of Total Energy of Bremsstrahlung Beams from Electron Accelerators* (Nauka, Leningrad, 1972).
10. R. Carrasco, M. J. Visente Vacas, and E. Oset, Nucl. Phys. A **570**, 701 (1994).
11. R. Carrasco and E. Oset, Nucl. Phys. A **536**, 385 (1992).
12. E. Oset and L. L. Salcedo, Nucl. Phys. A **468**, 631 (1987).
13. M. Liang, D. Branford, T. Davinson, *et al.*, Phys. Lett. B **411**, 244 (1997).
14. I. V. Glavanakov, Yad. Fiz. **63**, 2187 (2000) [Phys. At. Nucl. **63**, 2091 (2000)].
15. A. Fix, I. Glavanakov, and Yu. Krechetov, Nucl. Phys. A **646**, 417 (1999).
16. A. Fix, I. Glavanakov, Yu. Krechetov, *et al.*, nucl-ex/9912013 (1999).
17. R. Cenni, F. Conte, and U. Lorenzini, Phys. Rev. C **39**, 1588 (1989).

Translated by V. Sakun

JETP Letters, Vol. 73, No. 9, 2001, pp. 457–460. Translated from Pis'ma v Zhurnal Éksperimental'noĭ i Teoreticheskoĭ Fiziki, Vol. 73, No. 9, 2001, pp. 517–520.

X-ray Spectrum Determination from the Angular Dispersion of Radiation in a Diamond Prism

A. G. Tur'yanskiĭ*, I. V. Pirshin, R. A. Khmel'nitskiĭ, and A. A. Gippius

Lebedev Physical Institute, Russian Academy of Sciences, Leninskiĭ pr. 53, Moscow, 117924 Russia

** e-mail: tour@mail1.lebedev.ru*

Received March 27, 2001

The X-ray spectrum of hard polychromatic radiation with energies of up to 40 keV was obtained from the angular dispersion of the radiation beam in a diamond prism. In contrast to the classical optical scheme, the beam to be analyzed is passed through the entrance face of the prism without refraction and is directed onto the exit face at a glancing angle $\sim(2\delta)^{1/2}$, where δ is the real part of the decrement of the refractive index for the short-wavelength edge of the spectrum. The spectrum distortions caused by the intersection of the reciprocal lattice points by the Ewald sphere at a fixed number of wavelengths λ are minimized by the use of the angular divergence of the beam of ~10′ in the plane perpendicular to the refraction plane. In the energy range of 8–9 keV, an energy resolution of less than 100 eV was obtained, which exceeds the corresponding parameter for cooled semiconductor detectors. The measuring scheme suggested makes it possible to solve the problem of the analysis of spectra of directional X-ray beams when studying fast nonstationary generation processes. © *2001 MAIK "Nauka/Interperiodica"*.

PACS numbers: 07.85.Nc; 07.60.Hv; 41.50.+h

INTRODUCTION

The possibility of determining the spectra of hard X-ray radiation using the prism-spectrometer method that is well known in optics [1] has scarcely been considered to date. This is explained by the smallness of the real part of the decrement δ of the refractive index of any substance in the X-ray range ($10^{-6} \le \delta \le 10^{-5}$ for the radiation energy $E \sim 10$ keV) and by the spread of the dispersion picture because of diffraction effects at the edges of the refracting sample [2–4]. It was shown in our previous work [5] that the X-ray optical parameters of diamond single crystals make it possible, first, to minimize the influence of diffraction effects at the refracting face and, second, to obtain refraction contraction and a multiple increase in angular dispersion using beams that strike the refracting interface from the inside of the prism at a glancing angle $\theta < \theta_c(E)$ (where θ_c is the critical angle of the total external reflection).

In this work, we realized the scheme of a prismatic X-ray spectrometer in a practical manner and obtained the full spectrum of a polychromatic beam with an energy $E > 6$ keV, including bremsstrahlung and fluorescent lines, from the angular dispersion of radiation in a diamond prism.

RESULTS AND DISCUSSION

Figure 1 displays the experimental scheme of the spectrometer. The dispersion element is a rectangular diamond prism *5* cut along {110} planes and having optically polished faces. The exit surface of the prism facing the absorbing shield *6* had the dimensions of 2 and 5 mm along the beam and in the perpendicular direction, respectively. As a source of polychromatic radiation, an X-ray tube with a copper anode was used. The voltage at the tube was changed in steps from 15 to 40 kV. The angle γ at which the X-ray beam exits the anode, as measured from the anode mirror, was 5°. The radiation was detected with a scintillation counter *12* based on an NaI(Tl) crystal, which ensured a detection efficiency of more than 85% in the range of 6–33 keV. Prism *5* and detector *12* were placed on goniometers *4* and *10*, respectively, whose rotation axes were directed along the primary beam. This geometry permitted us to increase the accuracy of measuring small deviation angles by a factor of $(s + r)/s$, where s is the distance between the axes O_1 and O_2, and r is the distance from the axis O_2 to the entrance slit *11* of the detector *12*. The monochromator *7* and detector *9*, which could be rotated about the axis O_1, were used to adjust the spectrometer to the monochromatic spectrum line employed.

The full widths at half-maximum (FWHMs) of the beam in the measuring plane (which coincided with the

0021-3640/01/7309-0457$21.00

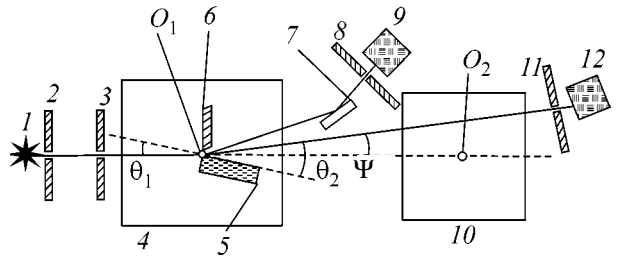

Fig. 1. Experimental scheme of measuring angular dispersion: (*1*) X-ray tube focus; (*2*, *3*, *8*, *11*) vertical collimating slits; (*4*, *10*) goniometers; (*5*) sample (prism); (*6*) absorbing shield; (*7*) monochromator; and (*9*, *12*) detectors of radiation.

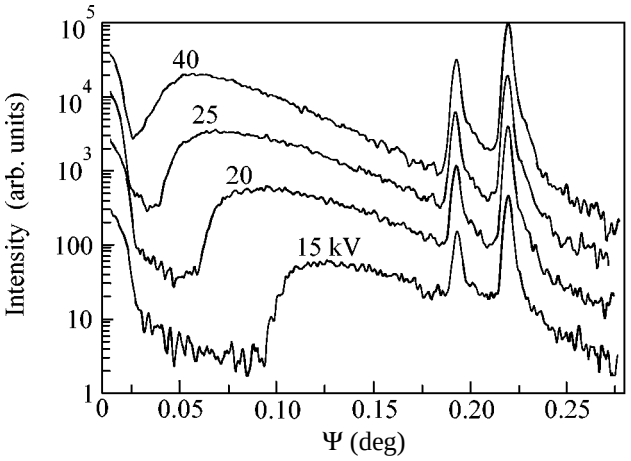

Fig. 2. Angular diagrams of the intensity of refracted radiation at various voltages at the X-ray tube with a copper anode.

plane of paper; see Fig. 1) and in the perpendicular direction, $\Delta\theta_p$ and $\Delta\theta_s$, were 25″ and 1200″, respectively. For these values of $\Delta\theta_p$ and $\Delta\theta_s$, the depths of diffraction dips in the angular dependence of the transmission coefficient of the prism upon rocking when using the Cu$K_{\alpha 1}$ line (8048 eV) did not exceed 20% of the average value in adjacent angular positions. The deepest dips corresponded to the energy band ΔE_d = 3–10 eV. As will be shown below, in spectral decomposition, the condition $\Delta E_d \ll \Delta E$ is fulfilled, where ΔE is the energy resolution of the prism spectrometer. This ensures a virtually complete smoothing of diffraction dips in the continuous spectrum that are caused by the intersection of the reciprocal lattice points of diamond by the Ewald sphere for a discrete set of bands of the spectrum.

The X-ray beam was directed onto the entrance side face of the prism at an incidence angle $\varphi = 3''$. With the above-indicated orientation of the prism, the deviation angle of the primary beam for the typical wavelength ~0.1 nm is ~0.001″; i.e., it is negligible in comparison with φ. Therefore, we have $\theta_1 \cong \varphi$, where θ_1 is the glancing angle between the plane of the exit face of the prism and the central ray of the beam to be analyzed. When calculating the deviation angle of the primary beam ($\Psi = \theta_2 - \theta_1$; see Fig. 1), the contribution of the imaginary part of the decrement of the refractive index $i\beta$ can be neglected, since in the energy range studied ($E > 6$ keV) the following condition is fulfilled for diamond: $\delta(E) \gg |i\beta(E)|$. Passing in the sine law from the sines of angles to the glancing angles themselves and using a series expansion at $\theta_1 \ll \pi/2$, we obtain the expression for the angle of deviation of the primary beam after transmission through the prism:

$$\Psi \cong \sqrt{\theta_1^2 + \frac{KZ\rho}{AE^2}} - \theta_1, \qquad (1)$$

where K is the dimensional coefficient, Z is the atomic number of the material of the refracting medium, ρ is the density of the material of the prism, and A is the atomic weight. Designating $C = KZ\rho/A$ and differentiating Eq. (1) with respect to E, we obtain the following formula for the angular dispersion of the rectangular prism:

$$D(E, \theta_1) = d\Psi/dE = -\frac{2C}{E^3\sqrt{\theta_1^2 + 2C/E^2}}. \qquad (2)$$

Figure 2 shows the angular diagrams of the intensities of the analyzed beam after the radiation passes through the prism for various voltages at the X-ray tube. The intense peaks in the diagram are due to the fluorescent copper lines (CuK_α doublet at 8028 and 8048 eV and the CuK_β line at 8906 eV); the rise in the intensity at small angles Ψ is due to the passage of part of the direct beam over the prism. As the voltage increases, the intensity of the bremsstrahlung part of the spectrum increases and the short-wavelength edge is shifted toward smaller angles Ψ.

Using expressions (1) and (2), we can pass from angular intensity distributions shown in Fig. 2 to the energy spectrum $S(E) = d^2N(E)/dEd\Omega$ measured in a given direction, where $d^2N(E)$ is the number of X-ray photons in the range (E, $E + dE$) that fall into a solid angle $d\Omega$ depending on the distance between the source of radiation and the prism and on the area of the entrance aperture of the spectrometer.

In the scheme used in this work, the effective width of the entrance aperture of the spectrometer $d_{\text{eff}}(E)$ is determined by the absorption of the radiation in the prism $A(E)$ and by the Fresnel transmission coefficient $T(E)$ at the exit face. The magnitude of $A(E)$ can easily be found in terms of geometric optics by solving the problem of beam transmission through an absorbing rectangular wedge [6]. The $T(E)$ dependence on the

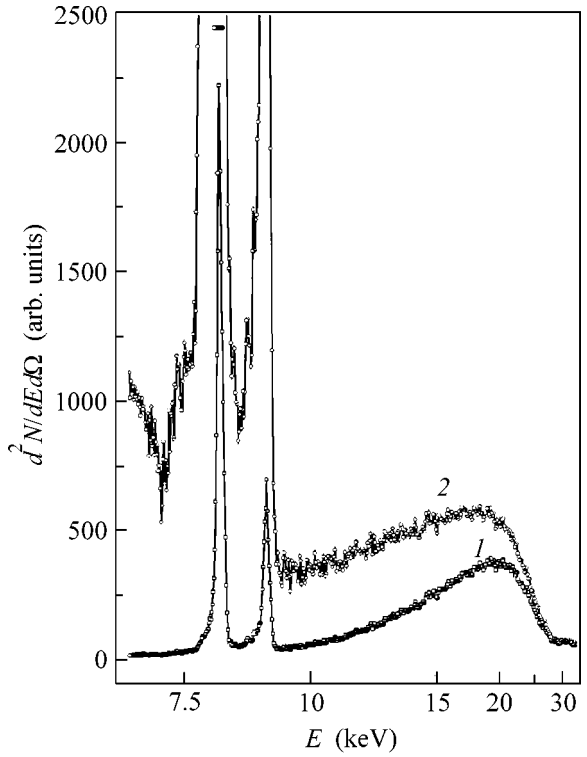

Fig. 3. Energy spectra of an X-ray tube with a copper anode and the escape angle of 5° at the voltage at the tube of 30 kV: (*1*) at the entrance window of the detector of radiation at a distance of 135 cm from the tube focus and (*2*) at the exit window of the X-ray tube.

glancing angle can be obtained from the Fresnel formulas [2, 3] by expanding into a power series at $\theta_1 = 0$:

$$A(E) = \int_0^L e^{-\frac{\mu(E)\rho y}{\cos\theta_1}} dy, \quad (3)$$

$$T(E) \cong 1 - \left\{ \frac{\sqrt{\theta_1^2(E) + 2\delta(E)} - \theta_1}{\sqrt{\theta_1^2(E) + 2\delta(E)} + \theta_1} \right\}^2, \quad (4)$$

where $\mu(E)$ is the energy dependence of the mass absorption coefficient, ρ is the density of the material of the prism, and y is the current coordinate for the beam outgoing from the refractive face of the prism. Note that, at the glancing angles θ_1 used in this work, the difference between the $T(E)$ values for the *s* and *p* polarizations is negligible and, therefore, the refracted spectrum is virtually polarization-independent.

Figure 3 displays the experimental energy spectrum (at a voltage at the tube equal to 30 kV) recorded by detector *12* (curve *1*) and the initial spectrum (curve *2*) at the exit window of the X-ray tube. Spectrum *2* was obtained from curve *1* with allowance for the dependences (3) and (4) and for the absorption in air and in the beryllium window (0.5 mm thick) of detector *12*. At E = 8990 eV, a jump of photoabsorption in copper is observed. Since the exit angle of the beam with respect to the anode mirror of the tube is relatively small, the absorption in the material of the anode exerts a significant effect on the shape of the spectrum. In particular, this leads to the appearance of a minimum in the bremsstrahlung part of the spectrum near the CuK_β fluorescent line. The observed asymmetry of spectral lines is mainly caused by the deviation of the refracting face from flatness near the prism edge.

With allowance for the instrument function, the energy resolution ΔE, characterized by the FWHM of the CuK_α line, is 97 eV, which is approximately half as large as the corresponding parameter for cooled semiconductor silicon detectors [7, 8]. This resolution is by no means limiting; an estimation shows that it can reach values of less than 40 eV with decreasing angular divergence in the plane of incidence.

The dependences shown in Figs. 2 and 3 were obtained by continuous angular scanning by the entrance slit. It is obvious that the replacement of a single-channel detector by a linear array or a matrix of detectors covering the entire angular range of the motion of the entrance slit will permit one to reject the angular rotation and, consequently, record a pulsed spectrum in a given direction without any restrictions on the duration of the pulse. Note that such a problem cannot be solved by using analyzing crystals, since, if the direction of recording is fixed in accordance with the Bragg diffraction condition, a change in the angle of rotation of the analyzing crystal is required.

CONCLUSION

The main results of this work are as follows.

(1) On the basis of a diamond prism, a scheme of a prism X-ray spectrometer was realized in a practical manner and spectra of hard X-ray radiation were obtained from the data on angular dispersion.

(2) In the energy range of 8–9 keV, an energy resolution of 97–106 eV was reached, which is half as large in comparison with that of cooled semiconductor detectors. This provides the possibility of practical application of such a prism spectrometer for analyzing spectra of intense X-ray sources.

(3) It is shown that the prism scheme with a linear array of detectors can be used for recording X-ray spectra in a given direction without any restrictions on the duration of the exciting pulse.

ACKNOWLEDGMENTS

This work was supported in part by the CRDF (grant no. RP2-2105).

REFERENCES

1. A. N. Zaĭdel', G. V. Ostrovskaya, and Yu. I. Ostrovskiĭ, *Technique and Practice of Spectroscopy* (Nauka, Moscow, 1976).
2. M. A. Blokhin, *Physics of X-rays* (GITTL, Moscow, 1957).
3. S. A. Akhmanov and S. Yu. Nikitin, *Physical Optics* (Mosk. Gos. Univ., Moscow, 1998).
4. A. G. Tur'yanskiĭ and I. V. Pirshin, Prib. Tekh. Éksp., No. 5, 90 (2000).
5. A. G. Tur'yanskiĭ, I. V. Pirshin, R. A. Khmel'nitskiĭ, and A. A. Gippius, Fiz. Tverd. Tela (St. Petersburg) **43** (2001) [Phys. Solid State **43**, 644 (2001)].
6. A. G. Tur'yanskiĭ and I. V. Pirshin, Prib. Tekh. Éksp., No. 6, 104 (1999).
7. D. V. Gryaznov and A. V. Lupilov, Prib. Tekh. Éksp., No. 6, 97 (2000).
8. Yu. K. Akimov, O. V. Ignat'ev, A. I. Kalinin, and V. F. Kushniruk, *Semiconductor Detectors in Experimental Nuclear Physics* (Énergoatomizdat, Moscow, 1989).

Translated by S. Gorin

JETP Letters, Vol. 73, No. 9, 2001, pp. 461–464. Translated from Pis'ma v Zhurnal Éksperimental'noĭ i Teoreticheskoĭ Fiziki, Vol. 73, No. 9, 2001, pp. 521–525.

Phonons in Ge/Si Superlattices with Ge Quantum Dots

A. G. Milekhin[1,*], A. I. Nikiforov[1], O. P. Pchelyakov[1], S. Schulze[2], and D. R. T. Zahn[2]

[1] *Institute of Semiconductor Physics, Siberian Division, Russian Academy of Sciences, pr. Akademika Lavrent'eva 13, Novosibirsk, 630090 Russia*

** e-mail: milekhin@thermo.isp.nsc.ru*

[2] *Institut für Physik, Technische Universität Chemnitz, D-09107 Chemnitz, Germany*

Received March 7, 2001; in final form, March 20, 2001

Ge/Si superlattices containing Ge quantum dots were prepared by molecular beam epitaxy and studied by resonant Raman scattering. It is shown that these structures possess vibrational properties of both two- and zero-dimensional objects. The folded acoustic phonons observed in the low-frequency region of the spectrum (up to 15th order) are typical for planar superlattices. The acoustic phonon lines overlap with a broad emission continuum that is due to the violation of the wave-vector conservation law by the quantum dots. An analysis of the Ge and Ge–Si optical phonons indicates that the Ge quantum dots are pseudoamorphous and that mixing of the Ge and Si atoms is insignificant. The longitudinal optical phonons undergo a low-frequency shift upon increasing laser excitation energy (2.54–2.71 eV) because of the confinement effect in small-sized quantum dots, which dominate resonant Raman scattering. © *2001 MAIK "Nauka/Interperiodica".*

PACS numbers: 63.22.+m; 78.67.Hc; 78.30.Fs

In the last few years, semiconductor Ge/Si structures have been intensively studied because of their potential use in optoelectronic devices compatible with silicon technology. Their vibrational properties are well studied and understood [1–3]. It was recently demonstrated that molecular beam epitaxy allows one to prepare, under certain growth conditions, dislocation-free Ge quantum dots (QDs) of various size (8–95 nm in base and 1–7 nm in height) [4–6]. It is expected that the Ge/Si superlattices (SLs) containing Ge QDs should combine QD advantages over the Ge/Si SL and, at the same time, retain a compatibility with silicon technology. Although considerable progress has been achieved in the Ge QD growth technology, the inquiry into the optical properties of these structures is presently the subject of numerous theoretical and experimental works.

Recently, Raman scattering spectroscopy was successfully applied in studying the built-in mechanical stress and the mixing effect in Ge QDs using the frequencies of longitudinal optical (*LO*) Ge and Ge–Si phonons [4, 7, 8]. Transverse optical (*TO*) phonons are not observable in these experiments because, according to the Raman selection rules, they are inactive in the scattering geometry used. As in the case of planar Ge/Si SLs, Raman spectra of the Ge/Si SLs with QDs show lines due to the folded longitudinal acoustic (*LA*) phonons in the low-frequency region [8]. At the same time, the presence of QDs is expected to weaken or even remove the selection rules, because the wave-vector conservation law is no longer operative in such a structure, so that Raman scattering can involve phonons in the "forbidden" geometry. Nevertheless, this problem has not been studied in detail so far.

This work reports the results of studying the vibrational spectra of periodic structures with Ge QDs by resonant Raman scattering. It is demonstrated that these structures possess vibrational properties that are typical of both two- and zero- dimensional objects. The observation of QD-size-selective resonant Raman scattering from the *LO* phonons confined in Ge QDs is reported.

Samples for investigation were grown by molecular beam epitaxy in the Stranski–Krastanov growth regime on a (001)-oriented Si substrate coated with a 20-nm-thick buffer Si layer. The growth temperature for the Si layers was 800 and 500°C, respectively, before and after applying the Ge layer. The Ge layers with QDs were grown at a temperature of 300°C. The nominal thicknesses of the Ge and Si layers were 1.4 and 37 nm, respectively. The number of repetitive Ge and Si layer pairs was 10. The structural monitoring of the QD parameters was performed by high-resolution transmission electron microscopy of the structure cross section.

The Raman experiments were carried out with a Dilor XY800 spectrometer in the backscattering geometries $z(xx)z$ and $z(xy)z$ using the excitation lines of Ar^+, Kr^+, and HeNe lasers in the wavelength range 676.4–457.9 nm (1.83–2.71 eV). Raman spectra in the $y'(zz)y'$ and $y'(zx')y'$ geometries were recorded at a wavelength of 514.5 nm of the Ar^+ laser using a microscope focusing light into a spot of diameter 1 μm onto the sample cross section. The x, y, z, x', and y' indices correspond to

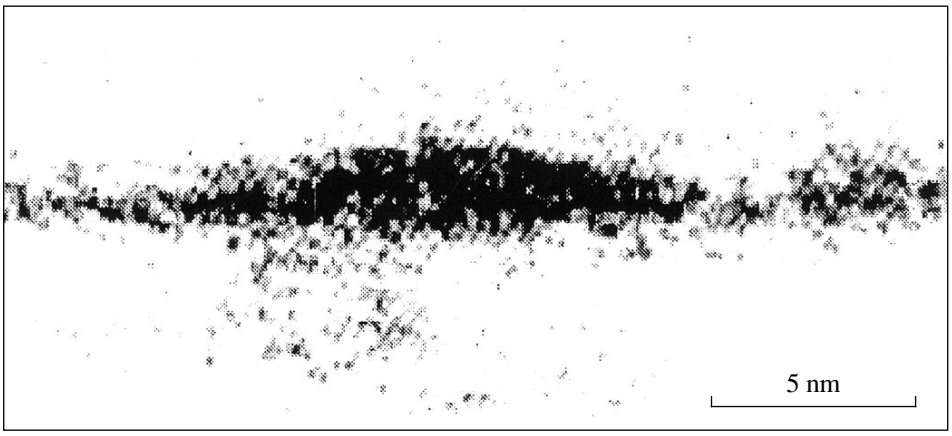

Fig. 1. High-resolution electron microscopy image of the sample. The dark area corresponds to the Ge layer with quantum dots.

the directions parallel to the [100], [010], [001], [1$\bar{1}$0], and [110] axes, respectively.

Figure 1 is a high-resolution electron microscopy image of the sample. The dark area corresponds to a layer with Ge QDs, and the light area corresponds to Si. One can see that the Ge QD is pyramid-shaped with a base on the order of 15 nm and a height of 2 nm. These parameters agree well with the tunneling microscopy data for samples prepared under similar growth conditions [9].

The Raman spectra recorded for different geometries are shown in Fig. 2. The low-frequency region of the $z(xx)z$ Raman spectra shows a line progression (up to the 15th order) due to folded *LA* phonons (FAPs) in the SL with Ge QDs. This fact is consistent with the Raman selection rules for the planar Ge/Si SLs [1]. The doublets of folded phonons are not resolved because of a small splitting (about 1 cm^{-1}) for the wave vector used in the experiment. The FAP lines overlap with a broad emission continuum with a maximum near 40 cm^{-1}. The FAP frequencies can be calculated using the dielectric continuum model [10], according to which the FAP dispersion in a periodic structure (e.g., Ge/Si) can be represented as

$$\cos(qd) = \cos\left(\frac{\omega d_1}{v_1}\right)\cos\left(\frac{\omega d_2}{v_2}\right) - \frac{k^2+1}{2k}\sin\left(\frac{\omega d_1}{v_1}\right)\sin\left(\frac{\omega d_2}{v_2}\right), \quad (1)$$

where $k = v_1\rho_1/v_2\rho_2$; $d = d_1 + d_2$; and d_1 and d_2, ρ_1 and ρ_2, and v_1 and v_2 are the thicknesses, the densities, and the sound velocities for the Ge and Si layers, respectively. The FAP dispersion calculated with parameters taken from [3] is shown in the inset in Fig. 2. The horizontal line in the inset corresponds to the wave vector used in the experiment. One can see from Fig. 2 that the agreement with the model is very good and there is no need to introduce any additional fitting parameters. The calculated period of the structure is 37.9 nm, in compliance with the value obtained from the high-resolution microscopy experiments.

The origin of the emission continuum observed in the Stokes and anti-Stokes regions of the $z(xx)z$ spectrum can be understood using the model of interaction between electrons (holes) confined in a quantum well and acoustic phonons. The charge-carrier confinement in a quantum well, whose width fluctuates because of the insular growth regime, breaks the translational symmetry and renders the whole acoustic branch Raman-active [11, 12]. The corresponding resonant Raman intensity is expressed as $q_z|M_{qz}|^2$, where q_z is the wave vector of a phonon propagating along the z axis and M_{qz} is the electron–phonon matrix element given by

$$M_{qz} = \int e^{iq_z z}|\varphi(z)|^2 dz. \quad (2)$$

Here, the wave function $\varphi(z)$ of the localized hole is taken in the form $\varphi(z) = a^{1/2}e^{-|z|/a}$, where a is the average thickness of the layer containing Ge QDs. This model was employed to calculate the Raman spectrum for a Ge layer thickness of 1.2 nm (Fig. 2, dotted line). The interaction between the neighboring layers with QDs was assumed to be negligible. One can see from Fig. 2 that this model adequately describes the experiment and that the Ge layer thickness is in agreement with its nominal value specified in the structure growth (1.4 nm). It is notable that the band maximum and shape strongly depend on the form of wave function. For this reason, the quantitative estimates should be done with the wave functions that are most appropriate to the geometry of the structures under study.

Let us now consider the optical phonon frequency range.

In the SLs containing Ge QDs, the optical phonons are split into two branches whose wave vectors are directed either along or perpendicular to the (001) direction: *LO* phonons and doubly degenerate *TO* phonons, respectively. According to the Raman selec-

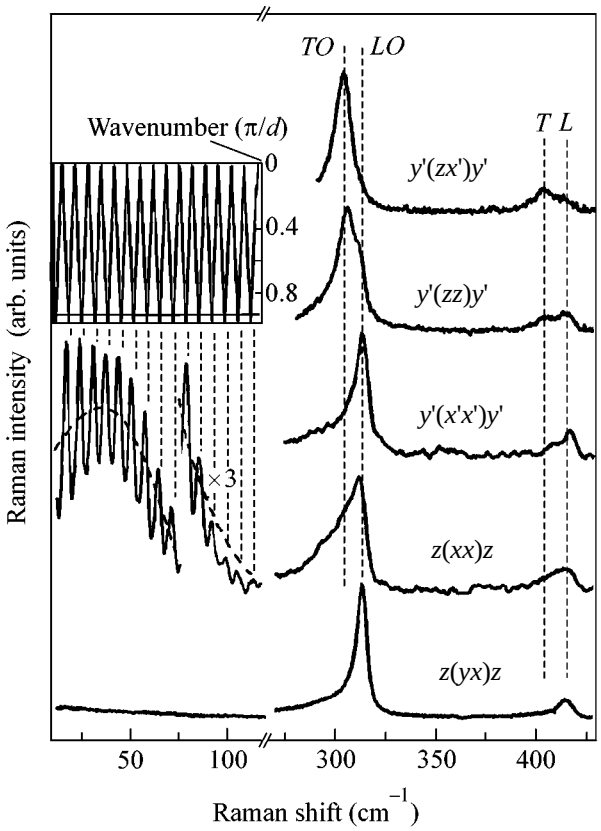

Fig. 2. Raman spectra recorded for the sample in different geometries. Inset: the calculated dispersion of acoustic phonons in the structure. The horizontal line corresponds to the wave vector used in the experiment.

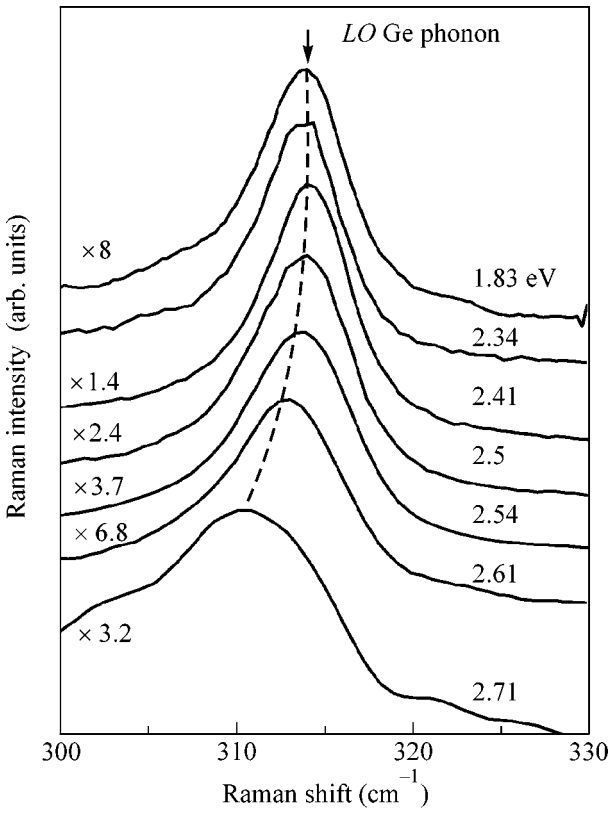

Fig. 3. The Raman frequency and intensity of *LO* phonons for different laser excitation energies.

tion rules, the *LO* phonons in the planar Ge/Si SLs grown on a (001) Si substrate should be observable in the Raman spectra for the $z(yx)z$ and $y'(x'x')y'$ scattering geometries, while the *TO* phonons are active in the $y'(zx')y'$ geometry [1]. The selection rules for Raman scattering in the SL containing Ge QDs are expected to weaken because of symmetry lowering. As a result, the "forbidden" vibrational modes become Raman-active in the structures with QDs. Indeed, as in the case of planar Ge/Si SLs, the experimental spectra of the structures with QDs (Fig. 2) show *LO* (315 cm^{-1}) and *TO* (308 cm^{-1}) phonons in the $z(yx)z$, $y'(x'x')y'$ and $y'(zx')y'$ geometries, respectively. Strong lines corresponding to the *LO* or to the *LO* and *TO* phonons are additionally observed in the forbidden $z(xx)z$ and $y'(zz)y'$ geometries, respectively, indicating the weakening of the Raman selection rules in the SL containing Ge QDs. Weak Raman lines observed at 405 and 417 cm^{-1} are caused by the transverse and longitudinal Ge–Si interface phonons labeled, respectively, *T* and *L* in Fig. 2.

A high-frequency shift of the *LO* and *TO* Ge phonons in QD relative to their bulk frequency (300 cm^{-1}) points to the presence of a strong mechanical stress in the QD. The calculation using the known dependence of phonon frequencies on mechanical stress [13] suggests that the Ge QDs are biaxially compressed to an extent of about 3.6% [8]. The *TO* and *LO* frequencies in this state are equal, respectively, to 310.6 and 315 cm^{-1}. A good coincidence with the experimental frequencies of optical phonons, as well as the small width of the corresponding lines (about 6 cm^{-1} at a half height), is evidence that the Ge QDs are unrelaxed and that there is no atomic mixing at the Ge–Si interface. A large experimental value of the *LO*–*TO* splitting is explained by the fact that the *LO* and *TO* phonons are characterized by different degrees of confinement in the Ge/Si structures. Indeed, only the *TO* Ge phonons are confined in the Ge/Si SL, because their frequencies do not overlap with the frequencies of optical and acoustic Si phonons. The longitudinal optical phonons in the Ge layers are quasi-localized because the Ge *LO* and Si *LA* bands overlap.

The observed *L*–*T* splitting fits the data in [2] and is explained by the fact that the atomic clusters contributing to the *L* and *T* vibrations have different character at the Ge/Si interface.

Whereas the acoustic phonons in the Ge/Si SL with QDs are satisfactorily described by the two-dimensional model, the behavior of optical phonons in the Raman spectra recorded at different laser excitation

energies can be explained only in terms of their confinement in the Ge QDs. Figure 3 displays the experimental Raman spectra in the *LO* region for different laser excitation energies in the $z(yx)z$ scattering geometry. The Raman intensity has a maximum at 2.34 eV, which is close to the resonance corresponding to the E_1 exciton in the Ge QD in [4]. The position of the *LO* phonons confined in the Ge QD shifts to lower frequencies (by 4–5 cm^{-1}) upon an increase in the excitation energy, which is evidence of the distribution of Ge QDs in size. The Raman intensity for small-sized QDs, in which the E_1 exciton lies at higher energy, increases when the excitation and E_1 energies are at resonance. The optical phonons confined in small-sized QDs are precisely the ones which undergo the largest low-frequency shift. Such a behavior is typical of the Ge-type materials with negative dispersion of optical phonons [14].

In summary, the vibrational spectrum of the Ge/Si superlattices containing Ge quantum dots have been studied in detail. It is found that these structures exhibit properties that are characteristic of both layered structures and quantum dots. The spectrum of acoustic phonons is adequately described by the dielectric continuum model. The low-frequency emission observed in the Raman spectra is caused by the contribution from the phonon states corresponding to the entire acoustic branch because of the violation of translational symmetry in the structures with QDs. As the laser excitation energy increases, the QD-size-selective resonant Raman spectra show a low-frequency shift for the optical phonons confined in the Ge QDs.

This work was supported in part by the Russian Foundation for Basic Research, project no. 00-02-18012.

REFERENCES

1. R. Schrorer, G. Abstreiter, H. Kibbel, *et al.*, Phys. Rev. B **50**, 18211 (1994).
2. S. de Gironcoli, E. Molinari, R. Schrorer, *et al.*, Phys. Rev. B **48**, 8959 (1993).
3. D. J. Lockwood, M. W. C. Dharma-wardana, J.-M. Baribeau, *et al.*, Phys. Rev. B **35**, 2243 (1987).
4. S. H. Kwok, P. Y. Yu, C. H. Tung, *et al.*, Phys. Rev. B **59**, 4980 (1999).
5. J. L. Liu, G. Jin, Y. S. Tang, *et al.*, Appl. Phys. Lett. **76**, 586 (2000).
6. O. P. Pchelyakov, Yu. B. Bolkhovityanov, A. V. Dvurechenskiĭ, *et al.*, Fiz. Tekh. Poluprovodn. (St. Petersburg) **34**, 1281 (2000) [Semiconductors **34**, 1229 (2000)].
7. A. B. Talochkin, V. A. Markov, S. P. Suprun, and A. I. Nikiforov, Pis'ma Zh. Éksp. Teor. Fiz. **64**, 203 (1996) [JETP Lett. **64**, 219 (1996)].
8. A. Milekhin, N. Stepina, A. Yakimov, *et al.*, Eur. Phys. J. B **16**, 355 (2000).
9. A. I. Yakimov, A. V. Dvurechenskii, Yu. Yu. Proskuryakov, *et al.*, Appl. Phys. Lett. **75**, 1413 (1999).
10. S. M. Rytov, Akust. Zh. **2**, 71 (1956) [Sov. Phys. Acoust. **2**, 68 (1956)].
11. T. Ruf, V. I. Belitsky, J. Spitzer, *et al.*, Phys. Rev. Lett. **71**, 3035 (1993).
12. A. Mlayah, A. Sayari, R. Grac, *et al.*, Phys. Rev. B **56**, 1486 (1997).
13. F. Cerdeira, C. J. Buchenauer, F. H. Pollak, *et al.*, Phys. Rev. B **5**, 580 (1972).
14. C. Trallero-Giner, A. Debernardi, M. Cardona, *et al.*, Phys. Rev. B **57**, 4664 (1998).

Translated by V. Sakun

JETP Letters, Vol. 73, No. 9, 2001, pp. 465–469. Translated from Pis'ma v Zhurnal Éksperimental'noĭ i Teoreticheskoĭ Fiziki, Vol. 73, No. 9, 2001, pp. 526–530.

Weak Localization Effects in a Quasi-One-Dimensional Electron System over Liquid Helium

Yu. Z. Kovdrya*, V. A. Nikolaenko, and S. P. Gladchenko

Verkin Physicotechnical Institute of Low Temperatures, National Academy of Sciences of Ukraine, Kharkov, 61164 Ukraine

** e-mail: kovdrya@ilt.kharkov.ua*

Received March 23, 2001

Magnetoresistance ρ_{xx} measurements are performed for a quasi-one-dimensional electron system over liquid helium in the gas-scattering region (the temperature range 1.3–2.0 K). The measurements show that, as the magnetic field increases, the magnetoresistance ρ_{xx} first decreases and then passes through a minimum and increases according to the law $\rho_{xx} \sim B^2$. It is suggested that the negative magnetoresistance observed in the experiment is caused by the weak localization effects. The results of the experiment are in qualitative agreement with the theoretical model describing the weak localization effects in a one-dimensional nondegenerate electron system.

PACS numbers: 73.20.Fz; 73.50.Jt

The localization effects in low-dimension disordered electron systems are the subject of many experimental and theoretical studies [1]. Two localization regimes are known: a weak localization and a strong one. A strong localization occurs when the electron free path l_0 for elastic scattering is small and the condition $kl_0 \sim 1$ is satisfied (k is the electron wave vector). The weak localization regime corresponds to the condition $kl_0 > 1$. A weak localization occurs as a result of the interference of the electron wave function in the presence of multiple electron scattering by impurities and other quasiparticles, which leads to noticeable corrections in the kinetic coefficients and, specifically, to a decrease in the conductivity. A weak localization is destroyed by the inelastic scattering and by the magnetic field. Earlier [2], it was shown that, in a magnetic field, the suppression of localization gives rise to an increase in the electron conductivity, and this negative magnetoresistance effect is one of the main indicators of weak localization.

Until recently, the attention of researchers was mainly concentrated on the weak localization effects in degenerate electron systems, i.e., in metals and semiconductors. However, the study of such effects in a nondegenerate electron gas is of major interest. Examples of nondegenerate systems of this kind are electrons localized on the surfaces of some cryogenic liquids or crystals—the surface electrons (SE). In nondegenerate systems, by varying the temperature it is possible to control the electron wave vector k_T and, hence, the quantity $k_T l_0$, which governs the localization processes. An SE layer allows one not only to vary the wave vector k_T in it, but also to vary the electron density n_0 and the electron free path l_0 in the same experiment, which can be important for studying fine effects of localization.

The weak localization effects that occur in a 2D electron system over solid hydrogen in the presence of the electron scattering from the surface roughness and from helium atoms were studied in [3, 4], and similar effects on a liquid helium surface with the scattering from vapor helium atoms were described in [5]. In these studies, the magnetoconductivity of the electron layer σ_{xx} was measured; it was found that the decrease in σ_{xx} due to the weak localization effects is within several percent.

The weak localization effects are most pronounced in quasi-one-dimensional (Q1D) and 1D electron systems. Up to now, the electron transport in Q1D and 1D systems in the weak localization conditions was studied in various types of nanostructures, such as metal films and semiconductors [6], carbon nanotubes [7], and other systems. In this paper, we describe the study of the weak localization effects in a Q1D electron system over liquid helium in the gas-scattering region.

To obtain a Q1D electron system in the experiment, we used a profiled insulating substrate covered with liquid helium [8, 9]. In this case, a system of parallel liquid channels with some curvature radius r is formed on the surface of the liquid. In the presence of a pressing electric field $E_\perp$, the electrons on the liquid surface pass

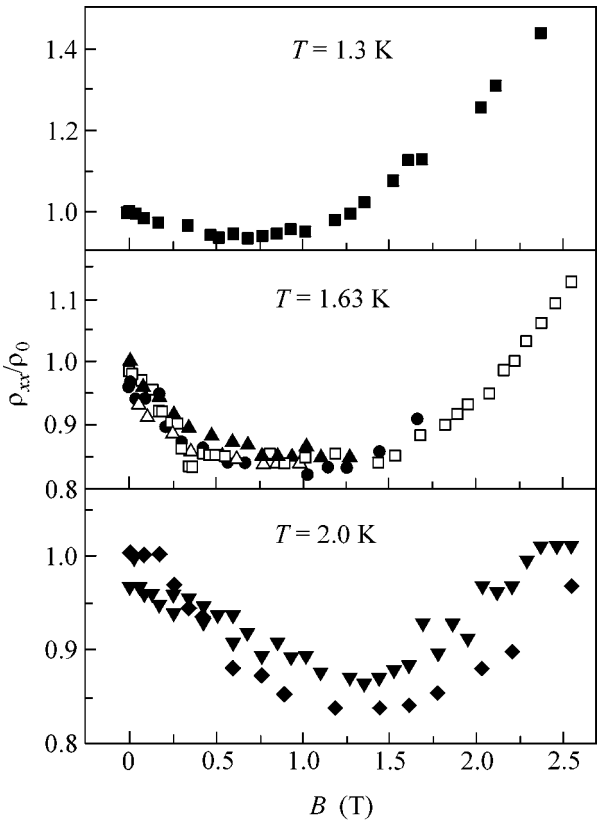

Fig. 1. Magnetic field dependence of the channel magnetoresistance divided by the resistance in zero magnetic field. Different signs represent the data obtained from different experiments.

to the bottoms of the liquid channels and form 1D or Q1D systems.

In a 1D system, the electron energy spectrum has the form [8]

$$\epsilon = \left(n + \frac{1}{2}\right)\hbar\omega_0 + \frac{\hbar^2 k_x^2}{2m}, \quad \omega_0 = \sqrt{\frac{eE_\perp}{mr}}, \qquad (1)$$

where $\hbar$ is Planck's constant, e and m are the electron charge and mass, k_x is the electron wave vector along the channel, and $n = 1, 2, 3, \ldots$.

Earlier [10, 11], in studying the electron mobility in such a system, we found that, when the substrate was contaminated by foreign substances or a charge accumulation occurred at its surface, a localization of electrons was observed at $T < 0.8$ K, which was accompanied by a considerable decrease in the effective mobility. However, the experiments were performed in zero magnetic field, and, therefore, it was difficult to separate the strong and weak localization processes. In the experiments described below, we measured the magnetoresistance in a Q1D electron system over liquid helium at relatively high temperatures, in the gas-scattering region where the free path l_0 was small and the localization effects were expected to be more pronounced. The experiments were performed within the temperature range 1.3–2.0 K in a pressing electric field of 450 V/cm, at a frequency of 100 kHz.

The experimental cell and the method of determining the conductivity of the channels are described in our previous publication [11]. The cell contained 150 channels with the mean curvature radius $r = 3.6 \times 10^{-3}$ cm and with a mean distance of 0.1 mm between them. The magnetic field was directed normally to the surface of the insulating substrate. In the experiments, we measured the real and imaginary parts of the cell conductance in the magnetic field B up to 2.5 T, which allowed us to determine the magnetoresistance of the channels.

The data obtained from our measurements are presented in Fig. 1, which shows the magnetoresistance $\rho_{xx}(B)$ divided by the resistance of the channels in zero magnetic field ρ_0 versus the magnetic field B. One can see that the quantity ρ_{xx}/ρ_0 first decreases with increasing magnetic field and then, passing through a minimum, increases approximately as $\rho_{xx} \sim B^2$. We note a good stability and reproducibility of the data for the temperatures 1.3 and 1.63 K. At $T = 2.0$ K, despite special precautions, some uncontrolled changes were observed in the electron density in the liquid channels, which explains the slight difference in the experimental data obtained in different experiments for $T = 2$ K.

We assume that the negative magnetoresistance observed in the experiment in small magnetic fields is caused by the weak localization of electrons in the Q1D electron system. As was mentioned above, the magnetic field suppresses the localization, which leads to a decrease in ρ_{xx}. With a further increase in magnetic field, ρ_{xx} begins to grow because of the decrease in the effective relaxation time due to the transition to the quantum transport regime.

The experimental data allow us to determine the value of the negative magnetoresistance $\Delta\rho_{xx}$, but it is necessary to know the dependence $\rho_{xx}(B)$ that should be observed in the absence of localization. An analysis of the literature data on σ_{xx} for SE over liquid helium [12] shows that the mobility μ of electrons over liquid helium does not depend on B up to the values $\mu B \sim 8$ at $T = 1.3$ K and up to $\mu B \sim 2$–3 at $T = 2.0$ K. We assume that, for the Q1D system under study, the mobility μ does not depend on B approximately up to the same values of μB. Extrapolating the dependence $\rho_{xx}(B)$ obtained from the experiment for magnetic fields $B >$ 1–1.5 T to the region of small magnetic fields where the mobility of the SE is independent of B, we can determine the value of ρ_0^0/ρ_0^l for $B = 0$ (ρ_0^0 and ρ_0^l represent the channel resistance in the absence and in the presence of localization, respectively) and, hence, the val-

ues of $\Delta\rho_{xx}$ and $\Delta\sigma_{xx}$. From the table, which shows the values of ρ_0^0/ρ_0^l, one can see that the effect of localization on the conductivity of the system reaches ~20%. This value far exceeds the corresponding value obtained for 2D nondegenerate systems [3–5].

In analyzing the results of our experiments, it is necessary to take into account that the system under study is not a 1D system in the strict sense. For the pressing electric field used in the experiment, the energy difference between two adjacent energy levels of the spectrum given by Eq. (1) is $\Delta\epsilon = 0.13$ K and, hence, at the temperature of the experiment, the electrons occupy not only the ground level, but also the higher levels with the numbers $n \approx kT/\Delta\epsilon$ (k is the Boltzmann constant). The table presents the lengths of the free paths l_0, as well as the mean "width" of a conducting channel at $B = 0$, which represents the localization length y_n of the electrons at the nth energy level. Unfortunately, the electron concentration in the channels n_0 could not be measured in the experiment, and, hence, we could not determine the electron mobility μ_0. However, taking into account that $\Delta\epsilon \ll kT$, we can assume that, in the system under study, the value of μ_0 is close to the corresponding value for a 2D electron layer. To calculate the values of n_0 and μ_0, we used the data on the mobility of electrons over liquid helium from [13]. According to the data presented in the table, at $T = 1.6$–2 K, we have $y_n > l_0$ and, at $T = 1.3$ K, the values of y_n and l_0 approximately coincide. Thus, one can see that, from the point of view of the kinetic characteristics, the system under study is close to a 2D system.

Using the data on ρ_0 obtained from the experiment and the data on μ_0 from the literature [13], we determined the decrease in conductivity due to the weak localization effects. The calculated values of this decrease per unit charge, $\Delta\sigma/n_0$, are presented in the table, and the dependence of this quantity on the concentration of helium atoms in the vapor, n_g, is shown in Fig. 2 by a solid line. One can see that $\Delta\sigma/n_0$ increases with decreasing n_g.

The characteristic length within which the coherence of electron states in the 2D system fails is determined by the expression

$$L_\varphi^{(2)} = \sqrt{\frac{1}{2} l_0 l_{in}}, \quad l_{in} = v_T \tau_\phi, \tag{2}$$

where l_{in} is the free path for inelastic processes, v_T is the thermal velocity of electrons, and τ_ϕ is the time within which the coherence of the wave function of the localized state is lost. Earlier [14], it was shown that, in the case of electron scattering by helium atoms, the following relations are valid:

$$\tau_\phi = (6\tau_0\tau_\lambda^2)^{1/3}, \quad \tau_\lambda = \left(\frac{M}{m}\right)^{1/2} \frac{\hbar}{2kT}, \tag{3}$$

where τ_0 is the relaxation time determined by the elastic processes and M is ^{4}He atomic mass. The table presents the values of $L_\varphi^{(2)}$ calculated by Eqs. (2) and (3). One can see that, at relatively high temperatures, we have $L_\varphi^{(2)} < y_n$ and, at $T = 1.3$ K, the opposite inequality is valid, $L_\varphi^{(2)} > y_n$. Thus, is seems reasonable to conclude that, from the point of view of localization effects, the system under study occupies an intermediate position between 1D and 2D systems.

The weak localization effects in the magnetoconductivity σ_{xx} of a nondegenerate electron gas were theoretically studied in [14]. The expression for σ_{xx} obtained in [14] is similar to that obtained in [2] and can be represented in the form

$$\sigma_{xx} = \frac{2e^2}{md} \int_{E_c}^{\infty} \frac{dE}{1 + \mu^2 B^2} \left(-\frac{\partial f}{\partial E}\right) \left[\nu_d E \tau_0 - \frac{md}{2\pi} J_d\right]. \tag{4}$$

Here, E is the energy, f is the distribution function, ν_d is the density of states, E_c is the limiting energy below which the localized electrons do not contribute to the conductivity, and d is the system dimension. The quantity J_d depends on the system dimension and, for a 2D electron gas, is determined by the expression

$$J_2 = \frac{\hbar}{4\pi} \left[\psi\left(\frac{1}{2} + \frac{\hbar m}{4eBE\tau_0^2}\right) - \psi\left(\frac{1}{2} + \frac{\hbar m}{4eBE\tau_0\tau_\phi}\right)\right], \tag{5}$$

where ψ is the digamma function.

At $B = 0$, Eq. (5) is reduced to the expression

$$J_2 = \frac{1}{4\pi} \ln \frac{\tau_\phi}{\tau_0},$$

and the decrease $\Delta\sigma_2$ that occurs in the conductivity of a 2D electron system in zero magnetic field due to the

Characteristics of the conducting channels

T, K	τ_0, 10^{-11} s	l_0, 10^{-5} cm	$k_T l_0$	y_n, 10^{-5} cm	$L_\varphi^{(2)}$, 10^{-5} cm	ρ_0^0/ρ_0^l	$\Delta\sigma/n_0$, 10^{-3} cm^3/s
1.3	10.3	3.6	10.9	2.64	4.64	0.83	4.44
1.63	2.51	0.97	3.29	2.96	2.0	0.75	1.59
2.0	0.91	0.42	1.58	3.3	1.06	0.86	0.35

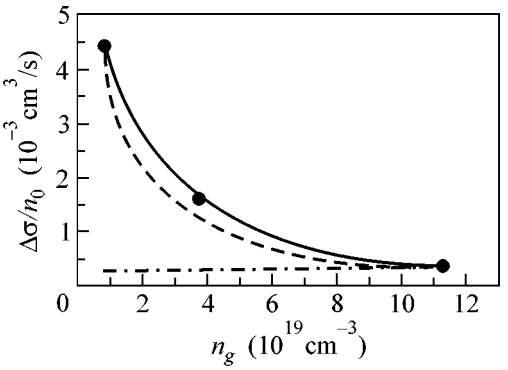

Fig. 2. Dependence of the quantity $\Delta\sigma/n_0$ on the concentration of helium atoms in the vapor. The solid line shows the experimental data, the dot-and-dash line corresponds to the calculation for a 2D system [14], and the dashed line shows the result of the calculation by Eq. (7) for $\tau_\phi/\tau_0 = 1.44$.

weak localization effects is determined by the expression [14]

$$\Delta\sigma_2 = -\frac{n_0 e^2 \hbar}{2\pi m k T}\ln\frac{\tau_\phi}{\tau_0}. \qquad (6)$$

In the derivation of Eq. (6), it was assumed that $E_c \approx 0$, which is valid in the case of electron scattering by helium atoms in the vapor when the concentration of helium atoms n_g is small. The quantity $\Delta\sigma_2/n_0$ calculated by Eqs. (3) and (6) is shown in Fig. 2 by the dot-and-dash line. From Fig. 2, one can see that, at $T = 2$ K, the experimental and calculated values approximately coincide, but, at lower temperatures, a considerable difference between experiment and calculation is observed. Thus, by analyzing the data in the framework of the theory developed for a 2D electron gas, we obtain no agreement with the experiment. It should be noted that the value obtained for τ_ϕ from Eq. (3) is greater than the experimental value reported in [5], and the use of the experimental value of τ_ϕ in the calculations decreases still further the calculated value of $\Delta\sigma_2/n_0$.

Using Eq. (4), we can obtain an expression that describes the decrease in the conductivity of a 1D nondegenerate electron gas, $\Delta\sigma_1$, due to the localization effects. We assume that, for $d = 1$, we have $J_1 = a(L_\varphi^{(1)} - l_0)$ [1], where $L_\varphi^{(1)}$ is the length within which the coherence of the wave function in the 1D system fails and a is a constant. The corresponding expression for $\Delta\sigma_1$ has the form

$$\Delta\sigma_1 = \left(\frac{2}{\pi}\right)^{1/2}\frac{n_0 e^2}{m}\tau_0\left(\left(\frac{\tau_\phi}{\tau_0}\right)^{1/2} - 1\right). \qquad (7)$$

In the derivation of Eq. (7), it was assumed that $a = 1$ and $L_\varphi = v_T(\tau_\phi\tau_0)^{1/2}$. Expression (7) adequately describes the experimental data if we take $\tau_\phi/\tau_0 = 1.44$ (the dashed line in Fig. 2). Such an agreement between the calculated and experimental data suggests that, at $T < 2$ K, in terms of the localization effects, the system under study is close to a 1D system.

It should be noted that the values of τ_ϕ/τ_0 obtained from the experiment are smaller than the corresponding value obtained in [5]. Presumably, in the Q1D system under consideration, additional mechanisms that destroy the coherence of the wave function come into play, for example, the mechanisms related to interlevel transitions.

It is well known that magnetic field destroys the localization when the magnetic length is $\lambda_H \approx l_0$. However, this condition is likely to be unsuitable for the system under study. According to [15], the energy spectrum of a 1D electron system changes in a magnetic field: in Eq. (1), the frequency ω_0 should be replaced by the frequency $\Omega = \sqrt{\omega_0^2 + \omega_c^2}$ (ω_c is the cyclotron frequency), and the electron mass should be replaced by the effective mass $m^* = m(\Omega/\omega_0)^2$. We note the following interesting feature: in contrast to a 2D electron system in which an electron is localized by the magnetic field within a length of the order of λ_H, in the system under study, in spectrum (1) in the magnetic field we have $k_x \neq 0$ [15], and, hence, an electron retains its ability to move along the channel. One can expect that, in this case, the localization effects caused by the interaction of electrons with scatterers are suppressed by much greater magnetic fields and the localization disappears when $\tau_\phi/\tau_0 \longrightarrow 1$ with increasing magnetic field. Unfortunately, so far the theory describing the weak localization effects in a Q1D electron system over liquid helium is lacking.

Thus, in our study, we observed the weak localization effects in a Q1D nondegenerate electron system over liquid helium. It was shown that the relative variation of the magnetoresistance due to the localization reaches ~20%, which far exceeds the corresponding value for a 2D nondegenerate electron gas. The calculated values of the magnetoconductivity decrease due to the weak localization effects in a 1D nondegenerate electron system are in qualitative agreement with the experimental results.

REFERENCES

1. P. A. Lee and T. V. Ramakrishnan, Rev. Mod. Phys. **57**, 287 (1985).
2. B. L. Altshuller, D. Khmelnitskii, A. L. Larkin, and P. A. Lee, Phys. Rev. B **22**, 5142 (1980).
3. P. W. Adams and M. A. Paalanen, Phys. Rev. Lett. **61**, 451 (1988).
4. P. W. Adams, Phys. Rev. Lett. **65**, 3333 (1990).
5. I. Karakurt, D. Herman, H. Mathur, and A. J. Dahm, Phys. Rev. Lett. **85**, 1072 (2000).
6. M. A. Kastner, R. F. Kwasnick, J. C. Licini, and D. J. Bishop, Phys. Rev. B **36**, 8015 (1987).

7. T. W. Ebbesen, H. J. Lezec, H. Hiura, *et al.*, Nature **382**, 54 (1996).
8. Yu. Z. Kovdrya and Yu. P. Monarkha, Fiz. Nizk. Temp. **12**, 1011 (1986) [Sov. J. Low Temp. Phys. **12**, 571 (1986)].
9. Yu. Z. Kovdrya and V. A. Nikolaenko, Fiz. Nizk. Temp. **18**, 1278 (1992) [Sov. J. Low Temp. Phys. **18**, 894 (1992)].
10. Yu. Z. Kovdrya, V. A. Nikolaenko, S. P. Gladchenko, and S. S. Sokolov, J. Low Temp. Phys. **113**, 1109 (1998).
11. S. P. Gladchenko, V. A. Nikolaenko, Yu. Z. Kovdrya, and S. S. Sokolov, Fiz. Nizk. Temp. **27**, 2 (2001) [Low Temp. Phys. **27**, 1 (2001)].
12. Yu. Z. Kovdrya, V. A. Nikolaenko, O. I. Kirichek, *et al.*, Low Temp. Phys. **91**, 371 (1993); A. O. Stone, P. Fozooni, M. J. Lea, and M. Abdul-Gader, J. Phys.: Condens. Matter **1**, 2743 (1989).
13. Y. Iye, J. Low Temp. Phys. **40**, 441 (1980).
14. M. J. Stephen, Phys. Rev. B **36**, 5663 (1987).
15. S. S. Sokolov and N. Studart, Phys. Rev. B **51**, 2640 (1995).

Translated by E. Golyamina

JETP Letters, Vol. 73, No. 9, 2001, pp. 470–473. Translated from Pis'ma v Zhurnal Éksperimental'noĭ i Teoreticheskoĭ Fiziki, Vol. 73, No. 9, 2001, pp. 531–535.

Observation of Anomalously Fast Diffusion in ^{3}He–^{4}He Solid Solutions near the BCC–HCP Transition

N. P. Mikhin*, A. V. Polev, and É. Ya. Rudavskiĭ

Verkin Physicotechnical Institute of Low Temperatures, National Academy of Sciences of Ukraine, Kharkov, 61103 Ukraine

** e-mail: mikhin@ilt.kharkov.ua*

Received March 23, 2001

The pulsed NMR technique was used to investigate diffusion on the BCC–HCP phase-equilibrium and melting curves of a dilute solution of ^{3}He in ^{4}He. The contributions from all coexisting phases were identified using the spin-echo method. It is established that, along with the contributions from the equilibrium BCC and HCP phases or from bulk liquid (in the melting curve measurements), there is an additional diffusional process that is characterized by an anomalously high diffusion coefficient. It is found that the latter is close to the diffusion coefficient in liquid helium, while the diffusion itself is spatially restricted. The observed effect may be caused by the formation of liquid droplets in the course of the BCC–HCP transition. © *2001 MAIK "Nauka/Interperiodica".*

PACS numbers: 67.80.Mg; 66.30.-h

Diffusional processes in solid ^{3}He–^{4}He solutions are highly diversified due to the quantum nature of the impurity and defect motions [1, 2] and to the coexistence of several crystallographic phases in crystal [2, 3]. The latter cause has not been adequately studied so far, while the experimental data obtained by different authors [3–5] do not allow one to draw unambiguous conclusions about the character of diffusional motion in the course of the BCC–HCP transition.

The BCC phase in pure ^{4}He and in a dilute solution of ^{3}He in ^{4}He exists only at relatively high temperatures (above 1 K), so that the diffusion in this phase mainly involves vacancies. NMR measurements have shown [3] that the spin-diffusion constant increases more than an order of magnitude upon the transition from HCP to BCC phase and reaches 10^{-7} cm^2/s. This result was confirmed in [4] for a broader range of solution concentrations. It should be noted that the diffusion coefficient measured in these works had a certain effective meaning; it described the diffusional transport in a mixture of phases and was assigned to that phase (BCC or HCP) which dominated in crystal at a given temperature.

A radically different temperature dependence was recently observed [5] for the diffusion coefficient at the melting point in the vicinity of the BCC–HCP transition. The authors of [5] measured the velocity of a thin superconducting wire moving in solid helium under the action of electromagnetic force. They assumed that the plastic flow accompanying this motion was caused by the self-diffusion of atoms via the exchange with vacancies and used this assumption to determine the relevant diffusion coefficient. The temperature dependence of this coefficient had a pronounced maximum near the BCC–HCP transition, with a peak value of 10^{-5} cm^2/s (for both pure ^{4}He and ^{3}He–^{4}He solutions) being close to the diffusion coefficient in liquid.

The inconsistency between the experimental results obtained in [3–5] motivated our detailed NMR studies of the diffusional motion in the vicinity of the BCC–HCP transition. Our concern was to use the merits of the spin-echo method and identify the diffusional processes for each of the phases coexisting in solution.

The experiments were carried out using a solution containing 1.05% of ^{3}He at temperatures of 1.3–1.8 K. In this temperature range, the melting curve has two triple points corresponding to the coexistence of the BCC, HCP, and liquid phases. In addition, measurements were made along the BCC–HCP phase equilibrium curve at pressures of 25.9–30.1 atm. A crystal for the investigation was grown by the capillary blocking method, and the diffusion coefficient was determined using the pulsed NMR technique at a frequency of 3.6 MHz.

A Stycast 1266 epoxy glue NMR tube was in close contact with a ^{4}He evacuation chamber. A capacitive pressure gauge was fitted to one of the tube's ends, and the temperature was measured by two resistance thermometers. Measurements were taken at each temperature point after 15-min holding to stabilize the temperature. The spin-diffusion coefficient was determined, for the most part, by the Carr–Purcell method [6] with a 90°–τ–180° sequence of probe pulses, where τ is the time delay between the pulses. If several equilibrium phases, each characterized by the individual diffusion coefficient D_i, are present in a sample, then the diffu-

sional decay of the spin-echo amplitude in a magnetic field with gradient G is given by

$$\frac{h}{h_0} = \sum_i \alpha_i \exp\left(-\frac{2}{3}\gamma^2 G^2 \tau^3 D_i\right). \quad (1)$$

Here, index i numbers the phases, α_i is the relative content of the ith phase in the sample, γ is the gyromagnetic ratio, h_0 is the maximal echo amplitude at $G = 0$, and h is the current value of echo amplitude at $G > 0$. In our experiment, the diffusional decay dominated over the decay caused by spin–lattice and spin–spin relaxation, because the condition $T_1^i > \tau > T_2^i$ was fulfilled. The parameters τ and G in Eq. (1) were chosen in such a way that the diffusional echo-signal decay could reliably be identified for each of the coexisting phases separately; for instance, it is convenient to use large τ times for the phases with small diffusion coefficient.

A typical dependence of the diffusional spin-echo decay on the magnetic-field gradient is presented in Fig. 1. Curve *1* (Fig. 1a) corresponds to a small τ value such that the exponentials in Eq. (1) are close to unity and $h/h_0 \approx 1$ for all G values. At the larger τ value (curve *2*), the diffusion coefficient can be determined from the slope of the h/h_0 vs. G curve with the use of Eq. (1). The result coincides well with the diffusion coefficient D_b measured for the BCC phase in [3, 7].

To identify the HCP phase, for which the diffusion coefficient is an order of magnitude smaller than for BCC, a more sensitive method of stimulated echo with three probe pulses 90°–τ_1–90°–($\tau_2 - \tau_1$)–90° [8] was used. In this case, the diffusional spin-echo decay has the form

$$\frac{h}{h_0} = \sum_i \alpha_i \exp\left(-\gamma^2 G^2 D_i \tau_1^2 \left(\tau_2 - \frac{\tau_1}{3}\right)\right). \quad (2)$$

An example of dependence (2) is demonstrated in Fig. 1a, where curve *3* approximates the experimental result by the sum of two exponentials corresponding to the diffusional processes in the BCC and HCP phases with diffusion coefficients D_b and D_h, respectively.

One can also see from Fig. 1a that, at small G, the h/h_0 ratio in curves *2* and *3* does not reach a maximum value close to curve *1*. This may signify the presence of one more phase with the diffusion coefficient much greater than D_b and D_h. To detect this diffusional process, we carried out systematic measurements by the Carr–Purcell method with short delay times τ. The results are presented in Fig. 1b, where each point corresponds to the average over several measurements.

It follows from Fig. 1 that, in addition to the diffusion in the BCC and HCP phases, a new diffusional process is clearly defined at small τ values in our experiment. As to curve *4* (Fig. 1b) for longer times τ, an analysis showed that it corresponds to the superposition of this new diffusional process and the diffusion in the BCC phase (the HCP signal decay is not detected at short times τ). The weight factor α_x for the additional fast diffusional process in Eqs. (1) and (2) is 7–9%.

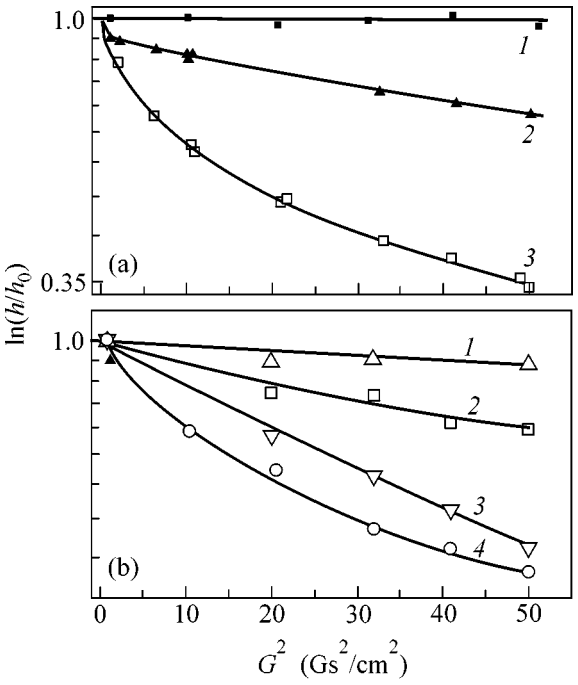

Fig. 1. Typical diffusional decay of spin-echo amplitude on the BCC–HCP phase equilibrium curve at $T = 1.42$ K. (a) Curves *1* and *2* are for the usual echo with $\tau = 0.3$ and 104 ms, respectively, and curve *3* is for the stimulated echo with $\tau_1 = 40$ ms and $\tau_2 = 910$ ms. (b) Usual echo at small τ values: (*1*) 2.2, (*2*) 10, (*3*) 25, and (*4*) 52 ms.

Unexpectedly, the coefficient D_x calculated for the new process using Eq. (1) proved to be dependent on τ. This implies that the additional diffusional process observed in our experiment is spatially restricted; i.e., atoms have time to encounter volume boundaries during the measurement. The restricted diffusion was examined earlier, both theoretically and experimentally, for various systems with different geometries of bounding cavities [9–12]. In this case, the true diffusion coefficient D_x corresponding to the bulk NMR measurements is related to the experimentally measured diffusion coefficient D_x' of the particles moving in a system of characteristic size a by expression

$$D_x' = \frac{a^4}{AD_x}\left(\frac{1}{\tau^2} - B\frac{a^2}{\tau^3 D_x}\right), \quad (3)$$

where the parameters A and B depend on the geometry of the system. In particular, $A = 175/3$ and $B = 581/1680$ for the spherical cavity of radius a [11]. Note that Eq. (3) is valid if $2\tau > a^2/\pi D_x$, i.e., if the diffusing particle suffers many collisions with barriers (droplet

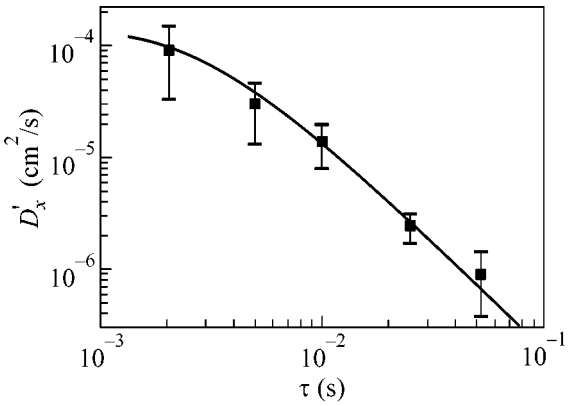

Fig. 2. The measured effective diffusion coefficient for the new diffusional process vs. the time delay between the NMR pulses at $T = 1.6$ K and $P = 29.9$ atm. Solid line is a fit to Eq. (3) with $D_x = (4 \pm 2) \times 10^{-4}$ cm^2/s and $a = (2 \pm 0.5) \times 10^{-3}$ cm.

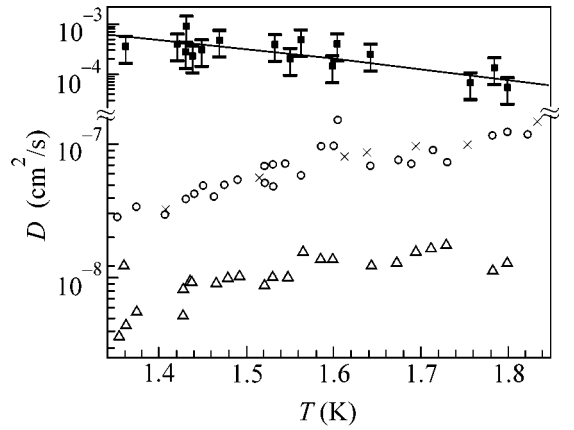

Fig. 3. Temperature dependences of the diffusion coefficients for each of the coexisting phases of a solid solution near the HCP–BCC phase equilibrium curve: (△) HCP phase; (○) BCC phase (this work); (×) BCC phase ([7]); and (■) the additional diffusional process. Solid line corresponds to the temperature dependence of the spin-diffusion coefficient in a bulk liquid at a pressure of 19 atm, as recalculated to the 1% ^{3}He concentration [13].

boundary) during time 2τ, so that its motion, though being three-dimensional, becomes spatially restricted.

Figure 2 shows the typical dependence of the measured D_x' value on the time delay between the pulses. These data were approximated by expression (3), which is valid for spherical geometry, and the result of the fitting procedure is shown by the solid curve. Note that the result changes only slightly if cylindrical [11, 12] or plane-parallel [9, 10] geometry is taken instead of a sphere.

The values of the true diffusion coefficient D_x corresponding to the new diffusional process are given in Fig. 3 together with the data for the BCC and HCP phases (D_b, D_h). The data obtained earlier in [7] for the BCC phase are in good agreement with our results and also presented in Fig. 3.

In spite of a noticeable scatter of the experimental data, it is clearly seen in Fig. 3 that the D_x value is several orders of magnitude greater than D_b and D_h and virtually coincides with the diffusion coefficient D_l in liquid [13] (solid line in Fig. 3). This fact and the restricted character of the diffusion allow the assumption to be drawn that D_x accounts for the diffusion in liquid droplets (of size a) that are formed in the course of the BCC–HCP transition. This assumption is also supported by the fact that the observed temperature dependence of D_x correlates well with the temperature dependence of D_l.

Inasmuch as the pressure in the sample far exceeds the pressure of liquid crystallization, the above-mentioned droplets can arise in the course of the BCC–HCP phase transition only if a local region of reduced pressure appears in crystal as a result of the defect formation due to lattice strains at the BCC–HCP interface and to the difference in molar volumes of the BCC and HCP phases. Liquid helium "pockets" arising near the rough tube walls or because of poor wetting of solid substrates with crystal helium [14] may be another possible source of the liquid.

The aforementioned results were obtained in the measurements along the BCC–HCP phase equilibrium curve. Similar studies were carried out for the melting curve in the temperature range covering two triple points and the two-phase liquid–BCC coexistence region. In the latter case, only two diffusional processes, corresponding to the BCC crystal and to the volume liquid, were detected in the spin-echo experiments. However, the experimental data obtained in the region near both triple points allowed the identification, apart from the expected three diffusional processes corresponding to the volume liquid, BCC phase, and HCP phase, of an additional restricted-diffusion process with the diffusion coefficient close to D_l. This process is quite similar to the diffusional motion of atoms with diffusion coefficient D_x, as discussed above for the higher pressure range (Fig. 3). The temperature dependence obtained in this case for the diffusion coefficients of the coexisting phases correlates with the results obtained in [3] and does not with the anomalous behavior observed for the diffusion coefficient in [5].

Note that the appearance of a liquid in the BCC–HCP transition was previously observed in the acoustic studies of the solid ^{4}He–HeII interface mobility [15]. Recent direct optical observations have shown [16] that the formation of the equilibrium HCP phase in the vicinity of the triple point on the ^{4}He melting curve is preceded by the appearance of a metastable BCC phase, whose formation requires a lower potential barrier than for the HCP phase. The subsequent formation of the HCP phase proceeded through the melting of the BCC phase.

There is also experimental evidence [17–20] for the ease of formation of liquid droplets in solid helium. It seems likely that the inner crystal surfaces containing defects are the most suitable places for the nucleation of liquid droplets. In the case of the BCC–HCP transition, the lattice distortions in the crystal boundaries are particularly strong and, thus, favor the formation of a liquid.

It is noteworthy that the fast diffusion may also be caused by a mechanism associated with the formation of linear defects (dislocations) or two-dimensional defects (grain boundaries) during the BCC–HCP transition. Since the activation energy for diffusion over the grain boundaries or along the dislocations is in many cases appreciably lower than the activation energy for bulk diffusion [21], the corresponding diffusion coefficients may differ from one another by several orders of magnitude.

In this case, a restricted low-dimensional diffusion should be observed instead of the three-dimensional restricted diffusion in droplets. Accordingly, the exponential form of the diffusional spin-echo decay, typical of the bulk diffusion [Eqs. (1), (2)], should be replaced by a nonexponential function [22, 23].

An analysis showed that our experimental results cannot be described by a one-dimensional model. As to the choice between two-dimensional and three-dimensional diffusion, the accuracy of our measurements is insufficiently high for an unambiguous conclusion to be drawn; to do this, measurement with larger magnetic-field gradients are necessary. However, the large relative contribution (α_x = 7–9%) from the fast diffusion to the echo-signal amplitude argues against the two-dimensional model. This situation can occur only if small-sized, on the order of 10^{-6}–10^{-5} cm, crystallites form during the BCC–HCP transition. This size is several orders of magnitude smaller than the value of a obtained in our experiment. Therefore, our experimental findings suggest that the fast diffusion observed in the solid solutions of ^{3}He in ^{4}He near the BCC–HCP transition is associated with the formation of liquid droplets in a crystal.

We thank V.N. Grigor'ev for the remark that initiated these experiments and for helpful discussions. We are also grateful to J. Saunders and B. Cowan (Royal Holloway University of London) for kindly providing us with a pulsed NMR spectrometer and to E.V. Syrnikov for assistance in the experiment.

REFERENCES

1. A. F. Andreev and I. M. Lifshits, Zh. Éksp. Teor. Fiz. **56**, 2056 (1969) [Sov. Phys. JETP **29**, 1107 (1969)].
2. V. N. Grigor'ev, Fiz. Nizk. Temp. **23**, 5 (1997) [Low Temp. Phys. **23**, 1 (1997)].
3. V. N. Grigor'ev, B. N. Esel'son, and V. A. Mikheev, Zh. Éksp. Teor. Fiz. **64**, 608 (1973) [Sov. Phys. JETP **37**, 309 (1973)].
4. A. R. Allen, M. G. Richards, and J. Schratter, J. Low Temp. Phys. **47**, 289 (1982).
5. I. Berent and E. Polturak, J. Low Temp. Phys. **112**, 337 (1998).
6. H. Y. Carr and E. M. Purcell, Phys. Rev. **94**, 630 (1954).
7. V. N. Grigor'ev, B. N. Esel'son, and V. A. Mikheev, Zh. Éksp. Teor. Fiz. **66**, 321 (1974) [Sov. Phys. JETP **39**, 153 (1974)].
8. E. L. Hann, Phys. Rev. **80**, 580 (1950).
9. B. Robertson, Phys. Rev. **151**, 273 (1966).
10. R. C. Wayne and R. M. Cotts, Phys. Rev. **151**, 264 (1966).
11. C. J. Neuman, J. Chem. Phys. **60**, 4503 (1974).
12. D. E. Lauffer, Phys. Rev. A **9**, 2792 (1974).
13. R. L. Garvin and H. A. Reich, Phys. Rev. **115**, 1478 (1959).
14. Yu. A. Kosevich and S. V. Svatko, Fiz. Nizk. Temp. **9**, 193 (1983) [Sov. J. Low Temp. Phys. **9**, 99 (1983)].
15. V. N. Grigor'ev, N. E. Dyumin, and S. V. Svatko, Fiz. Nizk. Temp. **15**, 253 (1989) [Sov. J. Low Temp. Phys. **15**, 142 (1989)].
16. T. A. Johnson and C. Elbaum, J. Low Temp. Phys. **107**, 317 (1997).
17. K. O. Keshishev, A. Ya. Parshin, and A. Babkin, Zh. Éksp. Teor. Fiz. **80**, 716 (1981) [Sov. Phys. JETP **53**, 362 (1981)].
18. E. Polturak, I. Schuster, I. Berent, *et al.*, J. Low Temp. Phys. **101**, 177 (1995).
19. T. Markovitz, E. Polturak, and S. G. Lipson, Phys. Rev. B **58**, 5493 (1998).
20. Y. Okuda, S. Yamazuki, T. Yoshida, *et al.*, J. Low Temp. Phys. **113**, 775 (1998).
21. H. G. van Bueren, *Imperfections in Crystal* (North-Holland, Amsterdam, 1960; Inostrannaya Literatura, Moscow, 1962).
22. V. A. Mikheev and V. A. Slyusarev, Fiz. Nizk. Temp. **7**, 379 (1981) [Sov. J. Low Temp. Phys. **7**, 186 (1981)].
23. K. N. Kantor and L. A. Maksimov, Fiz. Nizk. Temp. **15**, 123 (1989) [Sov. J. Low Temp. Phys. **15**, 69 (1989)].

Translated by V. Sakun

JETP Letters, Vol. 73, No. 9, 2001, pp. 474–478. Translated from Pis'ma v Zhurnal Éksperimental'noĭ i Teoreticheskoĭ Fiziki, Vol. 73, No. 9, 2001, pp. 536–541.

Boron Implanted in Silicon: Segregation at Angular Configurations of the Silicon/Silicon Dioxide Oxidation Boundary

G. A. Tarnavsky[1], S. I. Shpak[1,*], and M. S. Obrecht[2,]**

[1] *Institute of Theoretical and Applied Mechanics, Siberian Division, Russian Academy of Sciences, Novosibirsk, 630090 Russia*

** e-mail: shpak@itam.nsc.ru*

[2] *Siborg System Inc., University of Waterloo, N2L3G1 Ontario, Canada*

*** e-mail: obrecht@siborg.ca*

Received March 23, 2001

Based on computer simulation of the physicochemical segregation processes involving dopants implanted into a host material (silicon), the details of boron injection were investigated for four types of angular configurations (direct and inverse kinks and cavities of the "trench" and "square" types) of the "silicon/silicon dioxide" oxidation boundary. A complicated picture of the B distribution inside the Si and SiO_2 regions and at the SiO_2/Si front was obtained and analyzed in general terms. © *2001 MAIK "Nauka/Interperiodica".*

PACS numbers: 68.35.Dv; 66.30.Jt

Modeling of the segregation process, i.e., physicochemical process of interaction between the oxidation wave (boundary) in a host material and the impurities of various chemical elements implanted into the host (substrate), is an important part of computer simulation of a complex problem associated with the fabrication of materials possessing predetermined semiconductor properties. The physical mechanism of segregation is based on the appearance, at the oxide/material boundary, of an electromagnetic field with strongly localized high-intensity short-lived potential that either expels (ejection-type segregation) or draws in (injection-type segregation) the doping chemical elements, depending on the configuration of their outer electronic shells. This work is devoted to studying the segregation of boron B-5 ($2s^2 2p^1$) implanted into silicon Si-14 ($3s^2 3p^2$). The configurations of electronic shells whose structures cause strong injection (drawing-in) of B from the Si material to the SiO_2 oxide at the SiO_2/Si wave are given in parentheses. The quantum-mechanical approach to solving this problem encounters considerable difficulties and cannot be implemented in a practical manner even with modern computer techniques. This causes the necessity of developing approximate segregation models. The computational cycle presented below employs the theoretical model and the computer algorithm for its implementation that were described in detail in [1], where the interrelation between this model and other segregation models was also discussed. The dopant segregation at the SiO_2/Si boundary is induced by thermochemical silicon oxidation and characterized by the segregation coefficient $m = C_+/C_-$, where C_+ and C_- are the impurity concentrations at the material/oxide boundary on the material and oxide sides, respectively. The thermodynamic estimates of this coefficient are accurate to one to two orders of magnitude. The direct experimental measurements made by different authors (see, e.g., [2–7]) indicate that this coefficient strongly varies depending on the oxidation conditions. In the computations presented below, the value $m = 0.3$ taken for B corresponds to the coefficient that is most commonly accepted for the thermodynamically equilibrium segregation (note that m may change significantly under nonequilibrium conditions [8]). Generally, numerical simulation of the semiconductor properties of doped silicon is mainly carried out by taking into account simultaneously several processes: implantation of impurities into a host material, its oxidation, segregation of impurities at the boundary of oxidation wave, and impurity diffusion in oxide and material. In the simplest cases, the computational results for such a completely formulated problem correlate with the experimental data with a more or less reasonable accuracy. In the more complicated cases (in particular, with essentially curvilinear oxidation boundaries), the interpretation of the results may be rather difficult, because it then becomes unclear which of the above-mentioned processes is modeled with a good accuracy and which is not. For example, a rather inaccurate calculation of the oscillatory segregation process may be masked by the diffusion computations because the latter have a pronounced smoothing-out effect. In our opinion, this renders the development of numerical simulation separately for different physical

processes quite necessary because it would allow adequate comparison with the experimental data of type [9, 10] when designing new methods of fabricating semiconductor materials.

Statement of the problem. The segregation of Group IIIA element (boron) implanted into silicon with an oxide wave moving inside it is considered. The SiO_2/Si boundaries have rectangular bends comprising four types of oxide configuration in a material: "direct and inverse kinks" and cavities of the "trench" and "square" types (Figs. 1a, 2a, 3a, 4a). The initial impurity concentration in Si was taken to be uniform, and the diffusion of impurity is disregarded. The dimensional parameters of the problem were as follows: the length and width of the Si substrate (the computational X–Y region) ranged from 0.5 to 1.5 μm; the minimum initial and the maximum final thicknesses of oxide were 0.001 and 0.8 μm, respectively; the oxidation rate was 0.005 μm/min at a free O_2 pressure of 10^5 Pa and an oxidation temperature of 1100°C; and the initial impurity concentration was varied from 10^{16} to 10^{22} cm^{-3}. In the computations, linear dimensions were normalized to 1 μm, time to 1 min, and concentrations to 10^{20} cm^{-3}. This allowed the recalculation of the results from the dimensionless to the dimensional form when needed. As a rule, numerical simulation of segregation is performed for the smooth oxidation wave boundaries (continuous first and second derivatives with respect to coordinates) of the "bird beak" type (see, e.g., [7]). This also brings about rather smooth impurity distributions ahead and behind the segregation front and in the tangential direction. However, in practice, when developing the techniques of fabrication of semiconductor materials with predetermined properties, it is necessary to form depressions of various rectangular configurations in a host substrate, which also results in the right-angle configurations of the oxide/material boundaries (actually, the regions with a very sharp change in curvature and, formally, the regions where the first derivative has a discontinuity). On the one hand, the calculation of segregation at the boundaries of such a configuration is a good test of the computational methods and their computer implementation, while, on the other, the resulting numerical data are of considerable physical interest and important practical use. Figure 1 presents some numerical results for the impurity segregation dynamics at the SiO_2/Si oxidation wave shaped like a direct kink. Figure 1a shows the topology of the problem: the hatched area is occupied by SiO_2 whose boundary moves uniformly from the origin of coordinates through the SiO_2 material, draws in the B impurities from Si, and shifts them behind the front (into the SiO_2 oxide). Figure 1b shows the impurity distribution $C(x, y)$ in the substrate (the far corner in Fig. 1b corresponds to the origin of coordinates in Fig. 1a); the impurity concentration appears as strongly localized groovelike fronts at the oxide boundary. Behind this front, the trajectory of the corner on a flat $C(x, y)$ field

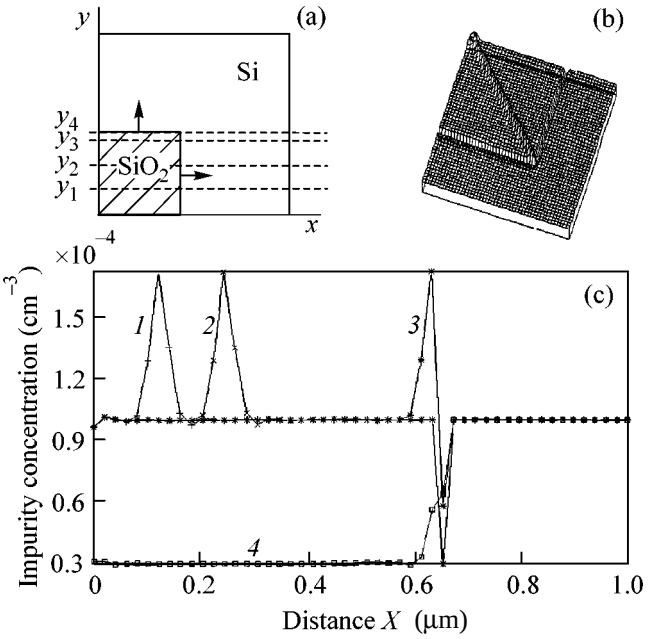

Fig. 1. Segregation at the direct kink. (a) General topology of the problem; (b) isometric projection of the $C(x, y)$ concentration in the computational region; (c) $C(x, y_i)$ distributions for y_i = 0.13, 0.25, 0.62, and 0.64 (curves *1–4*).

in SiO_2 is well-defined as a "ridge" with a maximum in the center and a sharp drop to its right and left. [Note that this impurity configuration serves as an initial condition for the algorithm of calculating diffusion in this temporary layer, so that one can expect high diffusion flows not only across the segregation front but also along it. This places special requirements upon the quality of diffusion calculation in the indicated subarea and upon the methods of its implementation and necessitates the use of a dense computational grid in two coordinate directions in the regions with large $C(x, y)$ gradients. Considering the boundary dynamics, this may become an overly stringent and hard-to-realize requirement when organizing the solution of a complete problem involving the implantation, oxidation, segregation, and diffusion processes.] Figure 1c allows one to carry out exact quantitative analysis. It demonstrates the one-dimensional impurity distributions $C(x, y_i)$ at time t = 40 for certain fixed values y_1 = 0.139, y_2 = 0.25, y_3 = 0.62, and y_4 = 0.64 indicated by the dashed lines in Fig. 1a. Lines *1–3* pass through the regions of SiO_2 oxide ($x < 0.62$) and Si ($x > 0.66$) and intersect the front of the SiO_2/Si oxidation wave at the point x = 0.64. Accordingly, curves *1–3* corresponding to the $C(x, y_1)$, $C(x, y_2)$, and $C(x, y_3)$ distributions are of the same type and have flat "plateaus" at a level of 0.96×10^{-4}, above which the "peaks" with a height of about 1.73×10^{-4} arise at the intersection points of the y_i = const lines and the SiO_2/Si-corner trajectory. In the second region, where the SiO_2/Si front is intersected, a

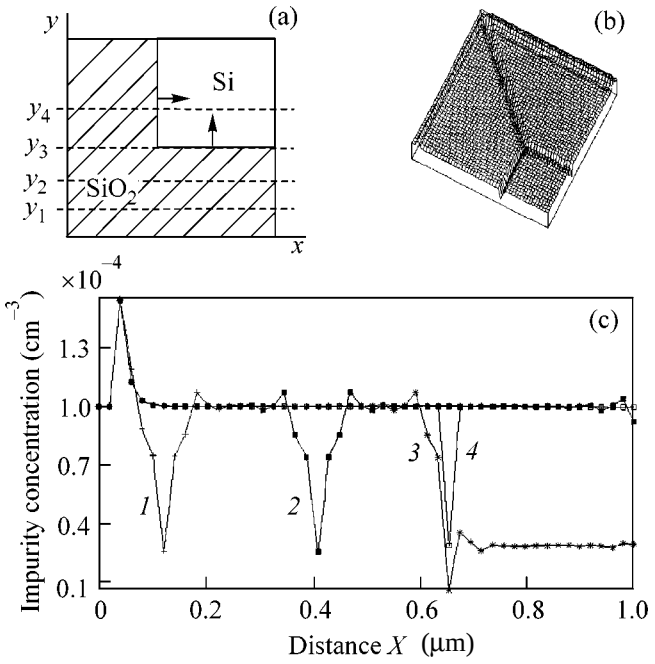

Fig. 2. Segregation at the inverse kink. (a) General topology of the problem; (b) isometric projection of the $C(x, y)$ concentration in the computational region; (c) $C(x, y_i)$ distributions for $y_i = 0.12$, 0.41, 0.64, and 0.82 (curves *1–4*).

"dip" arises with a minimum of 0.3×10^{-4} (segregation region). In the third region (Si), the concentrations are equal to their background value of 10^{-4}. Line *4* goes along the SiO_2/Si front ($x < 0.62$) and in Si ($x > 0.66$). Accordingly, curve *4* corresponding to the $C(x, y_4)$ distribution has three segments: two flat plateaus, one at a level of 0.3×10^{-4} along the SiO_2/Si front and the second at 10^{-4} in Si, and the intermediate segment between them at the SiO_2/Si corner ($0.62 < x < 0.66$).

The segregation at the inverse kink (Fig. 2a) is the inverse process of segregation at the direct kink, in the sense that, although the SiO_2/Si oxidation wave extracts the boron impurity from Si to SiO_2 oxide, the distribution of the extracted mass in SiO_2 is quite different; the ridge effect is replaced by the "gully" effect, for which a subarea (in our case a straight line) arises on the SiO_2/Si-corner trajectory, where the minima appear on the background of uniform $C(x, y)$ values in the remaining SiO_2 region. Three dips are clearly seen in Fig. 2b: two at the SiO_2/Si front and one on the corner trajectory. Figure 2c can be used to perform exact quantitative analysis. It illustrates the one-dimensional boron distributions $C(x, y_i)$ at time $t = 40$ for certain fixed values $y_1 = 0.12$, $y_2 = 0.41$, $y_3 = 0.64$, and $y_4 = 0.82$ indicated by the dashed lines in Fig. 2a. Lines *1* and *2* pass through the SiO_2 oxide, line *3* passes through the SiO_2 region ($x < 0.64$) and along the SiO_2/Si front ($x > 0.64$), and line *4* passes through SiO_2 ($x < 0.64$) and Si ($x > 0.64$) and intersects the SiO_2/Si front at the point $x = 0.64$. Curves *1* and *2* (Fig. 2c) corresponding to the $C(x, y_1)$ and $C(x, y_2)$ distributions illustrate, in fact, the whole history of the SiO_2/Si-boundary motion "upward rightwards" (Fig. 2a); in the vicinity of the intersection point of the $y_i = \text{const}$ line and the corner trajectory ($x = 0.12$ and $x = 0.41$ points for curves *1* and *2*, respectively), the dips with identical shapes and a minimum value of 0.3×10^{-4} arise in $C(x, y_2)$ on the background of a flat plateau of 10^{-4} values in the gully subarea (note for completeness that the peaks with maxima at 1.6×10^{-4} at $x = 0.04$ are caused by the initial configuration and are irrelevant to the further analysis). The $C(x, y_3)$ distribution in SiO_2 shows a plateau at 10^{-4} and is of the same type, but the flat plateau in the region $x > 0.7$ (SiO_2/Si front) is situated at a level of 0.3×10^{-4}. There is an intermediate region between these plateaus ($0.6 < x < 0.7$), with a deep minimum of 0.095×10^{-4} at $x = 0.64$, where the SiO_2/Si corner is located, and, hence, the segregation is more pronounced because of the injection of B through the fronts simultaneously in two directions (x and y). Curve *4* has the standard shape: a plateau at 10^{-4} in SiO_2 ($x < 0.62$) and Si ($x > 0.66$) and the intermediate region ($0.62 < x < 0.66$) at the SiO_2/Si front with a symmetric "triangular" 0.3×10^{-4} dip.

Segregation in a cavity of the trench type. The configuration of the oxidation boundary of this type (Fig. 3a) resembles the one used in semiconductor materials design. The impurity segregation in such a system has the same traits as in the above-mentioned segregation processes occurring at the direct and inverse kinks. Figure 3b provides a rather adequate qualitative illustration of the structures arising at the SiO_2/Si front as a result of the injection of boron impurity from the material to oxide. Among these are the direct dips in the $C(x, y)$ curves at the boundaries of the oxidation wave and the ridges on the trajectory of the convex corners of the front. A quantitative analysis of the $C(x, y)$ distribution in the computational region can be carried out using the graphs of one-dimensional sections $C(x, y)$ along the $y = \text{const}$ (0.5, 0.62, 0.75, and 0.86) and $x = \text{const}$ (0.5, 0.67, and 0.8) rays (Figs. 3c and 3d, respectively). Curve *1* corresponding to $C(x, y_1)$ in Fig. 3c passes along the SiO_2/Si front (Fig. 3a), with its central portion ($0.2 < x < 0.8$) lying at the front and its left ($x < 0.2$) and right ($x > 0.8$) portions lying in the Si region [note that for the chosen instant of time $t = 40$ the coordinates of the two convex corners of the boundary are (0.2, 0.5) and (0.8, 0.5), respectively]. The curve has a piecewise-constant shape with a central plateau of 0.3×10^{-4} in the [0.22, 0.78] interval and plateaus corresponding to the background concentrations of 10^{-4} in the [0, 0.2] and [0.8, 1] intervals. Curve *2* in Fig. 3c is the $C(x, y_2)$ distribution along the $y_2 = 0.62$ ray that passes through the Si ($x < 0.2$ and $x > 0.8$) and SiO_2 ($0.2 < x < 0.8$) regions and twice intersects the segrega-

tion front at $x = 0.2$ and 0.8. In the Si region, the concentration is equal to its background value of 10^{-4}; at the fronts, the concentration curve shows 0.3×10^{-4} dips; and in the SiO_2 region, the concentration increases to 10^{-4}. Peaks with a maximum of about 1.7×10^{-4} corresponding to the intersection of the $y = y_2$ ray and the SiO_2/Si-front corner trajectories are seen at $x = 0.35$ and 0.65 in the SiO_2 region. Curves *3* and *4* correspond, respectively, to $C(x, y_3)$ and $C(x, y_4)$ for the rays lying in Si (at $x < 0.2$ and $x > 0.8$) and SiO_2 (at $0.2 < x < 0.42$ and $0.58 < x < 0.8$) and intersecting the front at $x = 0.2$ and 0.8. In the range $x \in [0.42, 0.58]$, the y_3 ray goes along the initial SiO_2/Si front, while the y_4 ray twice intersects the initial front of the SiO_2 oxide at $x = 0.42$ and 0.58 and passes through it. Accordingly, the peaks in curves *3* and *4* are shifted to these coordinates, and the concentration reaches its absolute maximum of 2×10^{-4} at the corners of the initial SiO_2/Si boundary. The $C(x, y)$ distributions along the x = const rays, i.e., in another coordinate direction, are given in Fig. 3d. Curve *1* corresponds to the $C(x_1, y)$ values at the symmetry line $x_1 = 0.5$. This ray (Fig. 3a) passes through the Si material ($y < 0.5$), intersects the SiO_2/Si front at the point $y = 0.5$, and further goes through the two subareas of the SiO_2 oxide ($y > 0.5$), namely, through the region where the oxidation happened while solving the problem ($0.5 < y < 0.75$) and through the initial oxidation region ($y > 0.75$). The concentration changes along this ray in the following way. $C(x_1, y)$ is equal to its background value of 10^{-4} in the Si region; at the front, it decreases peakwise to a value of 0.3×10^{-4}; it reaches a plateau value of 10^{-4} in the first SiO_2 subarea, where a 1.5×10^{-4} peak occurs at $y = 0.75$; and then $C(x_1, y)$ regains its background value of 10^{-4} in the initial oxide subarea. Curve *2* in Fig. 3d corresponds to the $C(x_2, y)$ concentration on the $x_2 = 0.67$ ray that passes through the Si ($y < 0.5$) and SiO_2 ($y > 0.5$) regions and intersects the SiO_2/Si front at $y = 0.5$. In the Si region, the concentration is equal to its background value of 10^{-4}; at the front, it drops to 0.33×10^{-4}; and finally it regains its plateau value of 10^{-4}, where a peak with a maximum of 1.8×10^{-2} appears at the point $y = 0.67$ (corresponding to the intersection of the $x = x_2$ ray and the trace of the SiO_2/Si-corner trajectory). Curve *3* in Fig. 3d corresponds to $C(x_3, y)$ on the $x_3 = 0.8$ ray. This ray passes (Fig. 3a) through the region of Si material ($y < 0.5$), goes along the SiO_2/Si-wave front ($0.5 < y < 0.8$), and then passes through the SiO_2 oxide ($y > 0.8$). Accordingly, $C(x_3, y)$ is equal to its constant background value of 10^{-4} in the Si region and drops from 10^{-4} to 0.3×10^{-4} in the second region. Note that the curve in this region also has a plateau, after which $C(x_3, y)$ increases to its maximum value of 1.1×10^{-4} at the concave corner of the boundary, where an additional portion of impurity is injected. Understandably, $C(x_3, y)$ acquires its background value after passing through the SiO_2/Si front into the region of initial SiO_2.

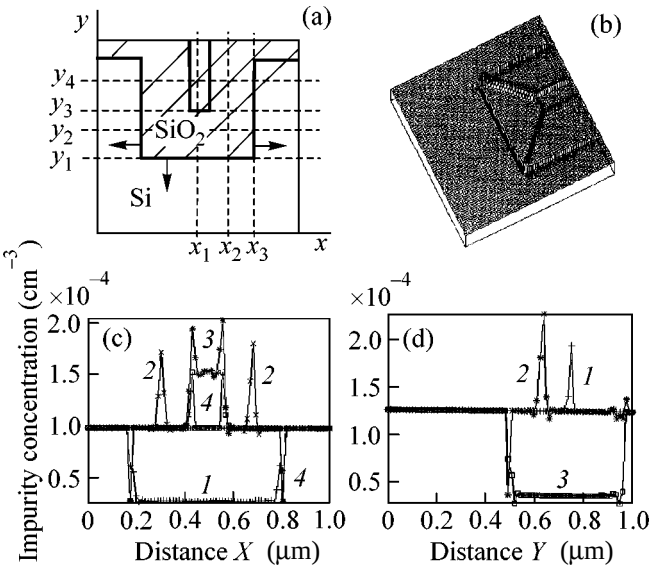

Fig. 3. Segregation at the cavity of the trench type. (a) General topology of the problem; (b) isometric projection of the $C(x, y)$ concentration in the computational region; (c) $C(x, y_i)$ distributions for $y_i = 0.5$, 0.62, 0.75, and 0.86 (curves *1–4*); and (d) $C(x_i, y)$ distributions for $x_i = 0.5$, 0.67, and 0.8 (curves *1–3*).

Segregation in a cavity of the square type. Contrary to the preceding cases, this configuration (Fig. 4a) has the shape of a closed area of oxide surrounded by the material on all sides. Square-type geometry, as well as trench geometry, is often used for the oxidation process in semiconductor materials design. The isometric projection of the impurity segregation at the moving SiO_2/Si boundary is qualitatively illustrated in Fig. 4b. The process is characterized by the presence of four oxidation fronts moving from the center to the periphery, four stationary traces of the initial SiO_2/Si fronts, and four semidiagonals corresponding to the trajectories of corner points. The $C(x, y)$ concentrations are characterized by the presence of dips at the fronts, ridges on the semidiagonals, and a flat field in between. A quantitative analysis of the impurity distribution $C(x, y)$ in the substrate can be carried out by analyzing the one-dimensional sections of $C(x, y_i)$ along the $y_1 = 0.2$, $y_2 = 0.3$, and $y_3 = 0.5$ rays at time $t = 50$ (Fig. 4c). Curve *1*, corresponding to the $C(x, y_1)$ values, passes through the Si region ($x < 0.2$ and $x > 0.8$) and along the SiO_2/Si front ($0.2 < x < 0.8$). As before, it represents a 0.3×10^{-4} plateau in the second (central) subarea and becomes a plateau of background values of 10^{-4} to the left and right. The $C(x, y_2)$ distribution (curve *2* in Fig. 4c) shows two 0.3×10^{-4} dips at the SiO_2/Si fronts ($x = 0.2$ and 0.8) and two peaks of a height of 1.8×10^{-4} at the intersection points of the y_2 ray and the corner tra-

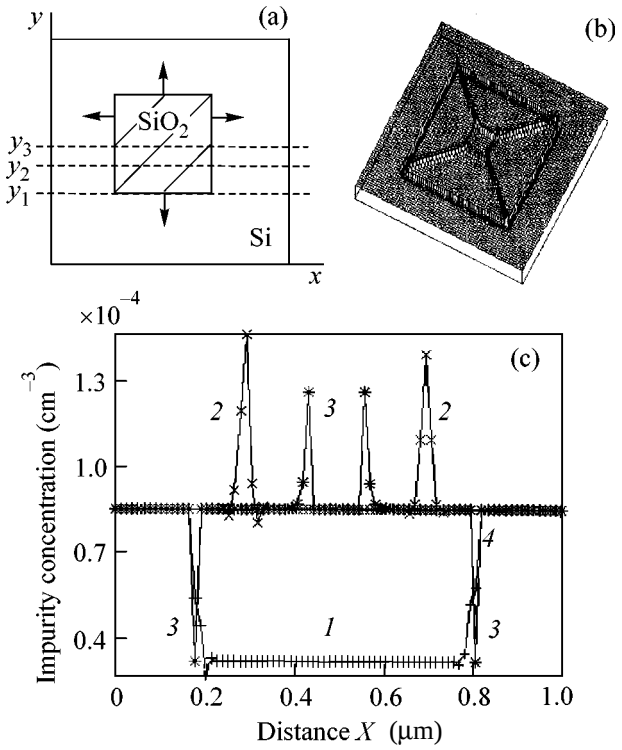

Fig. 4. Segregation at the cavity of the square type. (a) General topology of the problem; (b) isometric projection of the $C(x, y)$ concentration in the computational region; (c) $C(x, y_i)$ distributions for $y_i = 0.2$, 0.3, and 0.5 (curves *1–3*).

jectories ($x = 0.3$ and 0.7). The background concentration between the peaks and dips is equal to 10^{-4}. A small difference between the heights of the left and right peaks is due to the computational algorithm; it is associated with either clockwise or counterclockwise sense of going along the SiO_2/Si boundary (for details, see [1]). Curve *3* (Fig. 4c) corresponds to the $C(x, y_3)$ distribution. This curve is also symmetric about $x = 0.5$ and has five characteristic segments: the Si region ($x < 0.2$); the SiO_2/Si front intersections ($x = 0.2$ and 0.8); the SiO_2 region ($0.2 < x < 0.8$); and the region of initial oxide ($0.45 < x < 0.55$). In the Si and SiO_2 regions, the concentrations are equal to their background value of 10^{-4}, with two 0.3×10^{-4} dips occurring at the segregation fronts. At the initial fronts of the SiO_2/Si boundary ($x = 0.45$ and 0.55), there are concentrations peaks of 1.55×10^{-4} that are formed at the starting period of the oxidation wave motion. Note that the peaks in curves *2* and *3* have different origins.

REFERENCES

1. G. A. Tarnavsky, S. I. Shpak, and M. S. Obrecht, Vychisl. Mat. Programm. **2**, 12 (2001); http:www.srcc.msu./num-meth.
2. P. Deroux-Dauphin and J. P. Gonchand, J. Electrochem. Soc. **131**, 1418 (1984).
3. R. B. Fair and J. C. C. Tsai, J. Electrochem. Soc. **127**, 2243 (1980).
4. K. Tanigushi, K. Kurosava, and M. Kashiwagi, J. Electrochem. Soc. **125**, 2050 (1978).
5. A. Seidl and M. Svoboda, IEEE Trans. Electron Devices **ED-32**, 1960 (1986).
6. Dao Khac An and F. Pavlyak, Phys. Status Solidi A **95**, K117 (1986).
7. V. I. Kol'dyaev, V. A. Moroz, and S. A. Nazarov, Avtometriya **3**, 46 (1988).
8. V. N. Chebotin, *Physical Chemistry of Solid State* (Nauka, Moscow, 1982).
9. G. É. Tsirlin, P. Werner, G. Gösele, *et al.*, Pis'ma Zh. Tekh. Fiz. **27** (1), 31 (2001) [Tech. Phys. Lett. **27**, 14 (2001)].
10. E. V. Astrova, V. V. Ratnikov, A. D. Remenyuk, *et al.*, Pis'ma Zh. Tekh. Fiz. **27** (2), 1 (2001) [Tech. Phys. Lett. **27**, 41 (2001)].

Translated by V. Sakun

JETP Letters, Vol. 73, No. 9, 2001, pp. 479–482. From Pis'ma v Zhurnal Éksperimental'noĭ i Teoreticheskoĭ Fiziki, Vol. 73, No. 9, 2001, pp. 542–545.

Low-Temperature Kinetics of 2D Exciton Gas Cooling in Quantum Well Bilayer[1]

S. V. Iordanski and A. Kashuba

Landau Institute for Theoretical Physics, Russian Academy of Sciences, Moscow, 117940 Russia

Received March 27, 2001

We study the kinetics of 2D Bose gas cooling provided Bose particles interact with 3D phonons. At low temperatures, phonon emission is prohibited by energy and momentum conservation. We show that both particle–particle scattering and impurity scattering assist Bose gas cooling. The temporal relaxation of temperature follows the law $T \sim 1/\sqrt{t}$ above the Berezinski–Kosterlitz–Thouless phase transition point and $T \sim 1/t$ after a Bose–Einstein 2D quasi-condensate develops. © *2001 MAIK "Nauka/Interperiodica".*

PACS numbers: 71.35.Lk; 73.21.Fg; 05.30.Jp

Exciton gas in GaAs bilayer quantum represents well a system where a 2D Bose–Einstein quasi-condensation (BEqC) is possible at low temperatures. Experimental efforts [1, 2] have been directed to produce such an exciton gas and to cool it down to BEqC temperature. A short laser photoillumination pulse excites electron and hole pairs. The so-called indirect exciton technique is used where a perpendicular electric field drags electrons and holes apart into two spatially separated layers. Then, an electron and a hole bind themselves into an indirect exciton particle. This experimental setup suppresses the electron–hole recombination giving rise to a relatively long exciton lifetime. During the initial photoexcitation pulse, newly born excitons are hot and form a nonequilibrium state. A short time after the pulse ends, the exciton gas reaches equilibrium at some effective exciton temperature which is much higher than the lattice temperature of the cold GaAs crystal. Frequent exciton–exciton collisions ensure that the exciton temperature is uniform across the bilayer. Exciton gas then starts to cool down slowly due to emission of phonons into a crystal away from the bilayer. This is the longest phase of the experiment limited only by a decay time of excitons due to the electron–hole recombination. In order to reach the BEqC point, one needs both low temperature and a high density of excitons. Hence, a fast cooling is essential.

An important point is that the phonon emission gives the only way for exciton gas to cool. Otherwise, it is a closed system with conserved energy. Recent calculation of energy losses in a 2D ideal exciton system has predicted an extremely slow cooling at low temperatures with the temporal law $T(t) \sim 1/\log(t)$, where t is the time [3]. This fact is intimately related to the energy and momentum conservation, which prohibits an emission of phonons by an exciton moving slower than the velocity of sound in GaAs crystal c. Thus, the exciton gas cooling appears to stop when the exciton temperature falls below a characteristic blocking temperature $T_b = mc^2/2$, where m is the mass of exciton, even if the crystal temperature is zero.

This kinetic bottleneck problem becomes especially acute when the exciton gas is subjected to a strong perpendicular magnetic field that quenches the motion of exciton to the lowest Landau level and, thus, helps to bind electrons and holes into exciton pairs. In this case, the effective mass of an exciton is determined by the Coulomb interaction and can be much larger than either the electron or the hole mass [4]. This results in a higher blocking temperature T_b and makes it difficult to reach low temperatures in the end.

In this communication, we supplement the analysis of exciton cooling of [3] by an addition of exciton–exciton collisions and scattering on impurities. Both events assist the phonon emission. We specialize in the case of exactly zero lattice temperature, which allows us to neglect exciton–phonon scattering. Actually we are dealing with a general problem of 2D Bose gas cooling provided its particles interact with 3D phonons. The universal nature of 2D scattering at low energy of incoming particles makes these two assistance mechanisms robust to specific details of a particle–particle or impurity potential. The latter is only assumed to be short-ranged, with the characteristic interaction radius r_0 being shorter than the DeBroigle wavelength. For example, the indirect exciton interacts with an impurity or another exciton via the electron–hole dipole moment $e\mathbf{d}$, directed along the normal to the bilayer. Hence, the radius of such a dipole interaction is equal to the spacing between the electron and the hole layers $r_0 \sim d$.

[1] This article was submitted by the authors in English.

The Hamiltonian of the particle phonon interaction can be written generally as

$$H_{x-ph} = \iint \psi^+(\mathbf{r})\psi(\mathbf{r})\delta(z)\Gamma_i(\boldsymbol{\rho}-\boldsymbol{\rho}')u_i(\boldsymbol{\rho}')d^3\boldsymbol{\rho}'d^2\mathbf{r}dz, \quad (1)$$

where $\boldsymbol{\rho} = (\mathbf{r}, z)$, ψ^+ and ψ are the particle creation and annihilation operators and $\mathbf{u}$ is a crystal deformation induced by an acoustic phonon. Wavelengths of relevant phonons are much larger than the width of the bilayer d. The lattice deformation $\mathbf{u}$ can be expanded into the normal phonon modes as

$$u_i(\boldsymbol{\rho}) = \sum_{s,\mathbf{q}}\left(\frac{\hbar}{2\rho\omega_s(\mathbf{q})}\right)^{1/2} \times (e_i^s b_s^+(-\mathbf{q}) + e_i^{*s} b_s(\mathbf{q}))e^{i\mathbf{q}\boldsymbol{\rho}}, \quad (2)$$

where b_s^+ and b_s are the phonon creation and annihilation operators of polarization s; ρ is the mass density of solid; and $\omega_s(\mathbf{q}) = cq$ is the phonon frequency dispersion, which we assume to be isotropic and independent of phonon polarization s.

The exciton phonon interaction in GaAs crystal can be separated into piezoelectric and deformation potential parts. Lattice deformation in a piezoelectric crystal induces a polarization density $P_i = \beta_{ijk}\partial_j u_k$ [5], where β_{ijk} is the piezoelectric tensor. This polarization interacts with the exciton dipole moment. In the limit $qd \ll 1$, the deformation potential for an exciton Θ is a sum of the deformation potentials for an electron and a hole taken at the same spatial point. The latter represents a change of the semiconductor gap due to the local compression caused by a phonon deformation. Combining the piezoelectric and deformation parts and expanding the crystal lattice deformation in acoustic phonon modes, we write the exciton–phonon vertex in the Hamiltonian (1) as [5]

$$\Gamma_i(\mathbf{q}) = \left(\Theta q_i + ed\beta_{ijk}\frac{4\pi q_z q_j q_k}{\mathbf{q}^2}\right). \quad (3)$$

For a cubic GaAs crystal without the inversion center, $\beta_{ijk} = \beta$ if all i, j, k are different and zero otherwise. In the limit of large d, the piezoelectric part dominates over the deformation potential, but in the experiments [1, 2] $d \approx 50$ Å and both exciton–phonon interaction terms are of the same order of magnitude $\Theta \approx 4\pi ed\beta \approx 10$ eV.

The amplitude of phonon emission is given to the lowest order of perturbation theory by the matrix element

$$M_{if}^s(\mathbf{q}) = \langle f\mathbf{q}s|H_{ph}|i0\rangle \quad (4)$$

between initial state of Bose gas $|i0\rangle$ with no phonons and the final state of Bose gas $|f\mathbf{q}s\rangle$ with just one phonon specified by the momentum $\mathbf{q}$ and the polarization s. We assume that the thermalization of the Bose gas due to particle–particle scattering is much faster than the slow cooling due to phonon emission. Thus, at any given time t, the Bose gas is characterized by an effective temperature $T(t)$. This temperature defines the total gas energy $E = E(T)$. The Fermi Golden Rule gives the probability of phonon emission per unit time, and one needs to multiply it by the phonon energy $\omega_s(\mathbf{q}) = cq$ to find the total energy losses

$$\frac{dE}{dt} = -\frac{2\pi}{\hbar}\sum_{f\mathbf{q}s} cq\left|M_{if}^s(\mathbf{q})\right|^2\delta(E_i - E_f - cq). \quad (5)$$

Equation (5) has to be averaged over the Gibbs distribution of the initial state with the effective temperature $T(t)$. Both the initial and the final states of the Bose gas are calculated in the interaction representation (see, e.g., [6]). Particles are confined to the 2D layer, and the energy losses are proportional to the area of this layer.

In the experiments [1, 2], the exciton gas is dilute $nr_0^2 \ll 1$. Popov has shown [7] that for a 2D dilute Bose gas there is a 2D Berezinski–Kosterlitz–Thouless phase transition point,

$$T_c = \frac{2\pi n\hbar^2}{gm\log L}, \quad (6)$$

that separates high-T almost ideal Bose gas phase from the low-T superfluid phase. Actually, Popov theory is controlled by the large logarithm

$$L \approx -\log(nr_0^2) \approx \log\frac{E_0}{T_c}, \quad (7)$$

where n is the particle density, $E_0 = \hbar^2/r_0^2 m$, and g is the particle internal degeneracy [7]. For a Bose particle, $g = 2S + 1$, where S is the spin of particle. It was shown in [8] that electron and hole spins flip rapidly due to the spin–orbit interaction. Thus, $g = 4$ for a GaAs exciton.

For 2D dilute nonideal Bose gas, one can distinguish three temperature regions. At high temperatures $T \gg T_c \log L$, the ideal Bose gas is a good approximation. At intermediate temperatures $gT_c/L \ll T \ll T_c/\log L$, an overwhelming amount of particles constitute 2D BEqC with the density

$$n_s = n(1 - T/T_c), \quad (8)$$

whereas a small fraction of thermal particles have the bare dispersion and Bose distribution with the chemical potential $\mu \approx gT_c/L$ [7]. At low temperatures $T \ll \mu$, a weak particle–particle interaction is crucial and the quasiparticle excitations of the Bose system acquire Bogoliubov soundlike dispersion. Here, the transfer of momentum to impurity becomes inefficient because the quasiparticle has a vanishing scattering cross section on a pointlike impurity. In the case of excitons in GaAs crystal, the intermediate-T region hardly exists at all.

At $T \gg T_b$, a phonon is emitted perpendicular to the layer. Using Eq. (5), we calculate the total energy losses here:

$$\hbar \frac{dE}{dt} = -\frac{T_b T^3}{2\pi T_{x-ph}^2} An, \tag{9}$$

where A is the total area of bilayer. It is convenient to define a characteristic exciton–phonon energy:

$$T_{x-ph} = \sqrt{\frac{\rho c^5 \hbar^3}{\Theta^2 + (4\pi de\beta)^2/15}}. \tag{10}$$

In the case of GaAs, $T_{x-ph} \approx 5$ K. Using the ideal gas equation of state, $E(T) = AnT$, we get the temperature relaxation law: $T(t) \sim 1/\sqrt{t}$.

At $T \ll T_b$, an unassisted phonon emission is forbidden. Figure 1 shows two ways of particle scattering accompanied by an acoustic phonon emission. The left diagram shows a scattering on the second particle, and the right diagram shows a scattering on impurity. First, we treat this problem in the high-T and intermediate-T regions where particles have the bare dispersion: $\epsilon = \mathbf{p}^2/2m$. 2D scattering amplitudes in both cases are isotropic and depend only on the total kinetic energy in the center of mass frame: $\mathscr{E}$ (in the impurity case $\mathscr{E} = \epsilon$) in the limit $\mathscr{E} \longrightarrow 0$:

$$F(\mathscr{E}) = -\frac{2\pi\hbar^2}{m^*}\left(\log\frac{E_0}{\mathscr{E} r_0^2 m}\right)^{-1}, \tag{11}$$

where $m^* = m/2$ for particle–particle scattering and $m^* = m$ for the impurity scattering (see, e.g., [7]). Both the particle–particle interaction line and the impurity line on Fig. 1 correspond to the scattering amplitude $F(\mathscr{E})$. The total amplitude of assisted phonon emission is universal in both cases and is given by the following matrix element:

$$M_{if}^s(\mathbf{q}) = C\left(F(\mathscr{E})\frac{1}{cq} + F(\mathscr{E} - cq)\frac{1}{-cq}\right) e_i^s \Gamma_i(\mathbf{q}) \sqrt{\frac{q}{2\rho c}}, \tag{12}$$

where $C = 2$ for the particle–particle scattering and $C = 1$ for the impurity scattering. We neglect the phonon momentum transfer $\mathbf{q}_\parallel$ to the particle because $q_\parallel \ll p$, $p' \ll cm$, if $T \ll T_b$.

Plugging Eqs. (12) and (3) into Eq. (5) and taking the integral over the final state of the Bose gas, we obtain the total energy losses per unit time. In the high-T region we get

$$\frac{dE}{dt} = -\frac{2\pi c^3}{\hbar T_{x-ph}^2}\int\left(\frac{1}{\log(E_0/\epsilon)} - \frac{1}{\log(E_0/\epsilon')}\right)^2 \times K(\epsilon, T)\delta(\epsilon - \epsilon' - cq)\, d\epsilon\, d\epsilon' \frac{d^3\mathbf{q}}{(2\pi)^3}, \tag{13}$$

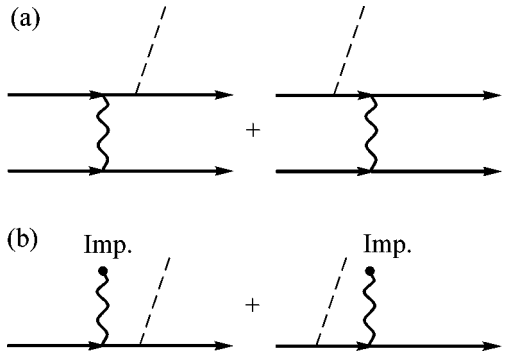

Fig. 1 Amplitude of exciton–exciton scattering (a) and exciton–impurity scattering (b) accompanied by phonon emission. Full lines correspond to the propagation of exciton, and dotted lines correspond to the propagation of phonon. Wavy line describes interaction either between excitons or exciton and impurity.

where $K(\epsilon, T) = 2AnN(\epsilon)(1 + 1/g)$ in the case o f particle–particle scattering and $K(\epsilon, T) = An_{imp}N(\epsilon)/2$ in the case of impurity scattering. n_{imp} is the areal density of impurities, and

$$N(\epsilon) = \frac{1}{\exp((\epsilon - \mu)/T) - 1} \tag{14}$$

is the Bose–Einstein occupation number. Combining the particle–particle and impurity contributions, we find the total cooling rate:

$$\frac{dT}{dt} = -(4(1 + 1/g)n + n_{imp})\frac{85}{9m}\frac{\hbar}{L^4}\frac{T^3}{T_{x-ph}^2}. \tag{15}$$

From Eqs. (9) and (15), we conclude that the temperature dependence of the 2D Bose gas cooling rate is the same above and below the phonon emission threshold: $T = T_b$.

In the intermediate-T region at $g = 1$, the cooling rate is enhanced by the stimulated scattering into the BEqC final states:

$$\frac{dT}{dt} = -n_s\left(64 n_s\left(1 - \frac{\zeta(3)}{\zeta(2)}\right) + n_{imp}\frac{\zeta(3)}{\zeta(2)}\right) \times \frac{2\pi\hbar^3}{m^2}\frac{\log^2 L}{L^4}\frac{T^2}{T_{x-ph}^2}. \tag{16}$$

In the low-T region, the thermodynamic equation of state reads $E(T) = A\zeta(3)T^3/\pi s^2$, where s is the Bogoliubov sound velocity: $s = \sqrt{\mu/m}$. In order to calculate the energy losses, we apply the Bogoliubov unitary transformation to the Hamiltonian (1):

$$H_{ph} = -\sum_{\mathbf{pq}} \frac{\mu}{2\epsilon(\mathbf{p})} \psi^+(\mathbf{p})\psi^+(-\mathbf{p} + \mathbf{q})\Gamma_i(\mathbf{q})u_i(\mathbf{q}) + \text{c.c.} \tag{17}$$

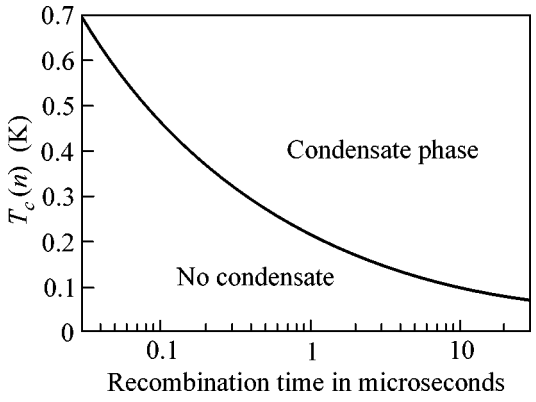

Fig. 2. Kinetic phase diagram showing the possibility of reaching a Bose–Einstein quasi-condensate phase in the GaAs indirect exciton bilayer.

This Hamiltonian allows emission of phonons. The cooling rate in this case is also enhanced by the condensate stimulation:

$$\frac{dT}{dt} = -\frac{\mu^2}{\hbar\pi T_{x-ph}^2}\left(1-\frac{\zeta(4)}{\zeta(3)}\right)T^2. \qquad (18)$$

In both cases of condensate stimulation, we find the temperature relaxation law: $T(t) \sim 1/t$.

For experimental realization of exciton cooling, the most relevant is Eq. (15). Integrating it and inserting $L \approx 6$ and $n \gg n_{imp}$, we find the overall cooling time t_c required to reach the phase transition point. Here, one can distinguish between two cases: (i) cooling of exciton gas with constant density, e.g., sustained by photoexcitation, and (ii) cooling of decaying exciton gas with $n(t) = n_0\exp(-t/\tau_r)$, where τ_r is the exciton recombination time. We find

$$t_c = C\hbar T_{x-ph}^2/T_c(n)^3, \qquad (19)$$

where $T_c(n)$ is the BKT temperature as a function of the exciton density n (6), and $C \approx 10$ in the case (i) and $C \approx 30$ in the case (ii). Note that C does not depend on exciton mass m and in the case (ii) the best condition for reaching T_c occurs at $t = \tau_r/3$. Equation (19) defines a line in the bilayer parameter space: (n, τ_r) or equivalently $(T_c(n), \tau_r)$, separating the two kinetic phases—one that can condense and the second that remains above T_c during the exciton life time τ_r. Figure 2 shows this borderline for the case of a thin GaAs bilayer.

We thank L.V. Butov and V.B. Timofeev for useful discussions. This work was supported by the Russian Foundation for Basic Research, project no. 01-02-17520, and INTAS, grant no. 97-31980.

REFERENCES

1. L. V. Butov, A. Imamoglu, A. V. Mintsev, *et al.*, Phys. Rev. B **59**, 1625 (1999); L. V. Butov and A. I. Filin, Phys. Rev. B **58**, 1980 (1998).
2. A. V. Larionov, V. B. Timofeev, I. Hvam, and R. Soerensen, Zh. Éksp. Teor. Fiz. **117**, 1255 (2000) [JETP **90**, 1093 (2000)].
3. A. L. Ivanov, P. B. Littelwood, and H. Haug, Phys. Rev. B **59**, 5032 (1999).
4. Yu. E. Lozovik and A. M. Ruvinskii, Zh. Éksp. Teor. Fiz. **112**, 1791 (1997) [JETP **85**, 979 (1997)].
5. V. F. Gantmakher and Y. B. Levinson, *Scattering of Charge Carriers in Metals and Semiconductors* (Nauka, Moscow, 1984).
6. A. A. Abrikosov, L. P. Gor'kov, and I. E. Dzyaloshinskii, *Methods of Quantum Field Theory in Statistical Physics* (Fizmatgiz, Moscow, 1962; Prentice-Hall, Englewood Cliffs, 1963).
7. P. N. Brusov and V. N. Popov, *Superfluidity and Collective Properties of Quantum Liquids* (Nauka, Moscow, 1988); D. S. Fisher and P. C. Hohenberg, Phys. Rev. B **37**, 4936 (1988).
8. A. Vinattieri, J. Shah, T. C. Damen, *et al.*, Phys. Rev. B **50**, 10868 (1994).

JETP Letters, Vol. 73, No. 9, 2001, pp. 483–486. Translated from Pis'ma v Zhurnal Éksperimental'noĭ i Teoreticheskoĭ Fiziki, Vol. 73, No. 9, 2001, pp. 546–550.

Chaos and Self-Organization in an Open Nonconservative System of Two Plane Coplanar Magnetized Bodies with Moments of Inertia

F. V. Lisovskiĭ[1,*] and O. P. Polyakov[2]

[1] *Institute of Radio Engineering and Electronics, Russian Academy of Sciences, Fryazino, Moscow region, 141120 Russia*
** e-mail: lisf@dataforce.net*

[2] *Moscow State University, Moscow, 119899 Russia*

Received January 25, 2001; in final form, March 27, 2001

Numerical analysis is used to study the nonlinear oscillation processes in an open nonconservative system of two plane coplanar magnetized bodies with moments of inertia. Bifurcation diagrams that illustrate different dynamic regimes of the system in an oscillating magnetic field, as well as the possibility of transitions from one regime to another due to variations in the parameters of the external action, are obtained. It is established that, for the regimes corresponding to infinite phase trajectories, in the general case, an asymmetry occurs in the choice of the rotation direction of the magnetized bodies. *© 2001 MAIK "Nauka/Interperiodica".*

PACS numbers: 75.70.Kw; 05.65.+b; 05.45.-a

It is well known that the ground state of a finite-size ferromagnet is in most cases magnetically nonuniform, whereas, in the presence of nonstationary external actions of a certain type, it exhibits a self-organization with the formation of completely or partially ordered domain structures (see, e.g., [1–3]). Several attempts were made to describe mathematically the dynamical processes that occur in this case by the nonlinear Landau–Lifshits equation with the use of analytical methods [4–6]. However, these attempts did not result in any major breakthrough. Presumably, some progress can be achieved with the help of a numerical analysis based on modern computational techniques. Such an approach allowed us earlier [7] to establish that a system consisting of two "massless" magnetic dipoles, which are bound by a dipole interaction, exhibits a stochastic behavior in the presence of an oscillating magnetic field [7]. Further studies showed that a full dynamic portrait of such a system with four degrees of freedom can hardly be obtained at the moment, even with the most advanced high-performance computers. This paper presents an attempt to make the physical model used in [7] as rough as possible (with retaining the ability for the chaotization of oscillations) by excluding the precession component of the magnetic dipole motion.

In the proposed model, each of the two magnetic dipoles is a centrosymmetric quasi-two-dimensional object with a moment of inertia; the object is elongated in one direction and magnetized along the same direction (an object of a type of magnetic compass needle). In addition, the symmetry of the object is characterized by the presence of a mirror plane passing through the center of symmetry normally to the plane of the object. We assume that the dipoles have a rotation axis passing through the center of symmetry, which also is the center of inertia. The magnetic needles are assumed to be made of a hard magnetic material (with an infinitely large coercive force).

The numerical calculation was performed for the following geometric configuration. The plane of the dipole rotation was the *XY* coordinate plane; the rotation axes of the dipoles with the magnetic moments $\mathbf{p}_1$ and $\mathbf{p}_2$ lay on the *X* axis, and the distance between them was $\mathbf{r} = a\mathbf{e}_x$. The angular positions of the magnetic needles at any instant of time *t* were uniquely determined by the angles $\phi_1(t)$ and $\phi_2(t)$, where $\phi_i = \arctan(p_{iy}/p_{ix})$.

In the absence of external actions, such a system has two equilibrium states (the centers or attractors of a "stable focus" or "node" type) for which the equalities $\phi_1 = \phi_2 = 0$ and $\phi_1 = \phi_2 = \pi$ are satisfied. The choice of one of the two equilibrium configurations is determined by the values of the angles $\phi_1^{(0)} = \phi_1(0)$ and $\phi_2^{(0)} = \phi_2(0)$ at zero time. In the presence of an alternating external magnetic field $\mathbf{H}\sin(\omega t)$ with the field vector lying in the *XY* plane and oriented at an angle ϕ_H to the *X* axis, the magnetic needles will experience rotational moments $\mathbf{K}_{1,2}$ caused by the Zeeman and dipole–dipole interactions:

$$\mathbf{K}_{1,2} = \left[\mathbf{p}_{1,2}, \left(\mathbf{H}\sin(\omega t) + \frac{3\mathbf{r}_{2,1}(\mathbf{p}_{2,1}\mathbf{r}_{2,1}) - a^2\mathbf{p}_{2,1}}{a^5}\right)\right]. \quad (1)$$

0021-3640/01/7309-0483$21.00 © 2001 MAIK "Nauka/Interperiodica"

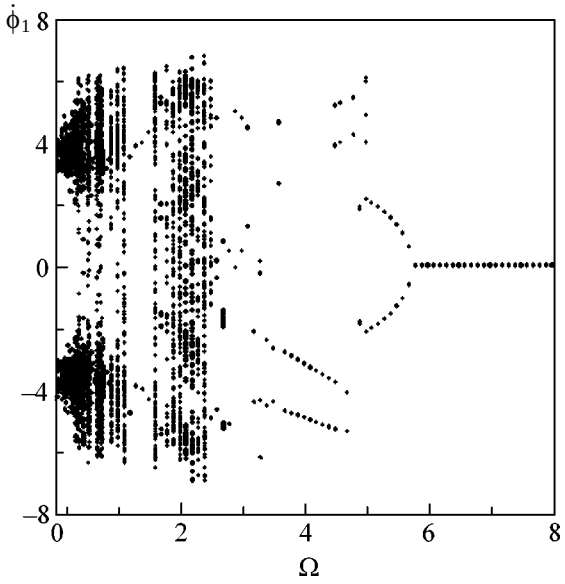

Fig. 1. Dependence of the maximal and minimal values of $\dot{\phi}_1$ on the normalized frequency of magnetic field.

Since, in the geometry under study, each rotational moment has only one nonzero component $K_{iz} = |\mathbf{K}_i| = K_i$, the time variation of the orientation of the magnetic needles with the moments of inertia J_1 and J_2 is described by the equations

$$J_i\frac{d^2\phi_i}{dt^2} + \alpha_i\frac{d\phi_i}{dt} = K_i, \tag{2}$$

where α_i are the damping constants. These equations can be represented in an explicit form:

$$\begin{aligned}\ddot{\phi}_1 &= -\sqrt{\frac{J_2}{J_1}}[\sin\phi_1\cos\phi_2 + \sin(\phi_1+\phi_2)]\\ &\quad -\beta_1\dot{\phi}_1 + \alpha_{H1}\sin(\phi_H-\phi_1)\sin(\Omega\tau),\\ \ddot{\phi}_2 &= -\sqrt{\frac{J_1}{J_2}}[\sin\phi_2\cos\phi_1 + \sin(\phi_1+\phi_2)]\\ &\quad -\beta_2\dot{\phi}_2 + \alpha_{H2}\sin(\phi_H-\phi_2)\sin(\Omega\tau),\end{aligned} \tag{3}$$

where a dot over a symbol denotes the differentiation with respect to the dimensionless time $\tau = \nu t$ and the dimensionless parameters β_i, α_{Hi}, and Ω are expressed through the initial parameters by the formulas

$$\begin{aligned}\beta_i &= \frac{\alpha_i}{\nu J_i};\quad \alpha_{H1} = \frac{Ha^3}{p_2}\sqrt{\frac{J_2}{J_1}};\\ \alpha_{H2} &= \frac{Ha^3}{p_1}\sqrt{\frac{J_1}{J_2}};\quad \Omega = \frac{\omega}{\nu};\quad \nu = \sqrt{\frac{p_1p_2}{a^3\sqrt{J_1J_2}}}.\end{aligned} \tag{4}$$

From general considerations, it follows that at least four different dynamic regimes can occur in the system under study. Regime I (with a limiting cycle) and regime II (without the limiting cycle) are characterized by a finite phase trajectory, and, in both these regimes, the dipoles oscillate about some dynamic equilibrium position with a peak-to-peak amplitude $\phi_{max} - \phi_{min}$ not exceeding 2π. Infinite phase trajectories correspond to regime III (with a limiting cycle) and regime IV (without the limiting cycle) in which the objects can perform as many revolutions as one likes about the rotation axes (clockwise or counterclockwise).

The typical results that were obtained from the numerical simulation of the behavior of the dynamic system under discussion for the simplest case of identical dipoles ($J_1 = J_2 = J$; $\alpha_1 = \alpha_2 = \alpha$; $\beta_1 = \beta_2 = \beta$) are presented in Figs. 1 and 2 in the form of bifurcation diagrams for the following initial conditions and values of internal parameters: $\phi_1(0) = 2.5$, $\phi_2(0) = \pi/4$, $\dot{\phi}_1(0) = \dot{\phi}_1(0) = 0$, $\alpha_H = 10$, $\beta = 0.3$, and $\phi_H = 0$.

Figure 1 shows the maximal and minimal values of the angular velocity $\dot{\phi}_1$ of the first magnetic dipole for each fixed value of Ω; the values of the angular velocity are those realized in the system in the course of the observation within the time interval $\Delta\tau$ far exceeding the time interval T_e between the neighboring extrema in the dependence of the angular velocity of the first dipole on the dimensionless time $\dot{\phi}_1(\tau)$.[1] If the set of extremum values contains a single element, we have either a stable state (a zero element) or a uniform rotation with $\dot{\phi}_{1max} = \dot{\phi}_{1min} = \text{const} \neq 0$. A two-element set corresponds to a simple cycle with a finite (for $\phi_{1max} = -\phi_{1min}$) or infinite (for $|\phi_{1max}| \neq |\phi_{1min}|$) phase trajectory. A four-element set and every $2n$-element set correspond to a twofold cycle and a cycle of order n, respectively, which can be with either a finite (for elements pairwise coincident in magnitude but different in sign) or an infinite (when ϕ_{1max} and ϕ_{1min} differ in magnitude) phase trajectory. In the case of a total dynamic chaos, the number of elements in the set of extremum values linearly increases (in proportion to the time of observation), and they fill uniformly a certain segment of the straight line $\Omega = \text{const}$.

The above consideration shows that the identification of the dynamic regimes which occur in the system under study by using only the bifurcation diagram presented in Fig. 1 can lead to ambiguous results. To eliminate this ambiguity, additional information is necessary: for example, the data on the time variations of the values of the function $\phi_1(\tau)$ (or $\phi_2(\tau)$) at the extremum points at $\Omega = \text{const}$. If, for $\tau \gg \tau_0$, these values remain invariant (correct to $2\pi n$), we deal with the fully deterministic regimes (with a limiting cycle), i.e., regime I

[1] In our case, $\Delta\tau = 100T_e$; the initial point τ_0 was chosen so as to eliminate the effect of transient processes occurring in the system on the results of observations for the dynamic regimes with a limiting cycle.

($n = 0$) or regime III ($n \neq 0$). A variation of these values within a bounded interval $\Delta\phi < 2\pi$ is an indication of regime II (chaotic oscillations of the dipoles near some middle position). If the value of $\Delta\phi$ grows without limit (in proportion to $\Delta\tau$), regime IV, i.e., a chaotic rotation of the dipoles, is observed. The data on the evolution of the values of the function ϕ_1 at the extremum points are shown in Fig. 2 for the same initial conditions and the same parameters as in the bifurcation diagram shown in Fig. 1.

The analysis of Figs. 1 and 2 with allowance for the above considerations shows that the high-frequency region corresponds to the equilibrium state,[2] whereas, at the point $\Omega \approx 5.7$, a Hopf bifurcation or a bifurcation of a simple cycle production (regime I with small oscillations of the dipoles near the equilibrium position) arises. As the normalized frequency decreases, the oscillation amplitude gradually increases and, at the second bifurcation value $\Omega \approx 5.0$, a transition to regime III with a complete revolution of the dipoles takes place (the production of twofold cycles, then fourfold cycles, etc.).

In the low-frequency region, below the third bifurcation value $\Omega \approx 2.5$, the system exhibits a chaotic behavior. In the diagram presented in Fig. 1, the points lying in this region are nonuniformly distributed with a tendency to being denser or sparser; i.e., the dynamic chaos is not absolute, but structured. In this case, regimes II and IV are realized. The regions corresponding to regime II are extremely narrow and localized near certain values of Ω, namely, $\Omega \approx 0.875$, $\Omega \approx 0.5$, $\Omega \approx 0.125$, etc. (see Fig. 2). In addition, the low-frequency region contains relatively wide zones of self-organization near the values $\Omega \approx 1.5$ and $\Omega \approx 1.75$, where attractors of the simple-cycle and twofold-limiting-cycle types, respectively, are observed.

The bifurcation diagrams presented in Figs. 1 and 2 also show that, in the general case, for regimes III and IV corresponding to infinite phase trajectories, an asymmetry in the choice of the rotation direction of magnetized bodies takes place. For example, when $\Omega \in [2.5, 5]$, the clockwise rotation of the first dipole ($\dot{\phi}_1 < 0$) is realized much more often than its counterclockwise rotation ($\dot{\phi}_1 > 0$). One can also see that, in some cases, the direction of the dipole rotation changes to the opposite as a result of an insignificant variation of the frequency Ω. The presence of such an asymmetry, which is a consequence of the asymmetry of the initial conditions for the first and second dipoles (at $\phi_1^{(0)} = \phi_2^{(0)}$, the asymmetry is absent), could be considered as a common phenomenon, were it not for the following fact: the asymmetry manifests itself to one or another

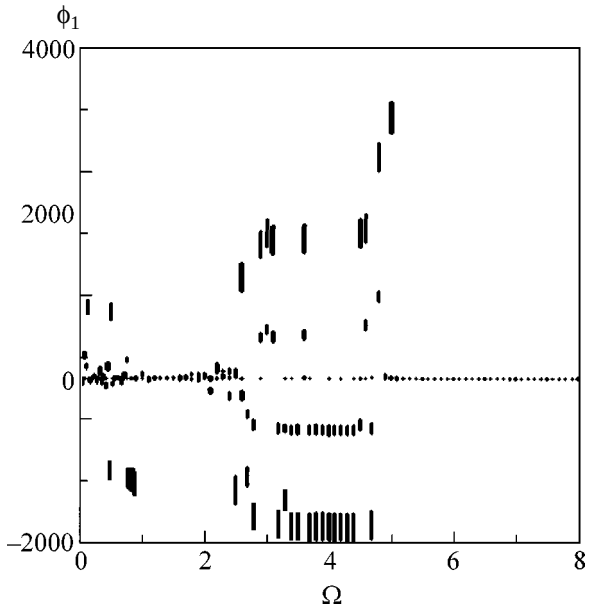

Fig. 2. Dependence of the maximal and minimal values of ϕ_1 on the normalized frequency of magnetic field.

extent for all values of Ω for which a complete revolution of the dipoles is realized in the system in both the deterministic and the chaotic regimes. In other words, the dynamic chaos in the system under study exhibits a memory for the initial conditions.

The analysis of the analogous bifurcation diagrams obtained for the second magnetized body with the same initial conditions and parameters as for the first body showed no qualitative difference in the dynamic behavior of the two objects under consideration. In the interval of the normalized frequency variation $0 < \Omega < 8.0$, for the second magnetized body we also obtained the zones of deterministic and chaotic behavior, the focus-type attractors, simple and multiple limiting cycles, the predominant clockwise rotation of the dipole in the regimes with an infinite phase trajectory, the self-organization regions within the frequency interval with a predominance of chaos, etc. However, it should be noted that, the changes in the rotation direction of the second object occur at other values of Ω than in the case of the first object; i.e., situations with opposite rotation directions of the magnetized bodies are possible.

A variation of the initial conditions causes no considerable changes in the dynamic behavior of the system under study. Nevertheless, when the initial deviation of the axis of the first dipole from the X axis decreases (above, we used the value $\phi_1(0) = 2.5$) and the initial position of the second dipole remains unchanged ($\phi_2(0) = \pi/4$), the number of Ω values at which the first dipole changes its rotation direction increases, and, when $\phi_1(0) \longrightarrow 0$, the cycles with the clockwise and counterclockwise rotations (for infinite phase trajectories) become of equal occurrence. However, these changes have practically no effect on the dynamic portrait of the second dipole, for which the asymmetry in

[2] With the selected value of the attenuation coefficient $\beta = 0.3$, the equilibrium states correspond to the attractors of the stable-focus type, because $\beta < \min\{\Omega_{0i}\}$, where Ω_{0i} are the eigenfrequencies of the system for low-amplitude oscillations (see below).

the choice of the rotation direction is retained even at $\phi_1(0) = 0$.

The aforementioned features of the dynamic processes that occur in the system under consideration are determined by the fact that its behavior is described by a system of equations with periodic coefficients in which the external action manifests itself not as a driving force, but as a factor modulating the internal parameters. For example, if we introduce new variables $\phi^{(+)} = \phi_1 + \phi_2$ and $\phi^{(-)} = \phi_1 - \phi_2$, the system of equations (3) will take the form

$$\begin{aligned}
&\ddot{\phi}^{(+)} + \beta\dot{\phi}^{(+)} + 3\sin\phi^{(+)} \\
&+ \alpha_H\left(\sin\frac{\phi^{(+)} + \phi^{(-)}}{2} + \sin\frac{\phi^{(+)} - \phi^{(-)}}{2}\right) = 0, \\
&\ddot{\phi}^{(-)} + \beta\dot{\phi}^{(-)} + \sin\phi^{(-)} \\
&+ \alpha_H\left(\sin\frac{\phi^{(+)} + \phi^{(-)}}{2} - \sin\frac{\phi^{(+)} - \phi^{(-)}}{2}\right) = 0.
\end{aligned} \tag{5}$$

A linearization of the system of equations (5) at $\alpha_H = 0$ leads to the equations

$$\begin{aligned}
\ddot{\phi}^{(+)} + \beta\dot{\phi}^{(+)} + 3\phi^{(+)} &= 0, \\
\ddot{\phi}^{(-)} + \beta\dot{\phi}^{(-)} + \phi^{(-)} &= 0;
\end{aligned} \tag{6}$$

i.e., in the low-amplitude approximation, the normal coordinates of the system are the quantities $\phi^{(+)}$ and $\phi^{(-)}$ whose variations represent the in-phase and antiphase oscillations, respectively, of the magnetic dipoles with the normal frequencies $\Omega_0^{(+)} = \sqrt{3}$ and $\Omega_0^{(-)} = 1$.

It is well known that, for the equations with periodic coefficients of a similar type (e.g., for the Hill equation) that describe the behavior of systems with one degree of freedom, the alternation of the domains of stable and unstable solutions in the frequency space is typical (see, e.g., [8]). In the absence of attenuation, unstable solutions can exist at any nonzero amplitude A of the external action; a dissipation gives rise to an instability threshold. The instability zones in the (A, Ω) plane lie near the values $\Omega = n\frac{\Omega_0}{2}$, where Ω_0 is the resonance frequency for free (undamped) oscillations. Although the system studied in this paper is more complex, one must take into account that the frequency intervals with a deterministic dynamic behavior within the chaos region (Fig. 1) may occur because of the same reason.

In closing, we note that, in Figs. 1 and 2, the role of the bifurcation parameter is played by the variable Ω, which is a dimensionless combination of several dimensional parameters of the system. However, the analysis of Eqs. (4) shows that the expression for the normalizing factor involves only the geometric (the distance between the dipoles), magnetic (the magnetic moments of the dipoles), and mechanical (the moments of inertia) parameters; i.e., the Ω and ω axes are related by a simple similarity transformation. Therefore, in an experimental study of the processes studied in this paper, the bifurcation diagrams should be determined by varying the frequency of the external magnetic field with a constant distance between the dipoles; in correlating the experimental values of the instant angular velocities of the dipoles, one should take into account that the values presented in Fig. 1 (and corresponding to the derivatives with respect to the dimensionless time) differ from the real values by the factor ν^{-1}. For the bifurcation diagram regions that correspond to the complete revolutions of the dipoles, it is also necessary to take into account the presence of the dynamic memory in the system under study, i.e., the dependence of the experimental data on the initial conditions.

This work was supported by the Russian Foundation for Basic Research, project no. 99-02-17404.

REFERENCES

1. G. S. Kandaurova and A. É. Sviderskiĭ, Pis'ma Zh. Éksp. Teor. Fiz. **47**, 410 (1988) [JETP Lett. **47**, 490 (1988)].
2. F. V. Lisovskiĭ and E. G. Mansvetova, Pis'ma Zh. Éksp. Teor. Fiz. **55**, 34 (1992) [JETP Lett. **55**, 32 (1992)].
3. F. V. Lisovskiĭ, E. G. Mansvetova, and Ch. M. Pak, Zh. Éksp. Teor. Fiz. **108**, 2031 (1995) [JETP **81**, 567 (1995)].
4. I. E. Dikshteĭn, F. V. Lisovskiĭ, E. G. Mansvetova, and E. S. Chizhik, Zh. Éksp. Teor. Fiz. **100**, 1606 (1991) [Sov. Phys. JETP **73**, 888 (1991)].
5. A. G. Shagalov, Fiz. Met. Metalloved. **84**, 17 (1997).
6. V. E. Ivanov and G. S. Kandaurova, Fiz. Met. Metalloved. **87**, 571 (1999).
7. F. V. Lisovskiĭ and O. P. Polyakov, Pis'ma Zh. Éksp. Teor. Fiz. **68**, 643 (1998) [JETP Lett. **68**, 679 (1998)].
8. E. Kamke, *Differentialgleichungen*, Bd. I: *Gewöhnliche Differentialgleichungen* (Geest and Portig, Leipzig, 1964; Nauka, Moscow, 1976).

Translated by E. Golyamina

JETP Letters, Vol. 73, No. 9, 2001, pp. 487–490. Translated from Pis'ma v Zhurnal Éksperimental'noĭ i Teoreticheskoĭ Fiziki, Vol. 73, No. 9, 2001, pp. 551–555.

Nonthermal Structural Transformation in Quasi-Monocrystalline Graphite during 100-fs Laser Pulse

S. I. Kudryashov* and V. I. Emel'yanov

International Laser Center, Faculty of Physics, Moscow State University, Moscow, 119899 Russia

** e-mail: sergeikudryashov@chat.ru*

Received March 28, 2001

Nonthermal structural transformation in quasi-monocrystalline graphite excited by a laser pulse with a duration of 100 fs was directly confirmed by ellipsometry. © *2001 MAIK "Nauka/Interperiodica".*

PACS numbers: 61.80.Ba; 64.70.Kb

1. In the past decade, the hypothesis for "plasma-induced" nonthermal structural transitions initiated in semiconductors by intense femtosecond laser pulses has been confirmed both experimentally and theoretically in a number of works [1–7]. However, it is still hard to directly identify the resulting new disordered (including fluid) and crystalline phases, because the methods of linear and nonlinear optical diagnostics do not always provide the desired structural sensitivity of optical response and its unambiguous interpretation [1–5], while the more universal X-ray diffraction method [6, 7] does not meet the requirements for subpicosecond time resolution of the structural changes in a medium. Nevertheless, in some cases, the optical methods allow the direct observation of long-range order breaking on a subpicosecond time scale in materials with pronounced optical anisotropy, e.g., in graphite [8]. Graphite is also of interest because its structural transformations are of great fundamental and practical importance, not only in connection with the development of new methods for manufacturing diamond (e.g., by exposure to electron beams [9]) but also because of the lack of reliable data on the hypothetical graphite phases—carbyne and liquid phase [10, 11].

In this work, ellipsometry (self-reflection of *s*- and *p*-polarized pulses) was used to prove that a 100-fs laser pulse can initiate nonthermal plasma-induced structural transformations in a quasi-monocrystalline graphite.

2. A standard femtosecond laser setup of the Institute of Laser and Plasma Physics (University of Essen, Germany) was used, whose components (oscillator and regenerative and multipass sapphire amplifiers) were described in [12]. The laser output was 1.5 mJ per pulse (TEM_{00} mode) at a wavelength $\lambda \approx 800$ nm, a pulse (Gaussian) duration $\tau \approx 100$ fs (FWHM), a repetition rate of 10 Hz, and relative amplitude of the pre- and postpulses no higher than 5–7%. The focused polarized (*s* and *p*) beam was directed at an angle of 45° onto the basal plane of a wafer that was made from high-oriented pyrolytic type UPV1-TMO (quasi-monocrystalline) graphite and moved from pulse to pulse. The energy of mirror-reflected *s*- and *p*-polarized pump beams was measured by a pyroelectric detector at different energies of the incident single pulses. The pump-beam self-reflectivities R_s and R_p were measured as functions of pulse energy, and the corresponding curves were processed to eliminate their spatial averaging due to the inhomogeneous distribution of pump fluence F over the TEM_{00} beam spot on the wafer. The resulting R_{1s} and R_{1p} values are presented in Fig. 1 as functions of the effective (pulse-integrated) pump fluence $F_{\text{eff}} = (1 - R_{1s,\,p})F$. This allowed the curve portions corresponding to the identical conditions of sample excitation to be juxtaposed in the plot.

3. The analysis of the ellipsometric data carried out for quasi-monocrystalline graphite in [13], where it was considered as an isotropic medium, seems to be incorrect because of the pronounced structural anisotropy and anisotropy of physical (primarily optical) properties of this material. Indeed, for an oblique (45°) incidence of a beam on the sample basal plane perpendicular to the *C* axis, the electric vector *E* of the *s*-polarized beam lies in the surface plane ($E \perp C$) [$R_{1s}(F_{\text{eff}})$ in Fig. 2] and interacts with the "semimetallic" atomic planes in graphite ($n_\perp = 2.7$ and $k_\perp = 1.67$ [14]; $n_\perp = 3.1$ and $k_\perp = 1.9$ [15]; $n_\perp = 3$ and $k_\perp = 1.5$ [16]; the data are for $\lambda \approx 800$ nm) to excite electron–hole (e–h) plasma in them. By contrast, the *p*-polarized beam incident at 45° has two mutually perpendicular *E* components with identical amplitudes ($E \perp C$ and $E \parallel C$; hereafter $E_\perp$ and $E_\parallel$, respectively), of which the latter acts across the graphite planes (along the *C* axis) and has optical constants ($\lambda \approx 800$ nm) $n_\parallel = 1$ and $k_\parallel = 0.25$ [14], $n_\parallel = 1.4$ and $k_\parallel = 0.7$ [15], and $n_\parallel = 2$ and $k_\parallel = 0.13$ [16]. One can show that the mutually perpendicular $E_\perp$ components of the *s*- and *p*-polarized beams are virtually equivalent for the quasi-monocrystalline graphite with hexagonal structure. Thus, the interaction of the *s*- and, especially, *p*- polarized beam incident on

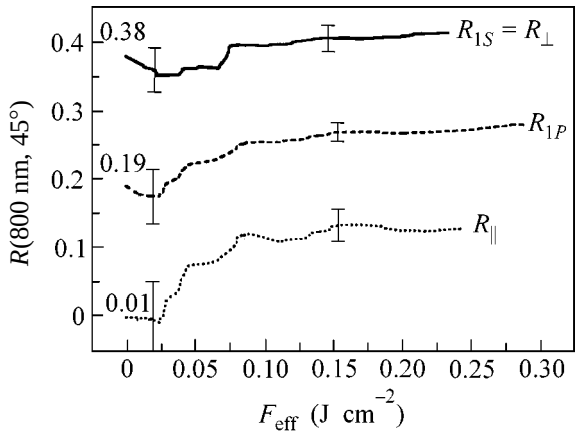

Fig. 1. Self-reflectivities $R_{1s} = R_\perp$, R_{1p}, and $R_\parallel$ as functions of effective (integrated) fluence F_{eff} of the pump beam. The confidence intervals (for $P = 0.95$, $N = 15$) and the calculated reflectivities of the unexcited graphite (data from [14–16]) are also given.

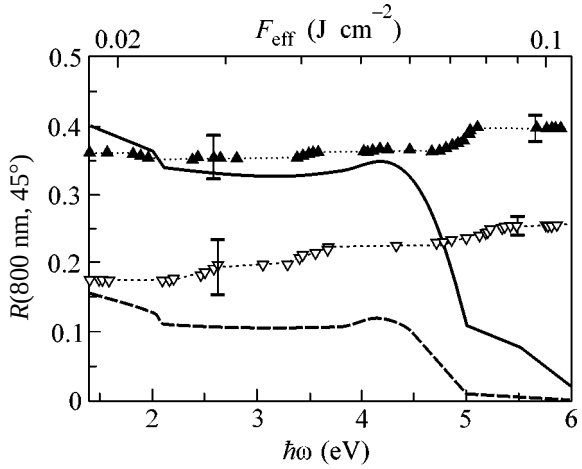

Fig. 2. Comparison of the $R_{1s}(F_{\text{eff}})$ (dark triangles) and $R_{1p}(F_{\text{eff}})$ (light triangles) dependences with the corresponding $R_{1s}(\hbar\omega)$ (solid line) and $R_{1p}(\hbar\omega)$ (dotted line) dependences calculated for the unexcited graphite using the data on $n_\perp$ and $k_\perp$ from [15].

the basal plane of graphite is characterized by two pairs of optical constants [$R_{1p}(F_{\text{eff}})$ in Fig. 2] that cannot be uniquely determined by ellipsometry from two measured parameters, namely, reflectivities for different polarizations or angles of incidence. However, in the diagnostics of graphite structural transformations, it is more important that the contribution from the *p*-polarization $E_\parallel$ component to the reflectivity, although being negligible for the unexcited sample, becomes comparable with the contribution from $E_\perp$ and, hence, appreciable after the structural transformation of graphite into a phase with weak anisotropy (amorphous substance, "cold" melt, or diamondlike phase).

Taking into account the effect of graphite anisotropy, the reflectivity for both beam polarizations at an incidence of 45° can be represented for the $E_\parallel$ and $E_\perp$ components as

$$F_{1s}^R = FR_{1s} = FR_\perp, \tag{1}$$

$$F_{1p}^R = FR_{1p} = F_\perp^R + F_\parallel^R = 0.5F(R_\perp + R_\parallel), \tag{2}$$

where F_{1s}^R and F_{1p}^R are the reflected fluences for the *s* and *p* polarizations, respectively, and incident fluence *F*, i.e., for $R_\perp = R_{1s}$:

$$R_\parallel = 2R_{1p} - R_{1s}. \tag{3}$$

The experimentally measured $R_{1s}(F_{\text{eff}})$ and $R_{1p}(F_{\text{eff}})$ reflectivities were used, together with Eqs. (1) and (3), to construct the $R_\perp(F_{\text{eff}})$ and $R_\parallel(F_{\text{eff}})$ curves (Fig. 1). The initial portion of the latter is scaled by a factor of 0.5 in the range $F_{\text{eff}} \le 0.025$ J cm^{-2} because the pumping was mainly provided by the $E_\perp$ component. It is notable that $R_\parallel$ is close to zero at $F_{\text{eff}} \le 0.025$ J cm^{-2}, confirming that the $E_\parallel$ component weakly interacts with graphite, in accordance with its optical properties along the *C* axis. The $R_\perp(F_{\text{eff}})$ curve shows a minimum in this range of F_{eff} values, indicating the onset of plasma effects—attainment of the plasma reflection edge or, due to the plasma-induced π-electron band-gap collapse, red shift in linear absorption of the $E_\perp$ component. Indeed, the pumping $E_\perp$ component undergoes strong linear absorption in graphite {α(800 nm) ≈ 3×10^5 cm^{-1} [15]}. Under the condition that the rate of optical e–h-plasma generation is equal to the Auger recombination rate, the data on the linear absorption in the indicated F_{eff} range yield, according to the expression

$$N_{\text{e–h}} \approx \sqrt[3]{\frac{\alpha F_{\text{eff}}}{\hbar\omega\gamma_A\tau}}, \tag{4}$$

a value higher than 10^{22} cm^{-3} for the upper limit of plasma density (estimates were made using the rate constant $\gamma_A = 4 \times 10^{-31}$ cm^6 s^{-1} for Si [17]). A comparison of the $R_\perp(F_{\text{eff}})$ curve with the $R_s(\hbar\omega)$ curve constructed for the unexcited graphite (Fig. 2) using the data from [15] shows that a change in $R_\perp$ in the range F_{eff} = 0.02–0.07 J cm^{-2} can be described within the framework of the hypothesis for the red shift in a linear absorption spectrum.

A sharp increase in $R_\parallel(F_{\text{eff}})$ at $F_{\text{eff}} > 0.025$ J cm^{-2} (Fig. 1) is due to a thresholdlike change in the optical properties in the *C* direction. At $F_{\text{eff}} > 0.08$ J cm^{-}, the $R_\parallel(F_{\text{eff}})$ curve flattens out at a level of about 0.12. The sharp increase in $R_\parallel(F_{\text{eff}})$ points to the fact that the minimum in the $R_\perp(F_{\text{eff}})$ curve is due not to the electronic effect alone, because the expected contribution from the e–h plasma does not account for the observed change in $R_\parallel(F_{\text{eff}})$. It is more conceivable that graphite

undergoes at $F_{eff} > 0.08$ J cm^{-2} a nonthermal structural transformation from the two-dimensional phase with pronounced anisotropy into a transient three-dimensional phase with weak anisotropy. This transformation occurs *within the pump pulse of a duration of 100 fs* [shorter than the period of optical or acoustic vibrations in graphite (2×10^{-13} s)] as a result of the well-known plasma-induced instability of acoustic modes [18, 19], likely, of the *TA* modes near the Brillouin zone boundary in our case. Indeed, the π-electron excitation to the antibonding states (conduction band) converts interlayer attraction into interlayer repulsion, thus causing mutual shift of the atomic planes in graphite (*TA* E_{2g} mode, 43 cm^{-1}), as was predicted in [20] and experimentally proved in [21]. The instability of this mode induces transition from the hexagonal graphite structure to the orthorhombic structure in which the planes may be linked together by the covalent bonds to form hexagonal or cubic diamond [22]. The density of the substance (2.26 g cm^{-3}) does not change in the course of structural transition during the 100-fs laser pulse, so that the interatomic distances in the transient diamondlike phase are appreciably larger than in the equilibrium diamond structure. As a result, the structure, the density, and, likely, the optical properties of the transient phase should be close to the analogous characteristics of crystalline Si, which also has the diamond lattice and a density of 2.33 g cm^{-3}.

The optical properties of the transient phase were analyzed in the range $F_{eff} > 0.08$ J cm^{-2} [plateau on the $R_{\|}(F_{eff})$ curve in Fig. 1]. In the new structural phase, $R_{\|}$ is not an independent component of R_{1p} in the indicated F_{eff} range, so that its optical properties are unambiguously determined by a pair of values R_{1p} and R_{1s}, with allowance made for the fact that the pumping is provided by both $E_{\perp}$ and $E_{\|}$ components of the *p*-polarized beam. Since the reflectivities $R_{1s}(F_{eff})$ and $R_{1p}(F_{eff})$ very weakly change at $F_{eff} > 0.08$ J cm^{-2}, one can ignore the averaging of the actual R_{2p} and R_{2s} values over the pulse duration, which is caused by the pump-pulse "self-action," and set R_{2p} and R_{2s} equal to R_{1p} and R_{1s}, respectively, for instantaneous $F_{eff}(t)$ values during the pulse. The presence of a plateau in the corresponding curves suggests that the surface layer of the new phase is optically "thick." Consequently, using the plateau values $R_{1p} \approx 0.28 \pm 0.02$ and $R_{1s} \approx 0.40 \pm 0.02$ in Fig. 1 and the Fresnel formulas, one can calculate the optical constants for the new phase. The result is $n(800\text{ nm}) \approx 3.8 \pm 0.1$ and $k(800\text{ nm}) \approx 1.1 \pm 0.6$. The Brewster angle for these values of n and k is considerably larger than 45°; i.e., the reflectivity of the new phase at the normal incidence and $\lambda \approx 800$ nm is approximately the half-sum of $R_{1p} \approx 0.28 \pm 0.02$ and $R_{1s} \approx 0.40 \pm 0.02$, giving 0.34 ± 0.05, in accordance with the calculated 0.37 ± 0.05.

Thus, as was assumed in the analysis of the hypothetical structure of the transient phase, it is "dielectric" at a wavelength of 800 nm and its optical constants, primarily $n(800\text{ nm})$, are close to those of crystalline Si {$n(800\text{ nm}) = 3.7$ and $k(800\text{ nm}) = 0.007$ [15]}. A strong, as compared to Si, linear absorption of the transient phase at a wavelength of 800 nm can be explained by a rather narrow energy gap in the new phase because of large interatomic distances and smaller radius of the carbon atom. At the same time, the optical resistivity of the transient phase is 550 ± 310 μΩ cm at $\lambda \approx 800$ nm, in compliance with the experimental data presented in [13] for the static resistivity of a short-lived laser-induced liquid carbon phase (625 ± 75 μΩ cm) and with the experimental data for the static resistivity of the equilibrium liquid carbon phase (600–900 μΩ cm [23]). The value of 0.37 ± 0.05 calculated for the normal-incidence reflectivity of the transient phase at $\lambda \approx 800$ nm agrees well with the analogous value for the equilibrium liquid carbon phase (0.4 at $\lambda \approx 650$ nm [24]). These facts give evidence for the liquid state of the transient diamondlike phase, as was predicted in recent theoretical works [10, 11].

In [4], the "optical microscopy" method (optical probing of the excited area with a spatial resolution up to 2 μm and a time resolution up to 100 fs) was used to study the reflection of the second harmonic from this graphite sample after it had been exposed to the pump beam. The data obtained indicate that, in the region of laser action beyond the area of sample damage through laser ablation {$F_{abl}(800\text{ nm}) \approx 0.18$ J cm^{-2} for the *p*-polarized pump beam [20]}, no detectable traces of structural transformation occur within several tens of seconds after the action. This suggests that the observed structural transformation is reversible.

4. In summary, the ultrafast (during the 100-fs laser pulse) nonthermal (plasma-induced) structural transformation into a short-lived three-dimensional dielectric (at $\lambda = 800$ nm) phase (presumably diamondlike or liquid) has been observed experimentally in quasi-monocrystalline graphite.

We are grateful to D. von der Linde, K. Sokolowski-Tinten, and V.V. Temnov for assistance in experiments and to the German Academic Exchanges Service for a partial support (fellowship for S.I.K. in 2000).

REFERENCES

1. C. V. Shank, R. Yen, and C. Hirliman, Phys. Rev. Lett. **50**, 454 (1983).
2. H. W. K. Tom, G. D. Aumiller, and C. H. Brito-Cruz, Phys. Rev. Lett. **60**, 1438 (1988).
3. S. V. Govorkov, V. I. Emel'yanov, and I. L. Shumay, Laser Phys. **2**, 77 (1992).
4. K. Sokolowski-Tinten, J. Bialkowski, and D. von der Linde, Phys. Rev. B **51**, 14186 (1995).
5. L. Huang, J. P. Callan, E. N. Glezer, *et al.*, Phys. Rev. Lett. **80**, 185 (1998).
6. J. Larsson, P. A. Heimann, P. J. Schuck, *et al.*, Appl. Phys. A: Mater. Sci. Process. **A66**, 587 (1998).

7. C. W. Siders, A. Cavalleri, K. Sokolowski-Tinten, *et al.*, Science **286**, 1340 (1999).
8. M. B. Agranat, S. I. Anisimov, S. I. Ashitkov, *et al.*, Zh. Éksp. Teor. Fiz. **113**, 2162 (1998) [JETP **86**, 1184 (1998)].
9. M. Zaiser and F. Banhart, Phys. Rev. Lett. **79**, 3680 (1997).
10. J. R. Morris, C. Z. Wang, and K. M. Ho, Phys. Rev. B **52**, 4138 (1995).
11. J. N. Glosli and F. H. Ree, Phys. Rev. Lett. **82**, 4659 (1999).
12. *Femtosecond Laser Pulses: Principles and Experiments*, Ed. by C. Rulliere (Springer-Verlag, Berlin, 1998).
13. D. H. Reitze, H. Ahn, and M. C. Downer, Phys. Rev. B **45**, 2677 (1992).
14. L. G. Johnson and G. Dresselhaus, Phys. Rev. B **7**, 2275 (1973).
15. *Handbook of Optical Constants of Solids II*, Ed. by E. D. Palik (Academic, Orlando, 1991).
16. R. Ahuja, S. Auluck, J. M. Wills, *et al.*, Phys. Rev. B **55**, 4999 (1997).
17. D. H. Reitze, T. R. Zhang, Wm. M. Wood, *et al.*, J. Opt. Soc. Am. B **7**, 84 (1990).
18. V. Heine and J. A. van Vechten, Phys. Rev. B **13**, 1622 (1976).
19. R. Biswas and V. Ambegaokar, Phys. Rev. B **26**, 1980 (1982).
20. K. Sokolowski-Tinten, S. Kudryashov, V. Temnov, *et al.*, in *Proceedings of the 12th International Conference on Ultrafast Phenomena, Charleston, 2000* (Springer-Verlag, Heidelberg, 2001); Springer Ser. Chem. Phys. **66**, 425 (2001).
21. T. Mishina, K. Nitta, and Y. Masumoto, Phys. Rev. B **62**, 2908 (2000).
22. S. Scandolo, M. Bernasconi, G. L. Chiarotti, *et al.*, Phys. Rev. Lett. **74**, 4015 (1995).
23. M. Togaya, Phys. Rev. Lett. **79**, 2474 (1997).
24. A. V. Baitin, A. A. Lebedev, S. V. Romanenko, *et al.*, High Temp.-High Press. **21**, 157 (1990).

Translated by V. Sakun

JETP Letters, Vol. 73, No. 9, 2001, pp. 491–494. Translated from Pis'ma v Zhurnal Éksperimental'noĭ i Teoreticheskoĭ Fiziki, Vol. 73, No. 9, 2001, pp. 556–560.

A New Crystalline Form of Carbon Based on the C_{36} Fullerene: Simulating Its Crystal and Electronic Structure

E. G. Gal'pern[1], A. R. Sabirov[1,2], I. V. Stankevich[1], A. L. Chistyakov[1], and L. A. Chernozatonskiĭ[2]

[1] *Nesmeyanov Institute of Organoelement Compounds, Russian Academy of Sciences, ul. Vavilova 28, Moscow, GSP-1, 117813 Russia*

[2] *Emanuel Institute of Biochemical Physics, Russian Academy of Sciences, ul. Kosygina 4, Moscow, 117977 Russia*

Received March 29, 2001

A new crystalline allotropic form of carbon consisting of covalently bound fullerenes C_{36} of symmetry D_{6h} is suggested. The structure of the unit cell of this compound was simulated. The unit-cell parameters obtained ($a = b = 6.695$ Å and $c = 6.763$ Å) are close to experimental data. The band structure of the spectrum of valence electrons was calculated by the method of crystal orbitals. The bandgap was found to be ~1.9 eV. The energy-band structure of quasi-one-dimensional macromolecules $[C_{36}]_n$ ($n \gg 1$) is discussed depending on the way in which the monomers are bound in them. © *2001 MAIK "Nauka/Interperiodica".*

PACS numbers: 61.48.+c; 71.20.Tx

The discovery and synthesis of macroscopic quantities of fullerenes C_{60} and C_{70} [1, 2] generated a vast flow of interdisciplinary investigations of these novel allotropic forms of carbon. The crystal structures of the fullerenes C_{60} and C_{70} were identified. The most abundant fullerenes C_{60} were found to form molecular close-packed crystals under conventional conditions. Under the effect of visible or ultraviolet light on C_{60}, photopolymerization of these carbon clusters was revealed in 1993 [3], which can be interpreted as a result of the reaction of (2 + 2) cycloaddition widely known in the chemistry of hydrocarbons [4]. Later, new polymeric structures on the basis of C_{60}, both layered (2D) [5, 6] and three-dimensional (3D) [7, 8], were found to be formed under the action of pressure and temperature. Polymerization of other fullerenes was only studied on the example of the C_{70} clusters. In this case, also several polymeric phases were found [9, 10].

The recent works on the synthesis and identification of the structure of smaller fullerenes C_{36} [11, 12] stimulated the appearance of new theoretical investigations of the properties of such clusters and their prognostication (see [12–15] and the references therein). Note that the possibility of the existence of the fullerene C_{36}, whose structure is displayed in Fig. 1 (**1**), was noted in [16, 17]. In these papers, it was also indicated that the cluster C_{36}, because of the stressed state of its carbon skeleton, should be more reactive than the fullerene C_{60}.

In principle, several isomers of the fullerene molecule C_{36} are possible, including a high-symmetry cluster of symmetry D_{6h}. The experimental data speak in favor of the formation of the isomer (D_{6h})-C_{36} [11], although calculations performed in [14, 15] show that an isomer of a lower symmetry D_{2d} should be more stable. It was established in [17] that the ground state of the fullerene C_{36} of symmetry D_{6h} is triplet. Therefore, such an isomer should have an enhanced ability to dimerization and to the formation of polymeric structures. In addition, the symmetry D_{6h} imposes sufficiently hard restrictions not only on the structure of the molecule itself but also on the arrangement of molecules in a covalent crystal that is formed from such fullerenes. Therefore, the (D_{6h})-C_{36} fullerene is of special interest as a possible structural module in simulating new carbon forms.

The (D_{6h})-C_{36} fullerene molecules can form dimers of several types [12, 14–16]. Three of them, **2**–**4**, which are of greatest interest, are shown in Fig. 1. The structure of dimer **2** can be interpreted as a result of the reaction of (2 + 2) cycloaddition. In the region of bonding of neighboring monomers, a four-membered cycle is formed. Dimer **3** can be considered as a result of the reaction of (4 + 4) cycloaddition. In this case, the covalent bonds are formed between 1,1' and 4,4' atoms (Fig. 1). In dimer **4**, a hexagonal prism is formed in the region of linking of two monomers. Note that earlier such a way of bonding of two monomers was suggested in [18] for hypothetical structures consisting of fullerenes C_{60} and later, in [19], an analogous approach was used for the simulation of hypothetical crystals of fullerenes C_{60} of an elongated shape (barrelenes).

The table lists the heats of formation for dimers **2**–**4** obtained by the MNDO/PM3 method (widely applied in calculations of the geometry and electron structure of cage-type molecules and their derivatives) by the optimization of the energy of these systems on the basis

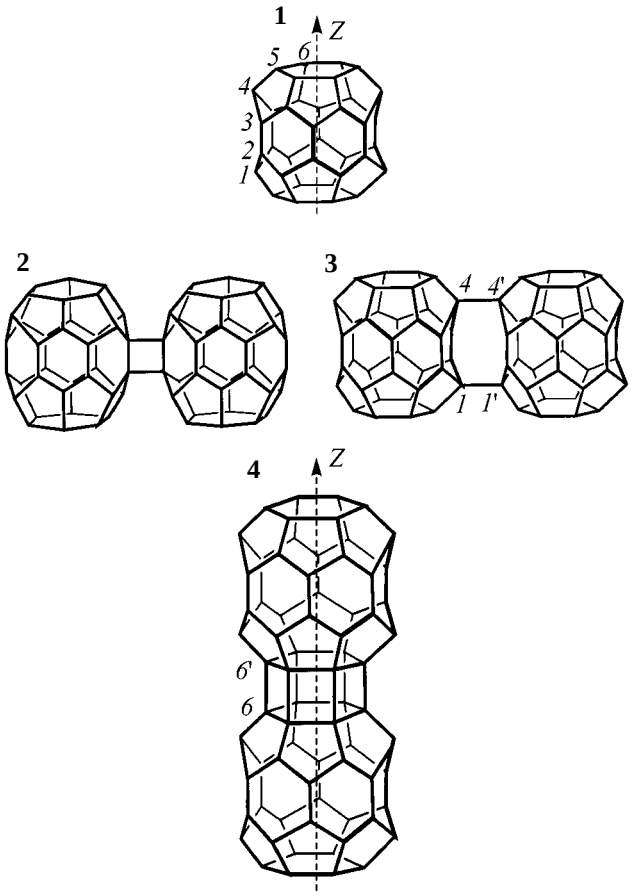

Fig. 1. (D_{6h})-C_{36} molecule (**1**) and dimers (**2**)–(**4**) with three different types of linking (schematic).

of their geometrical parameters. (A GAMESS program packet [20] for a DEC 3000 Alpha AXP 400X workstation was used.) It follows from the table that it is dimer **3** that is most stable. The reaction of the formation of dimer **2** from two monomers is endothermic, and the analogous reaction of formation of dimer **4** is exothermic. Note that the lengths of bonds between the monomers increase monotonically from 1.51 to 1.56 Å in the series of clusters **2**, **3**, **4**. In addition, the valence angle 4'–4–5 in cluster **3** is 134°, whereas in cluster **4** the analogous angle 4–6–6' differs from the classical valence angles (109° and 120°) even more and is equal to 149°. With such a large valence angle, we may expect a noticeable participation of some orbitals of four-coordinated carbon atoms in the interaction with residual conjugated systems of neighboring monomers.

Heats of formation of carbon clusters **1**–**4** found by the MNDO/PM3 method

Multiplicity	Cluster	ΔH_f, kcal/mol	ΔH_f, kcal/mol/C_{36}
1	(D_{6h})-C_{36} (**1**)	840.8	840.8
3	(C_{2v})-C_{36} (**1**)	821.0	821.0
1	$(C_{36})_2$ (**2**)	1724.96	862.4
1	$(C_{36})_2$ (**3**)	1535.8	769.9
1	$(C_{36})_2$ (**4**)	1596.6	798.3

Oligomeric and polymeric structures based on (D_{6h})-C_{36} clusters were discussed in a number of works (see, e.g., [13–15, 21, 22]). In [15, 21], a quasi-two-dimensional layer of covalently bonded (D_{6h})-C_{36} fullerenes was considered. In [14, 22], the so-called clathrate structures were studied, in which the (D_{6h})-C_{36} clusters were used as the main structural units bound with one another by carbon atoms located in intermolecular cavities.

In this work, we suggest a new 3D crystal structure (**5**, Fig. 2) based on the (D_{6h})-C_{36} fullerenes, which is constructed as follows: within one layer, each barrelene is bound with each of six neighbors by two covalent bonds of the same type as in dimer **3**; with the upper and lower neighbors, it forms, as in dimer **4**, hexagonal prisms of sp^3 hybridized atoms. This crystal structure belongs to the space group *P*6/*mmm*; its unit cell contains 36 atoms.

The structure of the unit cell of crystal **5** also was simulated in terms of the MNDO/PM3 quantum-chemical method. Note that this method was earlier used in describing the structure of a quasi-two-dimensional layer of (D_{6h})-C_{36} fullerenes [21]. The parameters of the hexagonal unit cell of crystal **5** and the atomic coordinates were chosen as a result of optimization of the energy of the hydrocarbon molecule $C_{264}H_{132}$ (**6**) of symmetry D_{6h}. The carbon skeleton of molecule **6** consists of a central cluster (D_{6h})-C_{36} and "halves" of eight adjacent clusters C_{36}. This lattice fragment is cut from the structure of crystal **5** by a sphere with its center located in the center of symmetry of the internal cluster C_{36}. The projection of this sphere on the plane $z = 0$ is shown in Fig. 2 by a dotted line. The broken C–C bonds were replaced by C–H bonds. The optimization of the geometry of this giant hydrocarbon molecule consisting of 396 atoms yielded the following coordinates of inequivalent atoms in the unit cell of this crystal: C(1): 0.414, 0.207, 0.099; C(2): 0.384, 0, 0.214; C(3): 0.237, 0, 0.386 (in Fig. 1, these atoms are designated *3*, *4*, and *5*, respectively); and the following parameters of the hexagonal lattice: $a = 6.695$ Å and $c = 6.763$ Å.

The electron spectrum of the crystal structure **5** was calculated by the crystalline orbital method in the valence approximation of the extended Hückel technique (EHT) using the program that is described in [23]. Figure 3 displays the energy band structure of crystal **5** and its Brillouin zone. It is seen from this figure that crystal **5** is a semiconductor with an energy gap of ~1.88 eV.

In contrast to the so-called clathrate structures of symmetry D_{6h} based on the C_{36} clusters [22], which contain additional atoms in the cavities between the

fullerenes, the structure of crystal **5** consists of only molecules C_{36} and is characterized by a semiconductor rather than insulating (7 eV) gap in its electron spectrum. The parameters *a* and *c* of its unit cell turned out to be somewhat nearer to the experimental value 6.68 Å than in the most energetically stable clathrate C_{36+4} [22] (a = 6.91 Å and c = 6.23 Å). Note also that on the surface of this crystal the vertices of the C_{36} molecules ([001] plane) in their structure coincide with the layer of C_{36} molecules linked by (4 + 4) cycles [21] and the lateral faces ([100] plane) coincide with the structure of chains of C_{36} (**7**) linked by hexagonal prisms. Therefore, in the crystal considered, the surface states localized at these structures as at defects (they lie inside the forbidden gap of crystal **5**) can yield a "fine structure" in the electron spectrum, which can be observed by using scanning tunneling spectroscopy of the surface of a nanocrystalline film of C_{36} [12].

Two ways of monomer linking are realized in crystal **5**, which determine the band structure of its electron spectrum. It is, therefore, of interest to compare its spectrum with the spectra of linear macromolecules in which only one type of monomer linking is used: either as in dimer **3** or as in dimer **4**. The first case was studied in [21], where it was shown that the corresponding linear polymer $[C_{36}]_n$ ($n \gg 1$) has a semiconductor spectrum with an energy gap of ~1 eV. The quasi-one-dimensional macromolecule **7** with intermonomer bonds of the second type (Fig. 1, **4**) was not investigated earlier. The structure of the repeating unit of the linear polymer **7** was determined based on the calculation of the trimer $(C_{36})_3$. The results of the calculations of the electron spectrum of this macromolecule are given in Fig. 4. It is seen that there is a sufficiently narrow energy gap (0.06 eV) in the spectrum of the macromolecule **7**. Such a character of the spectrum appears to be related to the anomalously large values of one of the valence angles (reaching 150°) of each of the four-coordinated carbon atoms. The macromolecule **7** can be regarded as a (6.0) nanotube with defects that lead to the formation of a corrugated structure, which nevertheless exerts no significant effect on the conducting properties of the molecule.

We performed a simulation of the geometric and electronic structures of the new crystal allotropic form of carbon of symmetry D_{6h} consisting of 3D polymerized barrelenes (D_{6h})-C_{36}. The parameters of the unit cell of this crystal agree well with the experimental data [11, 12]. These data correspond to a semiconductor character of the electron spectrum of the structure considered. Because of the presence of one-third of sp^2 hybridized atoms in crystal (**1**), it should be expected that the structure considered will have a sufficiently large hardness, similar to the structures of 3D polymeric fullerenes C_{60} [7, 8]. In future, we plan to calculate the phonon spectrum of the C_{36} crystal and estimate the bulk elasticity modulus and the modes that are active in Raman spectra, as well as its X-ray diffraction

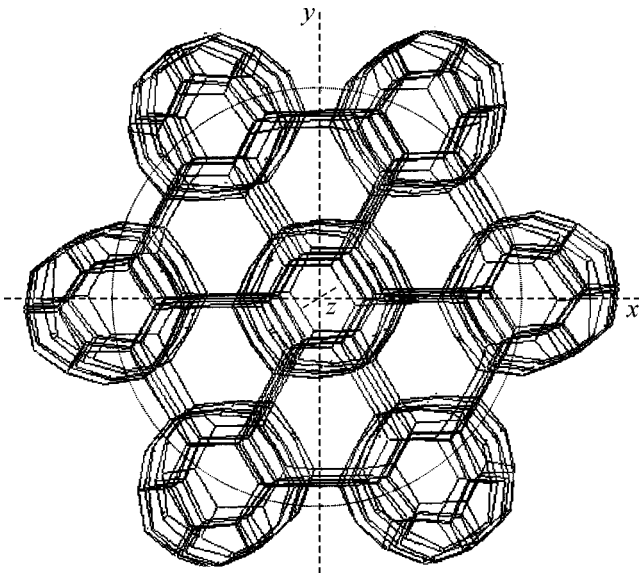

Fig. 2. Crystal (**5**) of hexagonal symmetry D_{6h} consisting of 3D polymerized fullerenes (D_{6h})-C_{36}. Dotted line shows the [001] projection of the sphere (with the center located at the center of symmetry of the internal cluster C_{36}) that restricts a crystal lattice fragment of 264 carbon atoms. This fragment was used for calculating unit-cell parameters of crystal (**5**). The values obtained are a = 6.695 and c = 6.763 Å.

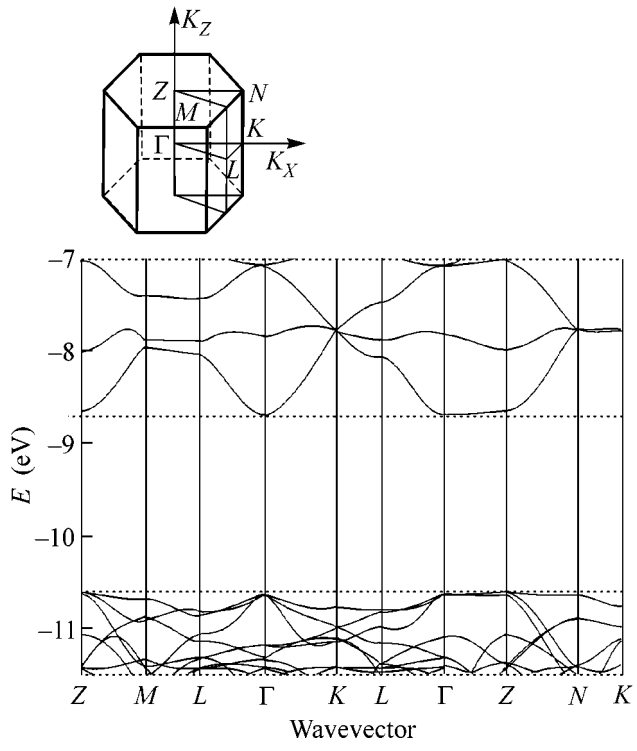

Fig. 3. Energy band structure of crystal (**5**) of hexagonal symmetry D_{6h} consisting of 3D polymerized (D_{6h})-C_{36} clusters. In the top portion, the first Brillouin zone is shown.

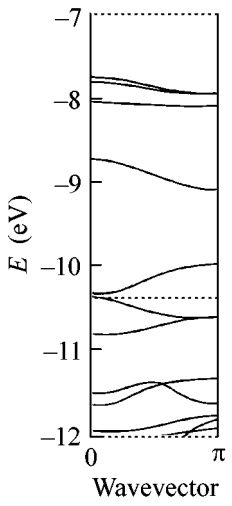

Fig. 4. Energy band structure of quasi-one-dimensional linear polymer **7** in which the bonds between neighboring monomers (D_{6h})-C_{36} form a hexagonal prism.

pattern, to more reliably identify its properties in experiment.

Note that the existence of the cluster C_{36} obtained by the authors of [11] was confirmed recently by high-resolution electron microscopy [24].

ACKNOWLEDGMENTS

This work was supported in part by the Russian Foundation for Basic Research and the Russian Research Program "Physics of Condensed Media," direction "Fullerenes and Atomic Clusters," INTAS project no. 00-237.

REFERENCES

1. H. W. Kroto, J. R. Heath, S. C. O'Brienet, *et al.*, Nature **318**, 162 (1985).
2. W. Krätchmer, L. D. Lamb, K. Fostiropoulos, and D. R. Huffman, Nature **347**, 354 (1990).
3. A. M. Rao, P. Zhou, K.-A. Wang, *et al.*, Science **259**, 955 (1993).
4. R. B. Woodward and R. Hoffmann, *The Conservation of Orbital Symmetry* (Academic, New York, 1970).
5. Y. Ivasa, T. Arima, R. M. Fleming, *et al.*, Science **264**, 1570 (1994).
6. M. Nuniez-Regueiro, L. Marques, J.-L. Hodeau, *et al.*, Phys. Rev. Lett. **74**, 278 (1995).
7. V. D. Blank, S. G. Buga, N. R. Serebrynaya, *et al.*, Phys. Lett. A **220**, 149 (1996).
8. L. A. Chernozatonskii, N. R. Serebrynaya, and B. N. Mavrin, Chem. Phys. Lett. **316**, 199 (2000).
9. A. M. Rao, M. Menon, K.-A. Wang, *et al.*, Chem. Phys. Lett. **224**, 106 (1994).
10. V. D. Blank, N. R. Serebrynaya, G. A. Dubitskii, *et al.*, Phys. Lett. A **248**, 415 (1998).
11. C. Piskoti, J. Yarger, and A. Zettl, Nature **393**, 771 (1998).
12. P. G. Collins, J. C. Grossman, M. Côté, *et al.*, Phys. Rev. Lett. **82**, 165 (1999).
13. J. C. Grossman, M. Côté, S. Louie, and M. L. Cohen, Chem. Phys. Lett. **284**, 344 (1998).
14. M. Menon and E. Richter, Phys. Rev. B **60**, 13322 (1999).
15. P. W. Fowler, T. Heine, K. M. Rogers, *et al.*, Chem. Phys. Lett. **300**, 369 (1999).
16. L. A. Chernozatonskii, Phys. Lett. A **55A**, 483 (1991).
17. E. G. Gal'pern, I. V. Stankevich, L. A. Chernozatonskiĭ, and A. L. Chistyakov, Pis'ma Zh. Éksp. Teor. Fiz. **55**, 483 (1992) [JETP Lett. **55**, 495 (1992)].
18. M. O'Keeffe, Nature **352**, 674 (1991).
19. L. A. Chernozatonskii, Chem. Phys. Lett. **209**, 229 (1993).
20. M. W. Schmidt, K. K. Baldridge, J. A. Boatz, *et al.*, J. Comput. Chem. **14**, 1347 (1993).
21. E. G. Gal'pern, I. V. Stankevich, A. L. Chistyakov, and L. A. Chernozatonskii, J. Mol. Graf. Model. (2001) (in press).
22. M. Menon, E. Richter, and L. Chernozatonskii, Phys. Rev. B **62**, 15420 (2000).
23. D. A. Bochvar, E. G. Gal'pern, and I. V. Stankevich, Zh. Strukt. Khim. **29**, 26 (1988).
24. T. Oku, T. Hirano, M. Kuno, *et al.*, Mater. Sci. Eng. B **B74**, 206 (2000).

Translated by S. Gorin

JETP Letters, Vol. 73, No. 9, 2001, pp. 495–497. Translated from Pis'ma v Zhurnal Éksperimental'noĭ i Teoreticheskoĭ Fiziki, Vol. 73, No. 9, 2001, pp. 561–564.

Elastic State of Stress in Narrow-Gap Semiconductors: A Fundamental Possibility to Increase the Quantum Yield of Infrared Radiation

S. G. Gassan-Zade*, S. V. Staryĭ, M. V. Strikha, G. A. Shepel'skiĭ, and V. A. Boĭko

Institute of Semiconductor Physics, National Academy of Sciences of Ukraine, Kiev, 01650 Ukraine

** e-mail: gassan@class.semicond.kiev.ua*

Received December 15, 2000; in final form, March 29, 2001

In a narrow-gap semiconductor with a direct band gap, an elastic state of stress provides the possibility to considerably reduce the collisional interband recombination because of the transformation of the valence band. As a result, the quantum yield of infrared radiation in the interband transition region increases drastically. The experimental results are obtained for InSb crystals. © *2001 MAIK "Nauka/Interperiodica".*

PACS numbers: 71.28.+d; 73.61.Ey; 78.66.Fd

It is common knowledge that the main obstacle to obtaining efficient radiators on the basis of narrow-gap semiconductors with direct band gaps is the collisional interband recombination (the Auger recombination). This important type of radiationless recombination is inherent in semiconductors, because its characteristics are determined by the parameters of the intrinsic energy-band spectrum of a semiconductor rather than by the presence of impurity or defect energy levels in the band gap. For example, in InSb, even at low excitation levels, the Auger recombination becomes significant at $T \geq 250$ K [1], i.e., in the intrinsic conduction region, whereas, in $Cd_xHg_{1-x}Te$ with $x = 0.20$, it already begins to dominate in the impurity conduction region ($T \geq 77$ K) [2].

In the case of a high-level excitation, when the nonequilibrium carrier concentration far exceeds the equilibrium concentration, i.e., $\delta n = \delta p \gg n_0, p_0$, the role of the Auger recombination drastically increases. This is related to the steeper (cubic) concentration dependence of the Auger recombination rate, as compared to the quadratic dependence for the radiative recombination rate. The latter fact imposes fundamental limitations on the limiting theoretical values of the parameters of infrared radiators.

This paper shows that, by producing an elastic state of stress in narrow-gap semiconductors, it is possible to considerably increase the quantum yield of infrared radiation in the interband transition region. Such an increase is achieved as a result of the suppression of the Auger recombination rate because of the radical transformation of the valence band under a uniaxial elastic stress.

In the presence of a uniaxial stress (below, we consider a compression along the [001] crystal axis; for other axes, one obtains similar results), the degeneracy of the valence band at the point $k = 0$ is eliminated, and the light and heavy hole states are mixed [3–5]. In this case, they are conveniently described by the subbands V_+ and V_-. Between the vertices of the subbands, an energy gap ε_0 is formed. According to the Bir and Pikus model [6], this energy gap is proportional to the compression P and can be represented in the form $\varepsilon_0 = 2|b|(S_{11} - S_{12})P$, where b is the deformation potential constant and S_{11} and S_{12} are the components of the elastic compliance tensor. We note that, in this case, the band gap (and, thus, the long-wavelength limit of the interband radiation) varies insignificantly (at $P = 4$ kbar, the variation of ε_g in InSb does not exceed 3 meV). This is related to the competition between two mechanisms: an increase in the energy gap because of the hydrostatic component of the uniaxial deformation and a decrease in this gap by $1/2\varepsilon_0(P)$ because of the upward motion of the V_+ subband. As a result, we obtain $\tilde{\varepsilon}_g = \varepsilon_g + \zeta/3P - 1/2\varepsilon_0(P)$, where ζ is the deformation potential constant for hydrostatic compression. The results of calculations agree well with the experimental data obtained from the polarization-spectral measurements of the photocurrent in uniaxially stressed InSb [7].

As one can see from the schematic diagram shown in Fig. 1, the quantity ε_0 reaches considerable values even at small values of P. Such a strong effect of deformation on the band structure of narrow-gap semiconductors is explained by the large effective mass ratio of light and heavy holes in the initial crystal, as compared to conventional semiconductors (in InSb, $m_h/m_l = 20$ and, in $Cd_xHg_{1-x}Te$ with $x = 0.20$, $m_h/m_l = 50$). In the elastic state of stress, the effective masses of holes become anisotropic and are described by the expressions $m_0/(\gamma_1 \pm 2\gamma)$ for the longitudinal and $m_0/(\gamma_1\gamma)$ for

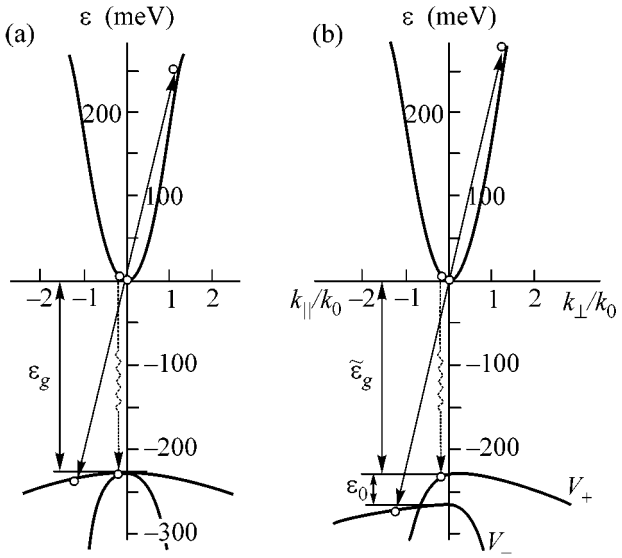

Fig. 1. Transformation of the energy spectrum of InSb under a uniaxial stress P = (a) 0 and (b) 4 kbar. The arrows indicate the interband recombination transitions: the Auger (the solid lines) and the radiative (the dotted lines) transitions; $k_0 \approx 4 \times 10^{-6}$ cm^{-1}.

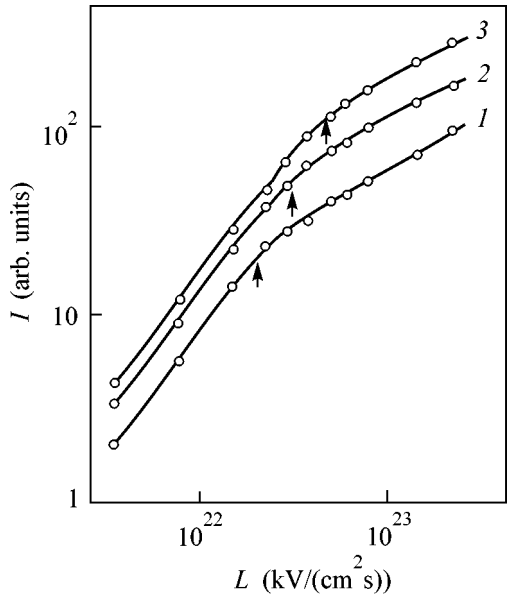

Fig. 2. Dependences of the recombination radiation intensity of *n*-InSb on the excitation level L for P = (*1*) 0, (*2*) 2.6, and (*3*) 4.5 kbar.

the transverse directions relative to the compression axis (here, γ_1 and γ are the Luttinger parameters).

The main result produced by the valence band transformation under uniaxial stress, which leads to a change in the interband recombination rate, consists in a considerable decrease in the average effective hole mass relative to the hole mass m_h in the initial crystal. In such a situation, most of the holes are thermalized in the small momentum region, and the direct radiative transitions of electrons from the *c* band become more efficient. The latter fact must lead to an increase in the radiative recombination rate with increasing P. At the same time, in the absence of deformation, the high rate of collisional interband recombination is determined by the low energy thresholds of the Auger transitions because of the small value of the ratio $m_c/m_h \ll 1$ [8] (m_c is the effective electron mass). A decrease in the effective masses of holes under an elastic stress leads to a sharp increase in these thresholds. Therefore, the Auger recombination rate decreases substantially (unlike the radiative recombination rate).

The deformation dependences of the quantum yield of radiation were studied on *n*-InSb crystals whose parameters at T = 77 K were as follows: $n = (2–4) \times 10^{13}$ cm^{-3} and $\mu_n = (3–5) \times 10^5$ cm^2/(V s). The sample to be studied was placed along with the uniaxial compression device in a cryostat with liquid nitrogen. The sample was excited by a neodymium laser in a pulsed mode of operation. The radiation was detected by a cooled Ge(Au) detector.

Figure 2 presents the dependences of the radiation intensity I of an *n*-InSb sample on the excitation level L for different values of the elastic stress P. The curves exhibit characteristic breakpoints, which testify to a change in the dominant recombination mechanism. In the interval $L = 5 \times 10^{22}–3 \times 10^{23}$ kV/(cm^2 s), the slope of the curves is about 0.5 on the logarithmic scale, and at smaller values of L, it is within 1.5–1.6 for different samples. One can assume that, at high excitation levels, the Auger recombination should dominate.

By solving the continuity equation for a nonuniform excitation of carriers by strongly absorbed light with the corresponding boundary condition at the sample surface (a small surface recombination rate), one can obtain an expression for the intensity of the interband recombination radiation as a function of the external excitation [9, 10]. For relatively low excitation levels (for InSb, $\delta n < 10^{17}$ cm^{-3}), the calculation yields the dependence $I \sim L^{1.7}$, whereas, for higher excitation levels, we have $I \sim L^{0.5}$. These relations fit the experimental data with fair accuracy. We note that the power laws obtained from the calculations are governed by the recombination terms that describe different recombination mechanisms in the aforementioned equation. The inclusion of the carrier degeneracy somewhat modifies the form of the dependences $I(L)$, as compared to the dependences obtained in [10].

Thus, the parts of the curves with the slope 0.5 in Fig. 2 can be associated with the dominance of the Auger interband recombination. The fact that the breakpoint in the curves moves to higher values of L with increasing P testifies to a decrease in the Auger recombination rate in the elastic state of stress.

The data shown in Fig. 3 seem to be of most interest. This figure presents the deformation dependences of the interband radiation intensity for InSb crystals at dif-

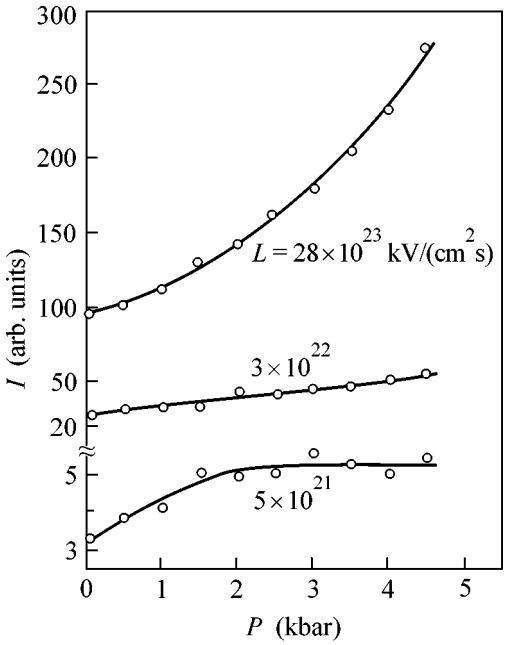

Fig. 3. Deformation dependences of the interband radiation intensity of an *n*-InSb sample for different excitation levels *L*.

ferent excitation levels. One can notice the qualitative difference between curves *1–3*. At small values of *L* (curve *1*), the dependence *I*(*P*) tends to saturation already at $P \geq 2$ kbar, whereas, at the maximal excitation levels (curve *3*), a superlinear dependence is observed. In this case, the intensity *I* increases several times relative to the initial value. We note that the behavior of the curves *I*(*P*) at high values of *L* (curve *3*) proved to be identical for all InSb samples studied. This means that the decisive factor is not the initial crystal parameters, but the high density of nonequilibrium charge carriers, which provides the dominance of the Auger recombination. At the same time, the form of curve *1* (qualitatively, curves *1* obtained for different samples were also similar to each other) points to an insignificantly small contribution of the Auger transitions to the resulting recombination in the initial crystal ($P = 0$) at low excitation levels. In this case, the growth of *I* with increasing *P* is determined by virtually nothing but the increase in the rate of direct interband radiative transitions. Curve *2* should be attributed to an intermediate case. The theoretical estimates (the detailed calculations will be published later) agree well with the experimental results presented above.

From the form of curve *3*, we can also conclude that the value $P = 4.5$ kbar achieved in the experiment does not exhaust the possibilities of the elastic state of stress from the point of view of increasing the quantum efficiency of interband radiation in InSb. According to the literature, elastic stresses in InSb can reach 5–5.5 kbar [5, 11] and, in $Cd_xHg_{1-x}Te$, they can reach 3.5–4.2 kbar [5, 12].

Thus, the experimental dependences *I*(*P*) presented in this paper testify to a suppression of the Auger interband radiationless recombination by an elastic stress and to a substantial increase in the quantum yield of infrared radiation due to this mechanism.

In closing, we note that the necessary elastic state of stress can easily be implemented in a semiconductor structure. For example, it can result from the difference between the lattice constants of the substrate material and the active layer of the main material. Another possibility is to use the difference between the linear expansion coefficients of materials.

We are grateful to F.T. Vas'ko for useful discussions.

REFERENCES

1. R. N. Zitter, A. S. Strauss, and A. E. Attard, Phys. Rev. **115**, 266 (1959).
2. N. S. Baryshev, V. L. Gel'mont, and M. I. Ibragimova, Fiz. Tekh. Poluprovodn. (Leningrad) **24**, 209 (1990) [Sov. Phys. Semicond. **24**, 127 (1990)].
3. F. T. Vas'ko, S. G. Gasan-zade, M. V. Strikha, and G. A. Shepel'skiĭ, Pis'ma Zh. Éksp. Teor. Fiz. **50**, 287 (1989) [JETP Lett. **50**, 318 (1989)].
4. S. G. Gasan-zade and G. A. Shepel'skiĭ, Fiz. Tekh. Poluprovodn. (St. Petersburg) **27**, 733 (1993) [Semiconductors **27**, 401 (1993)].
5. A. V. Germanenko and G. M. Minkov, Phys. Status Solidi B **184**, 9 (1994).
6. G. L. Bir and G. E. Pikus, *Symmetry and Stain-Induced Effects in Semiconductors* (Nauka, Moscow, 1972; Wiley, New York, 1975).
7. F. T. Vas'ko, S. G. Gasan-zade, M. V. Strikha, and G. A. Shepel'skiĭ, Fiz. Tekh. Poluprovodn. (St. Petersburg) **29**, 708 (1995) [Semiconductors **29**, 368 (1995)].
8. B. L. Gel'mont, Z. I. Sokolova, and I. N. Yassievich, Fiz. Tekh. Poluprovodn. (Leningrad) **16**, 592 (1982) [Sov. Phys. Semicond. **16**, 1067 (1982)].
9. V. K. Malyutenko, S. S. Bolgov, V. I. Pipa, and V. I. Chaĭkin, Fiz. Tekh. Poluprovodn. (Leningrad) **14**, 781 (1980) [Sov. Phys. Semicond. **14**, 457 (1980)].
10. S. S. Bolgov and L. L. Fedorenko, Fiz. Tekh. Poluprovodn. (Leningrad) **21**, 1188 (1987) [Sov. Phys. Semicond. **21**, 722 (1987)].
11. R. Bishof, I. Maran, and W. Seidenbusch, Infrared Phys. **34**, 345 (1993).
12. F. T. Vas'ko, S. G. Gasan-zade, V. A. Romaka, and G. A. Shepel'skiĭ, Pis'ma Zh. Éksp. Teor. Fiz. **41**, 100 (1985) [JETP Lett. **41**, 120 (1985)].

Translated by E. Golyamina

JETP Letters, Vol. 73, No. 9, 2001, pp. 498–502. Translated from Pis'ma v Zhurnal Éksperimental'noĭ i Teoreticheskoĭ Fiziki, Vol. 73, No. 9, 2001, pp. 565–569.

Reduction of the *XXZ* Model with Twisted Boundary Conditions

A. A. Belavin* and S. Yu. Gubanov**

Landau Institute for Theoretical Physics, Russian Academy of Sciences, Chernogolovka, Moscow region, 142432 Russia

** e-mail: belavin@itp.ac.ru*

*** e-mail: gubanov@itp.ac.ru*

Received March 29, 2001

The *XXZ* model with twisted boundary conditions is considered. The method of energy spectrum calculation based on the functional equation for the transfer matrix is analyzed. The Hamiltonian eigenvalues are obtained in an explicit form. © *2001 MAIK "Nauka/Interperiodica".*

PACS numbers: 05.50.+q; 75.10.Jm

Introduction. The model of a chain of two-level atoms with nearest-neighbor interactions [1] was proposed by Heisenberg as early as 1926 and now is one of the simplest models describing one-dimensional crystal. The Hamiltonian of the anisotropic Heisenberg–Ising model (*XXZ* model) has the form

$$H_{XXZ} = 2J\sum_{n=1}^{N}(\sigma_n^x\sigma_{n+1}^x + \sigma_n^y\sigma_{n+1}^y + \Delta\sigma_n^z\sigma_{n+1}^z), \quad (1)$$

where J is the Slater exchange integral [in our case, $\Delta = \frac{1}{2}(q + q^{-1}) \equiv \cos(\eta)$, where $q = e^{i\eta}$]. In 1931, Bethe suggested the method for calculating the eigenvectors and eigenvalues of this Hamiltonian and, therefore, for solving the problem. To do this, one has to solve the transcendental Bethe equations. In this work, we demonstrate how one can obtain the explicit expression for the energy spectrum in the case of generalized periodic boundary conditions without solving the transcendental equations of the Bethe ansatz.

The *twisted* boundary conditions read

$$\sigma_{N+1}^{\pm} = q^{\pm 2\beta}\sigma_1^{\pm}, \quad \sigma_{N+1}^z = \sigma_1^z, \quad (2)$$

where $\sigma^{\pm} = \frac{1}{2}(\sigma^x \pm i\sigma^y)$. The spin projection onto the z axis is conserved: $[S^z, H_{XXZ}] = 0$, where $S^z = \frac{1}{2}\sigma_1^z + \ldots + \frac{1}{2}\sigma_N^z$. The energies of the chains with different twist parameters are related to each other as follows [2]: the energy spectrum of a chain with twist parameter β from the $S^z = \beta - 1$ sector contains the energy spectrum of a chain with twist parameter $\beta - n$ from the $S^z = \beta - 1 + n$ sector, where n is an integer,

$$E^{(\beta)}_{S^z=\beta-1} = E^{(\beta-n)}_{S^z=\beta-1+n}. \quad (3)$$

This is so because of the quantum group symmetry $U_q(sl(2))$. We say "spectrum contains" because the sector $S^z = \beta - 1$ contains a smaller number of vectors than does the sector $S^z = \beta - 1 + n$.

The *XXZ* model is related to a two-dimensional classical statistical six-vertex lattice model (ice model). Ice H_2O crystal, PO_4H_2K ferroelectric, and $PO_4H_2NH_4$ antiferroelectric are among the physical systems obeying this model. It represents a two-dimensional idealized crystal with "hydrogen-bonded" atomic pairs or neighboring radicals. No more than two H^+ ions are located near each crystal site. In ice crystal, each oxygen atom forms four bonds with the neighboring oxygen atoms that are arranged in the vertices of a tetrahedron, giving six configurations relative to the lattice (Onsager and Dupuis, 1960). The Hamiltonian of the *XXZ* model and the transfer matrix $\hat{t}_{1/2}(u)$ of the six-vertex model are related to each other by the following equation:

$$H_{XXZ} = -\frac{N}{2}\cos(\eta) + \sin(\eta)\frac{d}{du}\log\hat{t}_{1/2}(u)|_{u=0}. \quad (4)$$

The Hamiltonian and the transfer matrix commute with each other and, hence, have the same set of eigenvectors. In this work, we will first of all obtain the transfer matrix eigenvalues and then calculate the energy spectrum using Eq. (4).

0021-3640/01/7309-0498$21.00

There is an infinite family of transfer matrices $t_j(u)$ with $j = 0, \frac{1}{2}, 1, \frac{3}{2}, \ldots$. They commute with each other and satisfy the following infinite system of recurrence functional fusion relations [3–5]:

$$\begin{aligned}\hat{t}_{1/2}(u-(j+1/2)\eta)\hat{t}_j(u) &= t_0(u-(j+1)\eta)\hat{t}_{j-1/2}(u+\eta/2)\\ &+ t_0(u-j\eta)\hat{t}_{j+1/2}(u-\eta/2),\end{aligned} \tag{5}$$

where $t_0(u) = \sin^N(u + \eta/2)$. In this work, we prove that, for the anisotropy parameter equal to a root of unity, $q^{p+1} = -1$, the transfer matrix with spin $j = p/2$ has zero eigenvalues for the Bethe eigenvectors if the twist parameter β and the sector $S^z = s$ satisfy certain conditions. If the eigenvalue of $t_{p/2}(u)$ becomes zero, the infinite system of functional fusion relations (5) becomes truncated and transforms to *a functional equation* for $t_{1/2}(u)$. By solving this equation, we find $t_{1/2}(u)$ and the corresponding energy value using Eq. (4). Denote the whole set of Bethe eigenvectors for which $t_{p/2}(u)$ has zero eigenvalues by the symbol V_p. We will call the projection of the *XXZ* model on the V_p space *the reduction of the XXZ model*. It was shown in [2] that the thermodynamic limit of such a reduced *XXZ* model coincides with the minimal model of the conformal field theory with central charge $c = 1 - 6/p(p + 1)$, rendering this treatment particularly interesting. The energy spectrum of the reduced *XXZ* model can be calculated by solving the functional equations for the transfer matrix of a six-vertex model.

Zero eigenvalues. Let us consider the Baxter's *T–Q* equations [$t(u) \equiv t_{1/2}(u)$]

$$\begin{aligned}t(u)Q(u) &= q^{-\beta}t_0(u+\eta/2)Q(u-\eta)\\ &+ q^{\beta}t_0(u-\eta/2)Q(u+\eta),\end{aligned} \tag{6}$$

where $t_0(u) = \sin^N(u + \eta/2)$. According to [6], this equation can be considered as a discrete version of the second-order differential equation [7]. In this case, in addition to the $Q(u)$ function, it must have the second linearly independent solution $P(u)$ with the same eigenvalue of the transfer matrix $t(u)$. The transfer matrix eigenvalues can be expressed through the eigenvalues of the Baxter operator $Q(u)$ and the $P(u)$ operator as

$$\begin{aligned}t_j(u) &= q^{(2j-1)\beta}f(u-(j-1/2)\eta)\\ &\times[Q(u-(j+1/2)\eta)P(u+(j+1/2)\eta)\\ &- Q(u+(j+1/2)\eta)P(u-(j+1/2)\eta)],\end{aligned} \tag{7}$$

where $f(u)$ is a quasiperiodic function,

$$f(u+\eta) = q^{-2\beta}f(u), \tag{8}$$

which is introduced for the sake of convenience [the function $\tilde{P}(u) = f(u)P(u)$ may also be introduced].

Let us consider the case for which the anisotropy parameter is a root of unity, $q^{p+1} = -1$, where p is a certain positive number. For the transfer matrix in the $j = p/2$ spin representation, one has

$$\begin{aligned}t_{p/2}(u+\pi/2) &= (-1)^{\beta}f(u)[P(u+\pi)Q(u) - P(u)Q(u+\pi)],\end{aligned} \tag{9}$$

whence it immediately follows that, if the functions $Q(u)$ and $P(u)$ satisfy relations

$$\frac{P(u+\pi)}{P(u)} = \frac{Q(u+\pi)}{Q(u)}, \tag{10}$$

then the eigenvalue of the transfer matrix $t_{p/2}(u)$ becomes zero.

We can express the function $P(u)$ through $Q(u)$: namely, after decomposing

$$\begin{aligned}\frac{t_0(u)}{Q(u+\eta/2)Q(u-\eta/2)} &= R(u) + q^{\beta}\frac{A(u+\eta/2)}{Q(u+\eta/2)} - q^{-\beta}\frac{A(u-\eta/2)}{Q(u-\eta/2)},\end{aligned} \tag{11}$$

where $R(u)$ is a trigonometric polynomial of degree $N - 2n$, which is uniquely defined by the known trigonometric polynomials $t_0(u)$ and $Q(u)$; accordingly, the degree of $A(u)$ is less than n (in the sector of interest, the integer n is related to the $S^z = s$ eigenvalue as $n = N/2 - s$). Let us now decompose

$$R(u) = q^{\beta}F(u+\eta/2) - q^{-\beta}F(u-\eta/2). \tag{12}$$

One can readily see that the function $P(u)$ is determined by the expression

$$P(u) = \frac{1}{f(u)}(Q(u)F(u) + A(u)). \tag{13}$$

An analysis of this expression leads to the following limitations on the twist parameter β in the boundary conditions of the *XXZ* model:

$$(-1)^{2\beta} = (-1)^N. \tag{14}$$

If the spin-chain length is *even*, then the β number must be *integer*, and if the length is *odd*, it must be *half-integer*. The system of functional relations is not truncated for the other β values. The condition for decomposing the $R(u)$ function into $F(u)$ (12), where the function $F(u)$ behaves exactly as $R(u)$ upon shifting $u \longrightarrow u + \pi$, is expressed by the inequality

$$\prod_{m=-s}^{+s}\sin\left(\pi\frac{m+\beta}{p+1}\right) \neq 0 \tag{15}$$

[because this product appears in the denominator of $F(u)$]. The m variable runs from $-s$ to $+s$ over either integer or half-integer values. Depending on the even-

ness of the chain length, the β and s numbers are both either integer or half-integer, so that their sum or difference is an integer number. Condition (15) is satisfied if

$$|s| < \min(\beta, p+1-\beta) \mod(p+1). \tag{16}$$

Therefore, when analyzing the second linearly independent Baxter's solution, one arrives at the following conclusion: *for the anisotropy parameter equal to a root of unity, $q^{p+1} = -1$, the transfer matrix for spin $j = p/2$ has zero eigenvalues in the sector $S^z = s$ if conditions (14) and (16) are fulfilled.*

Algebraic structure. We proved in the preceding section that, for the vectors subjected to certain restrictions, the chain of functional relations (5) breaks and transforms into a closed system of eigenvalue equations for the transfer matrix $t_{1/2}(u)$. In this section, we list all vectors satisfying this condition in the state space of the model.

It was pointed out in the Introduction that relationship (3) between the energies of the chains differing in twist parameter β is due to the presence of quantum group symmetry $U_q(sl(2))$. The S^z, X, and X^t operators are generators of this symmetry, where

$$X = \sum_{n=1}^{N} q^{\frac{1}{2}(\sigma_1^z + \ldots + \sigma_{n-1}^z)} \sigma_n^+ q^{-\frac{1}{2}(\sigma_{n+1}^z + \ldots + \sigma_N^z)} \tag{17}$$

(one can readily verify that $X^{p+1} = 0$ for $q^{p+1} = -1$). When acting on a vector from the sector $S^z = s$, the operator X transforms it into a vector from the $S^z = s+1$ sector: $[S^z, X] = X$. The action of this operator on the Hamiltonian gives

$$XH_{XXZ}^{(\beta)} - H_{XXZ}^{(\beta-1)}X = (\ldots)(1 - q^{2(S^z - \beta + 1)}), \tag{18}$$

which proves Eq. (3).

The transfer matrix of the six-vertex model, which is associated with the Hamiltonian of the *XXZ* model, is expressed through the diagonal elements $L_k^n(u)$ of the monodromy matrix:

$$t_j(u) = \sum_{n=1}^{2j+1} q^{-2\beta(j+1-n)} L_n^n(u). \tag{19}$$

Making use of the Yang–Baxter equation, one can obtain, exactly as was done in [8], the commutation relations between the matrix elements of the monodromy matrix and the S^z and X operators:

$$\begin{aligned} q^{S^z} L_k^n &= q^{n-k} L_k^n q^{S^z}, \\ XL_k^n(u) &= q^{2(j+1)-n-k} L_k^n(u) X \\ &+ \omega_{k-1} e^{+iu} q^{j+1-n} L_{k-1}^n(u) q^{-S^z} \\ &- \omega_n e^{+iu} q^{j+2-k} L_k^{n+1}(u) q^{+S^z}, \end{aligned} \tag{20}$$

where $\omega_n = \sqrt{[n]_q[2j+1-n]_q}$ and the standard notation $[x]_q = (q^x - q^{-x})/(q - q^{-1})$ is used. Commutation relations (20) allow one to express the transfer matrix through the X operator. Below, a nontrivial formula, which we derived for the transfer matrix with spin $j = p/2$ in the sector $S^z = s$, is presented without proof:

$$t_{p/2}(u) = \sum_{r,k=0}^{p} X^r \hat{M}_{rk} X^k. \tag{21}$$

In this formula, the $\hat{M}_{rk}$ operator is

$$\begin{aligned} \hat{M}_{rk} &= (-1)^r \omega^{-1} e^{-ipu} q^{-2s - (2\beta+1-r-k)p/2 - 2k} \\ &\times \sum_{n=0}^{p} q^{(2(\beta-s)+r-k)n} C_r^n C_k^{p-n} \\ &\times \sum_{m=0}^{p-r-k} \lambda_{m,\,p-r-k}(L_{p/2})(u)^1_{p-r-k-m} X^{p-r-k-m}. \end{aligned} \tag{22}$$

The following notation is introduced: $\omega = \prod_{k=1}^{2j} \omega_k$, C_n^N are the q-binomial coefficients

$$\begin{aligned} C_n^N &= \frac{1}{[n]_q!}[N]_q[N-1]_q \ldots [N+1-n]_q \\ &= \frac{[N]_q!}{[n]_q![N-n]_q!}, \end{aligned}$$

and $\lambda_{m,\,p-r-k}$ are defined as

$$\begin{aligned} &\lambda_{m,\,m'} \\ &= e^{imu} q^{p/2+1+s+(m'-m)(m'+s-3p/2-1)} C_m^{m'} \prod_{l=1}^{m} \omega_{m'-l}. \end{aligned}$$

One can see from Eq. (21) that the transfer matrix $t_{p/2}(u)$ is expressed through the sum of monomials of the $X^r \hat{M}_{rk} X^k$ type. Let us find for which integer numbers r and k the $\hat{M}_{rk}$ operator is nonzero if $q^{p+1} = -1$. The operator $\hat{M}_{rk}$ is proportional to the following sum of the q-binomial coefficients:

$$f_{rk} \equiv \sum_{n=0}^{p} C_r^n C_k^{p-n} q^{n(2l+r-k)}, \tag{23}$$

where $l = \beta - s$. Unfortunately, we failed to obtain closed expression for the f_{rk} coefficients. For this reason, we analyzed the sum in Eq. (23) numerically. We checked numerically the hypothesis that for $q^{p+1} = -1$ the coefficients f_{rk} are nonzero only in the following closed domain: $r + k \le p$ and either $r > p - l$ or $k > l - 1$.

Consequently, the transfer matrix $t_{p/2}(u)$ is representable as

$$t_{p/2}(u) = X^{p+1-l}(\ldots) + (\ldots)X^l, \tag{24}$$

and, hence, becomes zero on the cohomologies

$$V_{p,l} = \mathrm{Ker}\, X^l / \mathrm{Im}\, X^{p+1-l}. \tag{25}$$

Hence, zero eigenvalues exist for those eigenvectors v from the sector $S^z = s$ which, first, vanish under the action of the operator X^l,

$$X^l v = 0, \tag{26}$$

and, second, cannot be represented in the form $X^{p+1-l}\chi$, where χ is any other vector,

$$v \neq X^{p+1-(\beta-s)}\chi. \tag{27}$$

Thus, we listed above all vectors for which the transfer matrix $t_{p/2}(u)$ has zero eigenvalues and, hence, the recurrence system of Eqs. (5) transforms, as was stated above, to a closed system of eigenvalue equations for the transfer matrix $t_{1/2}(u)$.

Eigenvalue calculations. Let us find the eigenvalues of the transfer matrix and Hamiltonian for the case $q^4 = -1$. One has

$$\begin{aligned} t_{3/2}(u) &= 0, \\ t_{1-j}(u) &= -(-1)^{\frac{N}{2}+\beta-s} t_j(u+\pi/2). \end{aligned} \tag{28}$$

To simplify calculations, we introduce the function $S_N(u) \equiv (-2)^{N/2} t_{1/2}(u - \eta/2)$. Then the functional relationships take the form

$$\begin{aligned} &S_N\left(u+\frac{\pi}{8}\right)S_N\left(u-\frac{\pi}{8}\right) \\ &= \cos^N(2u) - (-1)^{-\frac{N}{2}+l}\sin^N(2u). \end{aligned} \tag{29}$$

This equation contains the numbers N and $l = \beta - s$. Depending on whether these numbers are even or odd, one obtains four different equations and, correspondingly, four different solutions:

$$\begin{aligned} S^{\{n\}}_{4M}(u) &= \prod_{m=1}^{M}\left(1 + (-1)^{n_m}\cos\left(\pi\frac{2m-1}{4M}\right)\cos(4u)\right), \\ S^{\{n\}}_{4M+2}(u) &= \sin(2u)\sqrt{2}\prod_{m=1}^{M}\left(1 + (-1)^{n_m}\right. \\ &\quad \left.\times\cos\left(\pi\frac{2m}{4M+2}\right)\cos(4u)\right), \\ S^{\{n\}}_{4M-1}(u) &= e^{-iu}(-i)^{M-1/2} \\ &\quad \times\prod_{m=1}^{2M-1}\left(e^{(-1)^{n_m}\frac{i\pi m}{4M-1}}\sin\left(2u+\frac{\pi}{4}\right)\right. \\ &\quad \left.- ie^{-(-1)^{n_m}\frac{i\pi m}{4M-1}}\sin\left(2u-\frac{\pi}{4}\right)\right), \\ S^{\{n\}}_{4M+1}(u) &= e^{-iu}(-i)^{M} \\ &\quad \times\prod_{m=1}^{2M}\left(e^{(-1)^{n_m}\frac{i\pi m}{4M+1}}\sin\left(2u+\frac{\pi}{4}\right)\right. \\ &\quad \left.- ie^{-(-1)^{n_m}\frac{i\pi m}{4M+1}}\sin\left(2u-\frac{\pi}{4}\right)\right), \end{aligned} \tag{30}$$

where the symbol $\{n_m\}$ stands for any arbitrary set of numbers 0 or 1, e.g., {0, 1, 0, …, 0, 1}. We treat these numbers as Fermi occupation numbers. These functions satisfy the equation

$$\begin{aligned} &S_{4M+\delta}\left(u+\frac{\pi}{8}\right)S_{4M+\delta}\left(u-\frac{\pi}{8}\right) \\ &= \cos^{4M+\delta}(2u) + i^{-\delta}\sin^{4M+\delta}(2u). \end{aligned} \tag{31}$$

Thus, we have found solutions only in the case of odd $\beta - s$. For the energy eigenvalues, we obtain

$$\begin{aligned} \frac{E^{\{n\}}_{4M}}{4J} &= -\frac{4M}{2\sqrt{2}} - \frac{4}{\sqrt{2}}\sum_{m=1}^{M}(-1)^{n_m}\cos\left(\pi\frac{2m-1}{4M}\right), \\ \frac{E^{\{n\}}_{4M+2}}{4J} &= -\frac{4M+1}{2\sqrt{2}} \\ &\quad + \frac{2}{\sqrt{2}}\left(1 - 2\sum_{m=1}^{M}(-1)^{n_m}\cos\left(\pi\frac{m}{2M+1}\right)\right), \\ \frac{E^{\{n\}}_{4M-1}}{4J} &= -\frac{4M-1}{2\sqrt{2}} \\ &\quad - \frac{1}{\sqrt{2}}\left(i + 2i\sum_{m=1}^{2M-1}\exp\left(\frac{-2i(-1)^{n_m}\pi m}{4M-1}\right)\right), \\ \frac{E^{\{n\}}_{4M+1}}{4J} &= -\frac{4M+1}{2\sqrt{2}} \\ &\quad - \frac{1}{\sqrt{2}}\left(i + 2i\sum_{m=1}^{2M}\exp\left(\frac{-2i(-1)^{n_m}\pi m}{4M+1}\right)\right). \end{aligned} \tag{32}$$

Although the imaginary unit explicitly enters into the last two formulas, the energy E is real because the

imaginary parts cancel out when evaluating this sum. For the even spin-chain lengths $N = 4M$ and $N = 4M + 2$, we have found 2^M energy levels for each. For the odd spin-chain lengths $N = 4M - 1$ and $N = 4M + 1$, we have found, respectively, 2^{2M-1} and 2^{2M} eigenvalues.

We thank M.Yu. Lashkevich for helpful remarks and fruitful discussions.

REFERENCES

1. M. Gaudin, *La fonction d'onde de Bethe* (Masson, Paris, 1983; Novokuzn. Fiz.-Mat. Inst., Novokuznetsk, 2000).
2. V. Pasquier and H. Saleur, Nucl. Phys. B **330**, 523 (1990).
3. Yu-Kui Zhou, hep-th/9502053 (1995).
4. A. N. Kirillov and N. Yu. Reshetikhin, J. Phys. A **20**, 1565 (1987).
5. C. M. Yung and M. T. Batchelor, Nucl. Phys. B **446**, 461 (1995).
6. A. Belavin and Yu. Stroganov, hep-th/9908050 (1999); Phys. Lett. B **446**, 281 (1999).
7. V. Bazhanov, S. Lukyanov, and A. Zamolodchikov, Commun. Math. Phys. **177**, 381 (1996); **190**, 247 (1997); **200**, 297 (1999).
8. A. A. Belavin, S. Yu. Gubanov, and B. L. Feigin, hep-th/0008011.

Translated by V. Sakun

JETP Letters, Vol. 73, No. 9, 2001, p. 503.

Erratum: “Strong Correlations in a Model of a Gauged (2 + 1)-Dimensional Nonlinear Schrödinger Equation” [*JETP Letters*, 73, 5, 255–261]

A. P. Protogenov

PACS numbers: 71.10.Pm; 11.10.Lm

In A.P. Protogenov’s paper published in *JETP Letters*, vol. 73, no. 5, pp. 255–261, the formula $\rho = \frac{r_0}{-\frac{r_0\xi}{\sqrt{1+\gamma^2}}}$ in Eq. (35) should be read as $\rho = \frac{r_0}{\cosh\frac{r_0\xi}{\sqrt{1+\gamma^2}}}$, and Eq. (37) should be read as

$$\Psi(x,t) = \frac{a}{\sqrt{\lambda v}\cosh[a(x-vt)]}e^{iv(x-ut)}. \quad (37)$$

0021-3640/01/7309-0503$21.00